AD-A217 266

SYMPOSIUM
on
FLOW-INDUCED VIBRATIONS

VOLUME 5
TURBULENCE-INDUCED NOISE
AND VIBRATION OF
RIGID AND COMPLIANT SURFACES

Edited by

M.P. PAIDOUSSIS (Principal Editor)
McGill University
Montreal, Quebec, Canada

A.J. KALINOWSKI
Naval Underwater Systems Center
New London, Connecticut

DTIC
COPY
INSPECTED
1

Accesion For		
NTIS CRA&I	☑	
DTIC TAB	☐	
Unannounced	☐	
Justification		

By $24.^{00}$

Distribution /

Availability Codes

Dist	Avail and/or Special

A-1 2

THE AMERICAN SOCIETY OF MECHANICAL ENGINEERS
United Engineering Center   345 East 47th Street   New York, N.Y. 10017

90 01 18 031

PREFACE

The 1984 ASME Symposium on Flow-Induced Vibration is a unique event in the annals of technical meetings organized by ASME. Apart from promising to be one of the most important symposia anywhere on this topic in recent memory (only time will tell exactly how important), it is the first time that such a large symposium on the subject has been organized by ASME. Furthermore, it is the first time that no less than six Divisions of the ASME have cooperated in co-sponsoring a symposium on any given subject, which surely bespeaks of the importance of the subject matter of this particular Symposium. The participating Divisions are:

Applied Mechanics, Fluids Engineering, Heat Transfer, Noise Control and Acoustics, Nuclear Engineering, and Pressure Vessels and Piping.

I should like to thank them all, for without their support this Symposium would not have been the success that it is promising to be.

The Proceedings of the Symposium are published in six bound volumes, containing sixty-eight papers in all, as follows:

Volume 1 Excitation and Vibration of Bluff Bodies in Cross Flow
Volume 2 Vibration of Arrays of Cylinders in Cross Flow
Volume 3 Vibration in Heat Exchangers
Volume 4 Vibration Induced by Axial and Annular Flows
Volume 5 Turbulence-Induced Noise and Vibration of Rigid and Compliant Surfaces
Volume 6 Computational Aspects of Flow-Induced Vibration

The organization of a Symposium of this size, with world-wide participation (from 12 countries), has been both a challenging and rewarding experience. It entailed a great deal of work by many people: the session developers, the reviewers, ASME Headquarters' staff, the 1984 WAM Organizers and, of course, the authors. Of the many people involved, too numerous to mention by name here, I am specially indebted to the session developers and co-editors (O. M. Griffin, M. Sevik, M. K. Au-Yang, S. -S. Chen, J. M. Chenoweth, M. D. Bernstein and A. J. Kalinowski), and would like to single out two: Dr. M. K. Au-Yang and Dr. S. -S. Chen, whom I would like to thank for their unswerving support from the very beginning, when the possibility of a "multidivisional symposium" looked like a pie in the sky! I would also like to thank my secretary, Ruth Gray, for efficiently handling the enormous amount of paperwork involved in several passes of sixty-eight-plus papers across my desk.

Michael P. Paidoussis
Principal Symposium Coordinator
and Principal Editor

FOREWORD

The study of the growth of a boundary layer on flat and curved rigid surfaces has been the traditional realm of classical viscous aerodynamics and hydrodynamics, which began with the "discovery" of the existence of the boundary layer by L. Prandtl at the beginning of the century, and has grown exponentially ever since. Then followed the study of the pressure field generated in the boundary layer, with special interest to the vibration of the surfaces (in the case of flexible or flexibly mounted surfaces), as well as in the sound radiated from these surfaces.

However, in recent years, it has become well established that the development of a boundary layer on a truly compliant surface is not necessarily similar to that on a rigid or sensibly rigid surface. The pioneering experiments of Kramer and the theoretical work of T. Brooke Benjamin and M. T. Landahl in the early 1960's should be mentioned here, also, the more recent analytical work of F. E. Ffowcs-Williams and A. P. Dowling for applying the Lighthill sound analogy towards turbulent-boundary-layer noise predictions. Indeed, it has been found that transition to turbulence may be significantly retarded by surface compliance, to which, among other things, has been attributed the efficient swimming of dolphins, as well as opening the possibility of more efficient propulsion of submarines and surface craft. Of course, the resulting wall-pressure field is also different, as is the radiated sound field. Thus was created the relatively new field of research on turbulence-induced noise and vibration of compliant surfaces.

The seven papers in this volume, Vol. 5 of the Symposium Proceedings, make a significant contribution in the field, with both theoretical and experimental studies on the flow-induced excitation and vibration of compliant surfaces. The first two papers are concerned with the measurement of motions of the compliant surface induced by pressure fluctuations in the turbulent boundary layer (TBL), while the following two papers switch the emphasis to the fluid side of the TBL-structure interaction and focus on measurements of the wall-pressure spectrum, with special attention to the low-wave number noise components. In the last group of papers, theoretical aspects of turbulence are treated, where the TBL pressure at the fluid/compliant-surface interface is first computed by a simulation scheme and, in the last papers, by employing Dowling's extention of the Lighthill sound analogy.

We would like to thank the authors for their cooperation in submitting papers of high quality to this Symposium, and specifically on the topic of this volume of the Proceedings, as well as for their willingness to participate and share their experience with others in this Symposium. We would also like to thank the reviewers for their thoughtful comments and for the experience they have brought to bear in the review process, which has ensured the selection of only worthy papers for the Symposium and contributed to the improvement of those finally accepted.

M. P. Paidoussis

A. J. Kalinowski

v

CONTENTS

A NONCONTACTING ELECTROOPTIC DISPLACEMENT SENSOR FOR PIEZOELECTRICALLY DRIVEN ACTIVE SURFACES*

S. A. Cerwin
Southwest Research Institute
San Antonio, Texas

ABSTRACT

A noncontacting electrooptic displacement sensor for the measurement of the motion of a piezoelectrically excited active wall is described. The active wall was constructed and studied as part of a program conducted for the Office of Naval Research to investigate the drag reduction properties of an actively driven surface in turbulent water flow. The sensor employed a two arm optical triangulation method with a two element position sensitive detector to monitor the surface displacements from a stand-off distance of 23 cm (9 inches). Designed to operate in either an air or water medium, the displacement sensor demonstrated better than 1.3 μm (50 μ-inch) resolution over displacement ranges of approximately 1.3 mm (.05-inch). The system was implemented in two different configurations: one using an infrared LED light source and the other a visible red helium-neon laser source. In both cases, the light source was modulated, and a phase locked detector was used to reject unwanted ambient light. Spot size was an adjustable parameter and was set to 1 mm (.04-inch) for this application. The displacement monitor was articulated in three axes on precision translation stages to cover a 5 cm x 13 cm (2-in. x 5-in.) area. The system was successfully used to monitor accurately displacements on the order of 25 μm (.001-inch) peak-to-peak on an active wall driven by piezoelectric transducers over an acoustic frequency range from DC to 150 Hz.

INTRODUCTION

This paper describes a noncontacting electrooptical displacement sensor developed to monitor the motions of a piezoelectrically excited active wall with peak-to-peak displacements on the order of 25 μm. The active wall was devised in a program conducted for the Office of Naval Research[†] to investigate the drag reduction properties of an actively driven surface in turbulent water flow. The active portion of the wall was constructed by stretching a thin, diffusely re-flecting mylar membrane over an array of piezoelectric pushers spaced at an interval of 1.25 mm. A cross sectional view of the wall construction is given in Figure 1. Because each of the peizoelectric elements could be driven independently, proper adjustment of the phase and amplitude of individual drive wave-

forms provided stationary or traveling surface waves programmable in direction, amplitude, frequency, and in the case of traveling waves, wave speed. Details of the entire active wall program are being presented elsewhere [1] and the remainder of this paper describes the electrooptical displacement sensor and subsequent measurements performed on the active wall.
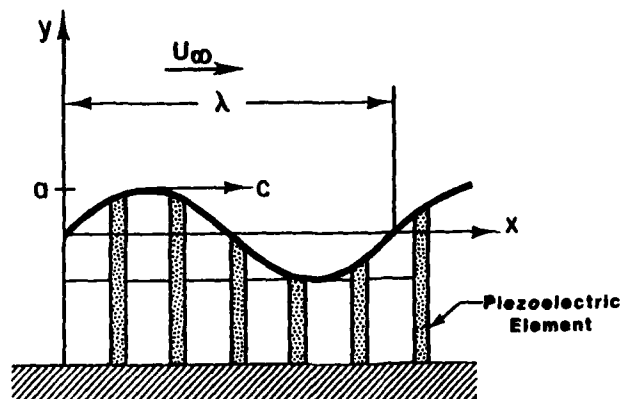

Figure 1. Illustration of Piezoelectrically Driven Active Wall.

PRINCIPLES OF OPERATION

The methodology used for the measurement technique is an adaptation of a technique developed by the author to profile roadway surfaces from a moving vehicle [2] and is illustrated in Figure 2. Two variations of the method can be implemented by choice of light source: a 1 mw Helium-Neon laser operating in the visible red at 633 nm or a high power (100 mw) light emitting diode (LED) operating in the near infrared at 933 nm. In both cases the light source is 100% amplitude modulated at a frequency of 5 kHz for use with phase sensitive detection so that a high signal-to-noise ratio and rejection of ambient light can be achieved. For the infrared version, the LED is modulated directly by the drive current, and for the visible red version, an acousto-optic modulator is used to modulate the laser. The light source is projected onto the target surface by a lens assembly oriented normal to the target surface to form a spot 1mm in diameter, a spot size small enough to resolve individual piezoelectric elements.

A portion of the light scattered from the diffusely reflecting target surface is collected by a receiving lens assembly oriented at 45° to the target surface. The lens assembly images the illuminated spot onto the center of a two element PIN photodiode detector with unity magnification. This target surface position, denoted as POSITION 1 in Figure 2, is the reference (or zero), position about which displacements are measured. At this position, the spot image is exactly centered on the two detector halves thereby causing the outputs of the two halves to be equal. By virtue of the 45° geometry, a positive or negative displacement of the target surface from the reference position causes a corresponding lateral shift of the spot image on the face of the dual detector. An example of a negative displacement is shown as POSITION 2 and is represented by the dashed lines for the target surface, light path, and spot image on the dual detector. Shifting the image of the spot on the face of the detector causes more area of the spot to fall on one half of the detector than the other, thus producing unequal outputs. The displacement signal is extracted by computing the difference and sum of the outputs of the two detector halves, then dividing the difference by the sum. The difference between the two detector halves as the image of the spot is translated from one detector half to the other, (beginning with the spot completely one half), is simply the difference in areas of a circle divided by a chord. The function is "S" shaped, with extremely good linearity for small displacements about center.
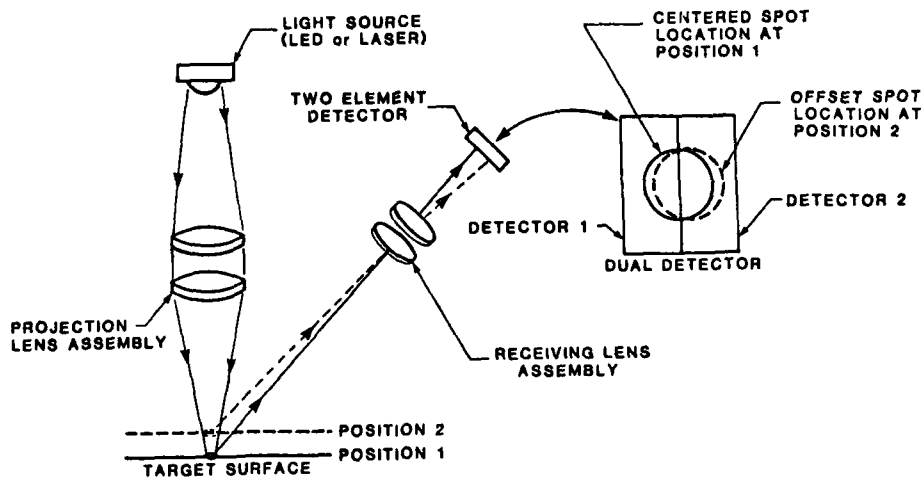
2

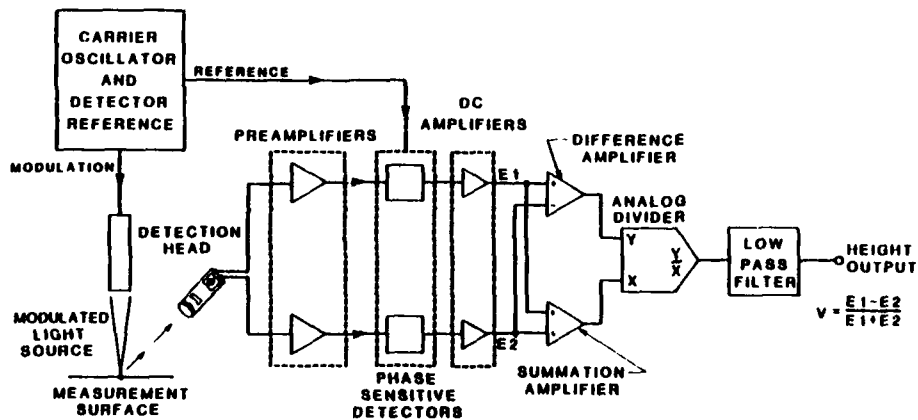Figure 2. Optical Displacement Measuring Technique

Figure 3. Electro-Optical Displacement Sensor

$$V = \frac{E1-E2}{E1+E2}$$

3

The sum of the two detector half outputs is a constant with respect to spot position and contains spot intensity and diameter information. The difference function is also influenced directly by spot intensity and diameter which is undesirable, as errors in the displacement measurement will occur if factors influencing spot intensity or detector sensitivity (e.g. LED or laser brightness, target surface reflectivity, water path attenuation, temperature, etc.) are variable. As the intensity and diameter data appear in both the difference and sum function, dividing the difference by the sum cancels errors associated with variable intensity or sensitivity. This method assumes uniform intensity within the spot, and no difficulties were encountered with nonuniform illumination or reflectance in this application. For details on a distance measurement system based on a similar principle but with provisions to cancel errors associated with nonuniformly reflective surfaces, the interested reader is referred to the system developed for profiling roadway surfaces [2].

A block diagram of the signal processing electronics for the displacement sensor is given in Figure 3. Design of the circuitry is straightforward and models the foregoing signal processing algorithm. A 5 kHz crystal controlled oscillator is used to drive the light modulator and to act as reference for the phase sensitive detectors. The outputs of the two detector halves are individually preamplified and filtered through active 5 kHz bandpass filters. DC restoration is accomplished through phase sensitive detectors and subsequent amplification by DC amplifiers. The DC voltages thus obtained (denoted by E1 and E2) are proportional to the light values impinging on each detector half. E1 and E2 are then processed by the differential and summation amplifiers and the resultant difference and sum are fed into the Y and X inputs of the analog divider. The quotient is $(E1-E1)/(E1+E2)$ and is taken as the displacement signal after high frequency noise component are removed by an active low-pass filter. The signal processing circuitry was packaged in a compact (12 cm x 18 cm x 25 cm) enclosure and was completely self-contained. The light source, lens systems, and detector assembly were mounted on a precision XYZ fixture for positioning over selected areas of the active wall.

Specification for some of the component parts implemented in the laboratory system are as follows:

LED Source:	Type TIES12 (Texas Instrument) 0.91 mm (0.036-inch) diameter 50 mw @ 933 nm
LED Projection lens Assembly:	72 mm focal length 50 mm diameter
Detector:	Type PIN Spot-2D (United Detector Technology) two element discreet active surface: 2.54 x 2.67 mm (0.1 x 0.105-in.)
Detector Lens Assembly:	47 mm focal length 45 mm diameter
Laser source:	Helium-Neon Type Spectra-Physics model 138, 1.0 mw @ 633 nm
Laser Modulator:	Acoustooptic Type Anderson Labs Model PLM-5VS 40 mHz center acoustic frequency 100% square wave modulation @ 5 kHz

SENSOR CALIBRATION AND FREQUENCY RESPONSE

The electrooptic displacement sensor was calibrated with a fixture constructed specifically for the task. The calibration fixture was fabricated by using a precision micrometer and ball configuration in conjunction with a 10:1 mechanical reduction arm to provide precise control over the reference surface. Thus 0.010-inch (254 μm) of travel on the micrometer head (which was readable to 0.0001-inch or 2.54 μm) produced 0.001-inch (25.4 μm) of travel at the reference surface. Precision ball bearings were used for the fulcrum.

4

Figure 4 is a typical response plot of the displacement sensor taken with the calibration fixture. The fixture was immersed in a transparent water tank for this test, with the reference surface set 15 cm from the entry point of the light beam. The infrared LED was used for the light source and the spot projection was directed into the tank normal to the top wall surface. The received light was collected through the adjacent tank side wall by the receiving lens which was oriented at 45° to the tank side wall. This resulted in a water path angle of 32° by virtue of refraction at the water/air interface. Linearity and resolution over the 25 μm peak-to-peak range is extremely good, as evidenced in Figure 4. Responsivity of the displacemenmt sensor in this configuration was measured to be 61.58 μm/volt.
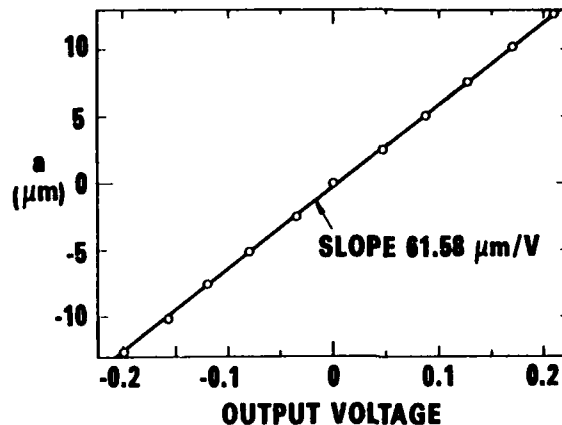

Figure 4. Displacement Calibration For Electro-Optical Sensor

Calibration data were taken in a total of four different configurations: in both air and water, and with both LED and laser light sources. The laser source has three distinct advantages and two distinct disadvantages for this application. First, the laser provides a much more intense source of light and operates at a wavelength which has little loss in water. The LED source, at 933 nm, is attenuated by the absorption band in water near 944 nm, presenting a signal strength problem for long water path distances. Second, the laser can be focused to a much smaller spot on the target surface, providing superior spatial resolution. The LED source cannot be focused efficiently to a spot much smaller than the physical diameter of the active area without incurring significant losses in intensity. Finally, the He-Ne laser operates in the visible red (as opposed to IR for the LED), making alignment of the system an easier task.

The disadvantages of using a laser are expense and stability. Most commercially available lasers in this power range, although relatively inexpensive in themselves, cannot be directly modulated. An acousto-optical modulator was used to provide the required 5 kHz subcarrier, and the cost of the modulator was more than that of the laser itself. Secondly, the laser must have a stabilized output relatively free from the noise components associated with the intermodulation products of multiple optical frequencies. These products commonly occur in the frequency range of 1 to 100 kHz, which is in-band to the 5 kHz subcarrier frequency. The noise components appear as sidebands about the 5 kHz subcarrier frequency and thus cannot be filtered easily. The analog division process removes most of the amplitude modulated noise components, but improvements in signal to noise ratios can be gained through the use of stabilized lasers.

The frequency response of the displacement monitor was measured by inserting an analog multiplier between the detector preamplifier and the remainder of the signal processing electronics. Light input to the detectors was held constant while the frequency of an external oscillator connected to the control input of the multiplier was varied. The frequency response curve is given in Figure 5 and shows reasonably flat response out to about 60 Hz with a roll off of approximately 8 dB/octave after the breakpoint. Response of the displacement sensor is
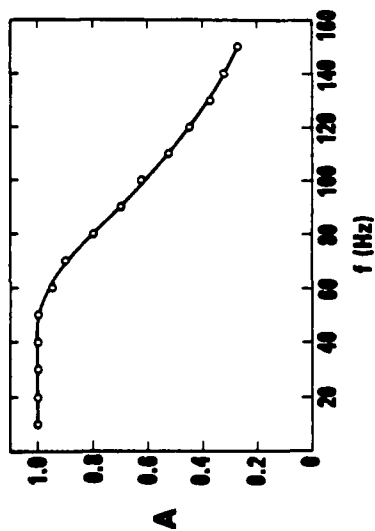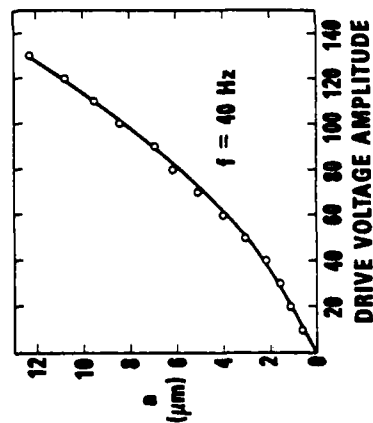
Figure 7. Wave Amplitude Response For Active Wall

Figure 8. Phase Response For Active Wall

Figure 5. Amplitude Response For Electro-Optical Sensor
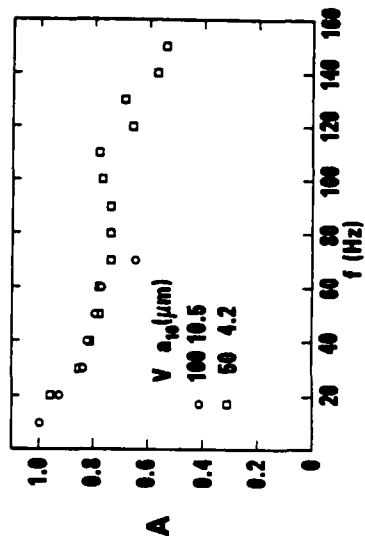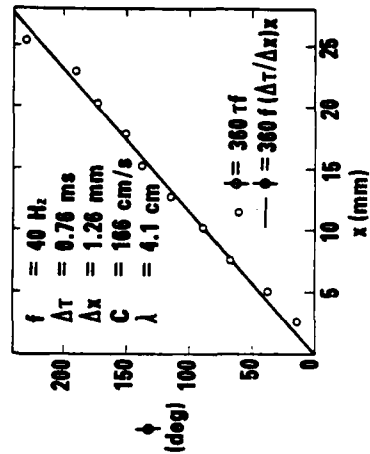
Figure 6. Wave Amplitude Calibration For Active Wall

6

an adjustable parameter and is controlled by the Q of the 5 kHz bandpass amplifier, design of the output low pass filter, and (somewhat) on the selection of carrier frequency.

ACTIVE WALL MEASUREMENTS

Actual measurements made on the prototype active wall are given in Figures 6, 7 and 8. In Figure 6, the amplitude response of an individual element of the active wall is plotted as a function of applied driving voltage at a fixed frequency of 40 Hz. Figure 7 shows the frequency response of the same element plotted as a function of drive frequency for an applied voltage of 150V peak-to-peak. For both Figure 6 and 7 the raw data obtained from the displacement monitor was corrected by the amplitude and frequency response calibrations of Figures 4 and 5. Figure 8 shows the longitudinal phase response of the active wall when set up to produce a traveling wave. The data were taken by translating the displacement monitor along the length of the active wall (transversing from element to element) at a fixed standoff distance. The wall demonstrated excellent phase linearity over a distance of approximately 30 mm (1.2 in.).

CONCLUSIONS

In summary, a methodology for producing noncontacting displacement measurements through air and water path distances to surfaces possessing very small absolute displacements has been described. Actual measurements have been performed on a piezoelectrically driven active wall with successful results.

ACKNOWLEDGMENTS

REFERENCES
1. Park, J. T., Silvus, H. S., Jr., and Cerwin, S. A., "An Active Wall Device for the Generation of Small Traveling Surface Waves," Review of Scientific Instrumentation (submitted for publication).

2. King, J. D., and Cerwin, S. A., "System for Inventorying Road Surface Topography (SIRST)," U. S. Department of Transportation, Federal Highway Administration, Final Report Contract No. DOT-FH-118498, FHWA/RD-82/062, Aug. 1982.

AN OPTICAL TECHNIQUE FOR MEASURING THE FLOW-INDUCED
MOTION OF A COMPLIANT SURFACE

M. Gad-el-Hak
Flow Research Company
Kent, Washington

ABSTRACT

The flow-induced motion of a compliant surface was measured using a novel remote optical technique. The "Laser Displacement Gauge" employs a Reticon camera equipped with a linear array of 256 photodiodes spaced 25 micron apart. A vertical beam of laser light produces a bright spot when it intersects the elastic or the viscoelastic compliant material, which contains minute amounts of Rhodamin-6G fluorescent dye. The axis of the photodiode array was aligned with the vertical laser beam. Thus, the digital output resulting from the continuous scanning of the array indicates the vertical displacement of the compliant surface. The system has a frequency response of 1 kHz, and resolves vertical displacements as low as 0.002 cm. The device was used to measure the characteristics of two classes of hydroelastic instability waves that form on elastic or viscoelastic compliant surfaces as a result of the interaction with a turbulent boundary layer.

1. INTRODUCTION

The motion of a fluid over a surface which complies to the flow offers the potential for a rich variety of fluid/surface interactions. Compliant surfaces are currently finding many engineering applications such as sound absorption in aero-engines, vibration reduction in Naval vessels, and noise shielding in sonar arrays. Moreover, intensive research is currently conducted to find compliant surfaces that will reduce the skin-friction drag on moving vehicles.

The design of a compliant coating to achieve a particular objective is a complex task requiring the determination of the surface response to a specific flow disturbance. This response is excited by the hydrodynamic forces and results in a surface motion which in turn acts on the flow field near the interface. Waves that form on the compliant surface can be either stable, unstable or neutral.

There exists a need for the development of reliable techniques to measure the compliant surface response under a variety of flow conditions. The device needed should be accurate, have a fast response, and not interfere with the observed phenomenon. Very few such devices exist today. Grosskreutz [1] used a Schlieren apparatus to measure the motion of a homogeneous but nonisotropic compliant surface made of rubber and subjected to a turbulent boundary layer in a water tunnel. He computed the frequency and the wavenumber dependence of the

9

flexibility of the compliant wall using the third-octave-spectra of the surface motion. Ash et al. [2] used a similar Schlieren method to provide flash photos of a compliant surface deformation in a wind tunnel. Dinkelacker et al. [3] placed a 97 mm pressure transducer containing several hundered membranes under a turbulent boundary layer. The device served as the mirror in a Michelson interferometer. High speed photographs of the fringe patterns in the interferometer were used to compute the dimensions and the speed of convected turbulent pressure fluctuations. More recently, Rathsam et al. [4] measured the "pre-instability", microscopic surface motion on a PVC plastisol in a turbulent boundary layer. Their laser/optics system sensed the instantaneous slope and the frequency of motion on the compliant surface where a focused laser beam was reflected. This device is incapable of directly measuring the amplitude of the surface motion, however, Rathsam et al. inferred the amplitude from the measured slope spectra by assuming a dispersion relation for the compliant surface response.

The remote optical technique presented in this paper is used to measure the flow-induced motion of a compliant surface. The technique is particularly suited for studying hydroelastic instability waves that form on an elastic or a viscoelastic compliant surface as a result of the interaction with a turbulent boundary layer. The waves' amplitude, wavelength and phase speed are directly measured with this linear device.

2. EXPERIMENTAL EQUIPMENT AND PROCEDURE
2.1 The Laser Displacement Gauge

The laser displacement gauge (LDG) is a remote optical device used in the present investigation to measure the compliant surface vertical displacement. The technique was originally developed for measuring wind-waves [5,6]. Its first use for measuring compliant surface deformation was reported by Gad-el-Hak et al. [7,8]. The system employs a Reticon camera (Model LC 600V) driven by a controller (Reticon Corporation, Model RS605). An optical interface is created at the surface of the compliant material, which contained minute amounts of Rhodamin-6G fluorescent dye, by projecting a 4 Watt vertical beam of argon-ion laser (Spectra Physics, Model 164-05) having a diameter of 1 mm. The displacement of this optical interface is measured by electronically scanning the photodiode array housed in the Reticon camera.

The axis of the photodiode array is aligned with the vertical laser beam above the fluid/compliant coating interface. The optical interface is imaged onto the photodiode array via a set of lenses and extension tubes. The linear photodiode array is composed of 256 elements spaced 25 μm apart. The aperture width of the array is also 25 μm. the spatial resolution, which is the same in both the vertical and longitudinal directions, depends on the field of view. For example, the spatial resolution is 0.01 cm for a field of view of 2.5 cm. In this case, the horizontal spatial resolution is only about one-tenth of the diameter of the laser beam. The scanning rate of the array ranges from 0.4 to 40 ms. The LDG is a digital device with practically no electronic drift. The digital output from the controller is a time series of integers from 1 to 256 updated at a frequency of the scanning rate. Each integer corresponds to the nth photodiode on which the optical interface is imaged during each scan. The digital output is recorded and analyzed on-line with a NOVA minicomputer system.

Calibration of the LDG is made by displacing the Reticon camera, which is fixed on an accurate traverse mechanism, to several vertical positions with predetermined increments. A second-degree polynomial is best-fitted through the calibration points to account for nonlinearity resulting from the aberration of the optical lenses. The ratio of the coefficients of the nonlinear and linear terms was typically 10^{-4}. For practical purposes, the displacements may be considered to be linearly porportional to the LDG output.

The Reticon camera is mounted so that it looks down onto the compliant surface at a nearly horizontal angle. This arrangement minimizes blockage of the

optical interface by the wave crests between the laser beam and the tank wall on the side where the camera is mounted. This blockage occurs most often near the troughs of the waves, where the wave profiles are relatively smooth. Whenever a blockage occurs, the photodiode array loses its object (i.e. the optical interface) and the maximum diode number of 256 is registered by the controller. Therefore either a sharp jump or a sharp spike, depending on the duration of the blockage, appears on the measured wave profiles. To remove the sharp jumps or spikes the computer was programmed to replace them with a straight line that connects the points before and after each jump or spike.

In the present experiments the laser displacement gauge was set to have a frequency response of 1 kHz and to resolve vertical displacments as low as 0.002 cm.[1] The surface deformations were also recorded using a 16 mm movie camera moving with the plate (Section 2.2). For the elastic surface, the camera was mounted to the side to capture a side view of the instability waves; while for the viscoelastic surface a top view was more suited to observe the instabilities developing on such a surface.

2.2 Flow Facility

The Flow Research 18-m towing tank was used in the present experiments. The 1.2 m wide, 0.9 m deep water channel has been described by Gad-el-Hak et al. [9]. To generate a turbulent boundary layer, a flat plate was rigidly mounted under a carriage that rides on two tracks mounted on top of the towing tank. During towing, the carriage was supported by an oil film which insured a vibrationless tow, having an equivalent freestream turbulence of about 0.1 percent. The carriage was towed by two cables driven through a reduction gear by a 1.5 hp Boston Ratiotrol motor. The towing speed was regulated within an accuracy of 0.1 percent. The system was able to achieve towing speeds between 20 and 140 cm/sec for the present study. The flat plate used in the present experiment has an aluminum frame that provided a flat bed for the Plexiglas working surface. The gaps in the aluminum frame were filled with lightweight styrofoam and the frame was painted with marine enamel to prevent corrosion. The whole structure was buoyant in water and was flat to within 0.2 mm. Care was taken to avoid leading-edge separation and premature transition by having an elliptic leading edge and an adjustable lifting flap at the trailing edge. The flap was adjusted so that the stagnation line near the leading edge was located on the working surface. The working surface was smooth and was 210 cm long and 106 cm wide. A 45 cm by 95 cm well was built into the working surface for placing compliant materials of up to 1 cm in thickness.

Trips were used to generate a fully-developed turbulent boundary layer. The trips were brass cylinders with 0.32 cm diameter and 0.25 cm height placed 20 cm behind the leading edge, and having their axes perpendicular to the flat plate. During towing, the plate and the movie cameras moved at a speed $U\infty$, while the Reticon camera and the vertical laser beam were fixed in space.

2.3 Compliant Material

A nearly-ideal elastic compliant surface and an incompressible viscoelastic one were used in the present investigation. The elastic coating was made of commercially available Knox gelatins. The gelatin powder was dispersed in boiling water, followed by the addition of an equal amount of room-temperature water. The concentration of the gelatin was varied in the range of 1 to 6 parts of weight of gelatin per 100 parts of water. The mixture was poured into the well in the flat plate and allowed to gel for 16 hours before using for a maximum of 8 hours, then a new coating was formed for the next series of runs. Care was taken to insure that the compliant surface was smooth and flush with the rest of the Plexigas working surface.

---

[1] The field of view is then about 0.5 cm.

Whenever a new coating was poured, a 0.6 cm x 10 cm x 10 cm sample was produced from the same mixture to measure the modulus of rigidity, G. The shear modulus of rigidity was measured with an automated strain gauge/LVDT device which subjected the sample to a prescribed shear force and the displacement was measured. The force versus displacement curve was always linear in spite of the fact that displacement as high as 50% of the thickness were used. The modulus value was quite sensitive to small differences in the mixing process and ranged in value from 400 dyne/cm^2 at the lowest concentration used to 25,000 dyne/cm^2 at the highest concentration.

The viscoelastic coating used in the present investigation was a plastisol gel made by heating to 160°C a mixture of polyvinyl chloride resin (PVC), dioctyl phthalate (plasticizer), and dibutyl tin maleate (stabilizier). The mixture was poured in a heated aluminum pan and allowed to cool gradually to complete the gelation process. The pan was then placed inside the well in the working surface of the flat plate and its height was adjusted from the bottom to insure a flush smooth surface. Unlike the gelatin, the PVC plastisol solidified rather quickly, particularly when the percentage of PVC in the mix increased.

Several recent studies have used similar PVC plastisols to study their interactions with laminar and turbulent flows [10-16]. In the present experiments, the modulus of rigidity of the PVC plastisol was varied in the range of 50 to 125,000 dyne/cm^2 by changing the percentage of PVC from 3 to 25 percent in the mixture. The stabilizer was always 10 percent of the PVC by weight. To check the viscoelasticity of the plastisol, a dynamic test was conducted on a sample using the strain gauge/LVDT device. A shear stress was applied until the system came into equilibrium, and the stress was suddenly released. The value of the subsequent strain was observed using the LVDT and a Nicolet digital oscilloscope (Model 4094). The observed time history indicated that the plastisol could be modeled as a viscoelastic solid of the generalized Kelvin type [17]. The time constant of the plastisol decreased as the percentage of PVC in the mix increased. For the 3% plastisol, the relaxation time was about 1 second, indicating a relatively strong damping. Since mechanical properties of the material change considerably during gelling, the compliant surface and the sample were allowed to sit in air for 16 hours before testing and using in the tank. Typically a coating was used for 8 hours before a new one was formed for the next series of tests.

3. RESULTS

The slowest travelling free wave speed on the surface of either an elastic or a viscoelastic solid is given approximately by the transverse wave speed $c_t = \sqrt{G/\rho_s}$, where G is the shear modulus of rigidity[2] and ρ_s is the density of the solid. Whenever the free stream velocity, U_∞, becomes sufficiently large compared to c_t, unstable waves appear on the solid surface. The onset speed of the two classes of hydoelastic instability was determined from the Reticon camera records and from visual observation of the compliant surface. The results for different moduli of rigidity and different thicknesses are shown in Fig. 1. For a particular coating thickness, the onset of instabilities on the viscoelastic coating is generally observed at higher ratios of the onset speed to the transverse wave speed than for the elastic coating. For both coatings, U_{onset}/c_t decreases as the thickness, d, increases. In other words, thick surfaces are more susceptible to the hydroelastic instability than thin ones.

Typical examples of the instability waves on the elastic and the viscoelastic coatings, as recorded by the Reticon camera, are shown in Fig. 2. Both coatings have a thickness of d = 0.32 cm and the freestream speed was U_∞ = 80 cm/sec. The

---

[2]For an elastic solid, the shear modulus is real; whereas for a viscoelastic solid it is complex and frequency dependent, the real part is the shear storage modulus G and the imaginary part is the shear loss modulus G'.
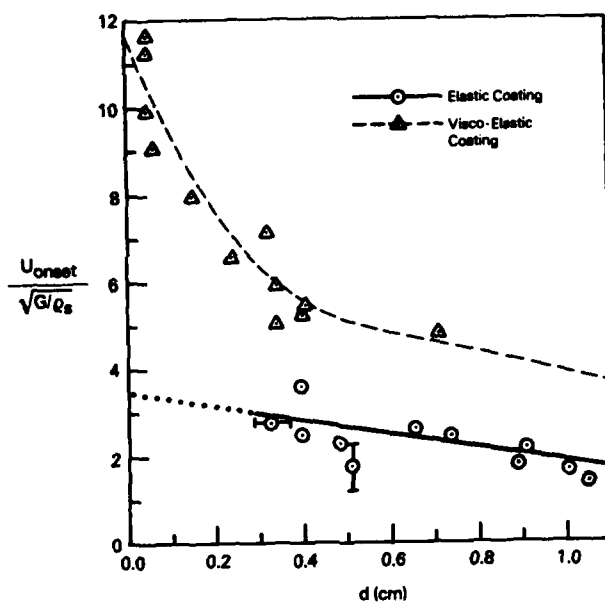
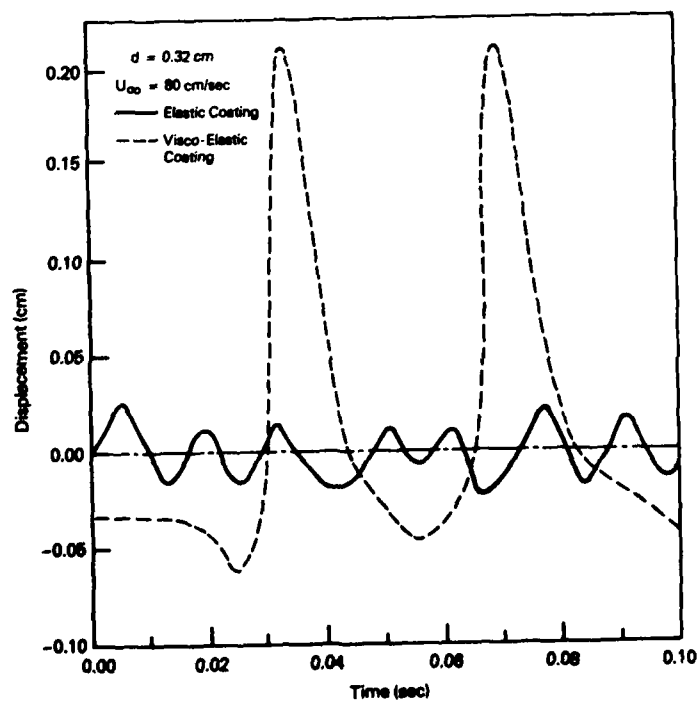**Figure 1.   Onset Speed Dependence on Thickness**

Figure 2.   Typical Surface Displacement

13

modulus of rigidity for the elastic coating was $G = 740$ dyne/cm^2 and for the visco-elastic coating was $G = 50$ dyne/cm^2. A well defined average wavelength and ampli-tude are apparent. The elastic waves have smaller wavelength and amplitude as compared to the waves excited on the viscoelastic surface. The peaks of the waves on the viscoelastic coating are sharp and the valleys are shallow and broad; while the elastic waves are more or less symmetric. The waveform on the viscoelastic surface appears to be non-sinusoidal with higher harmonics phase-locked with the fundamental wave.

In the viscoelastic coating case, small amplitude waves always grew very rapidly to large amplitude; consequently, a wave train of small amplitude could never be recorded. With the elastic coating at low flow velocities, small amplitude waves existed. The growth mechanism for the two kind of instabilities appears to be different.

The average wavelength was measured from the ciné films. By averaging over several frames, the statistical scatter of this random phenomenon was reduced to a standard deviation of less than 20%. For both the elastic surface and the viscoelastic surface the wavelength has a strong dependence upon the depth of the coating and upon the flow speed as shown in Figures 3(a) and 3(b), for five elastic coatings and five viscoelastic coatings, respectively. The elastic waves are generally shorter than the viscoelastic waves, indicative of the two different types of instability. The wavelength increases as the flow speed and the coating thickness increase for both coatings. However, a maximum wavelength is observed for each of the five viscoelastic coatings. The flow speed at which this maximum is observed coincided with the appearance of a three-dimensional wave structure superimposed on the normally two-dimensional viscoelastic waves. As the velocity continued to increase, small irregularities along the wave crests seemed to spawn new crescent shaped waves downstream. As these additional waves appeared over the viscoelastic surface, the average wavelength decreased as seen. No similar phenomenon was observed for the elastic coating at the speeds achieved in the present experiments.

The data of Figures 3(a) and 3(b) are normalized with the thickness, d, and the transverse wave speed, c_t, and are replotted in Figures 4(a) and 4(b). Scaling the wavelength with the thickness reduces the range of the elastic coating data but does not appear to collapse the data, suggesting that another length scale may be relevant to the problem. For the viscoelastic coatings, the data collapses reasonably well for the two-dimensional waves, while the three-dimensional wave data do not collapse.

The average peak-to-trough amplitude, 2A, was computed from the Reticon camera's output. The results are shown in Figures 5(a) and 5(b) for the elastic coating and the viscoelastic coating, respectively. The peak-to-trough amplitude for the waves on both surfaces increases monotonically with both the thickness and the flow speed. The elastic waves data do not collapse when the amplitude is normalized with the coating thickness, while the viscoelastic waves scale with the thickness indicating, perhaps, that the maximum amplitude is limited by the thickness. However, confidence in this result should be tempered by the limited amount of data in the figure.

As mentioned before, very few small amplitude waves were ever observed on the viscoelastic coating. No measurable surface deformation was observed as long as the velocity was below the onset speed, and immediately above the threshold velocity, waves with amplitude of typically $2A/d = 0.5$ appeared. With the elastic coating at velocities near onset, small amplitude waves existed. The growth rate for the two waves is evidently different.

One of the greatest differences between waves on the elastic and the visco-elastic coatings is the phase speed. The phase speed c_p was determined from the record of the Reticon and the movie cameras using the relation:

$$\lambda = P(U_\infty - c_p) \quad,$$

14
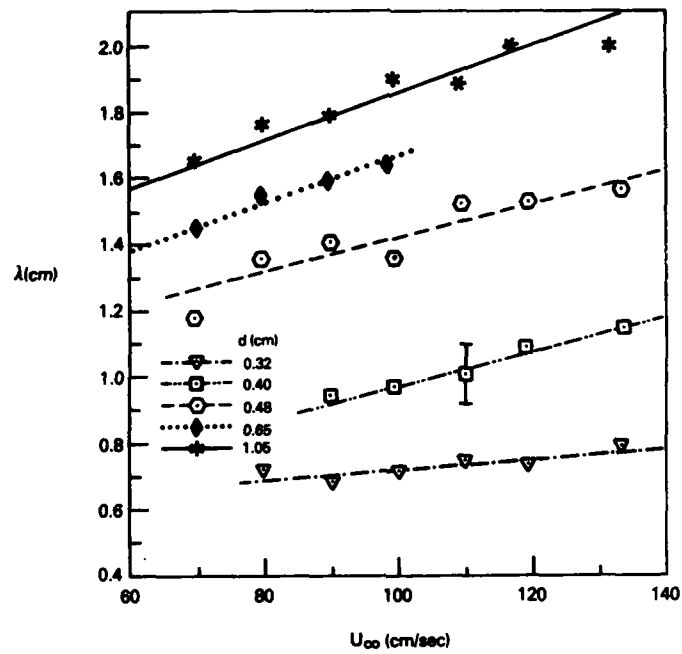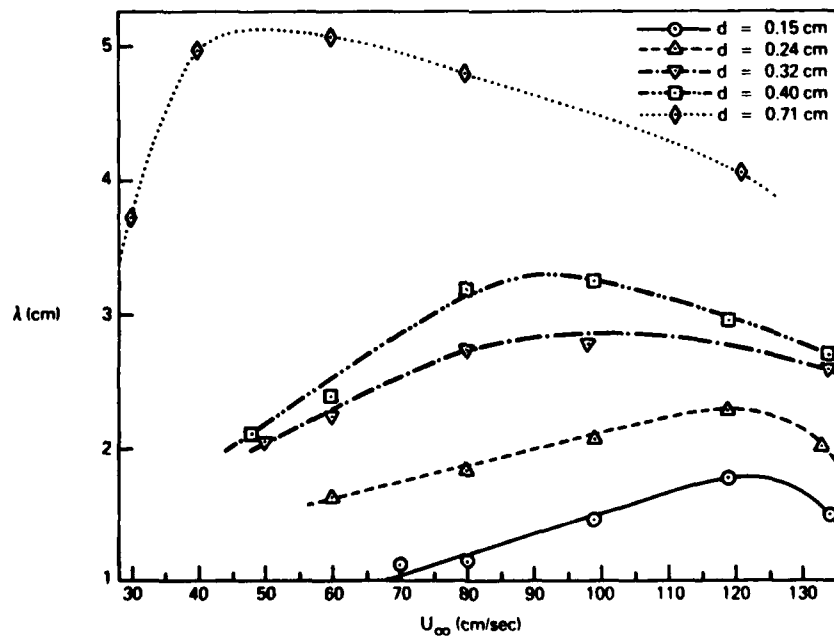
a. Elastic Coating

b. Viscoelastic Coatings

Figure 3. Wavelength Dependence on Thickness and Flow Speed

15
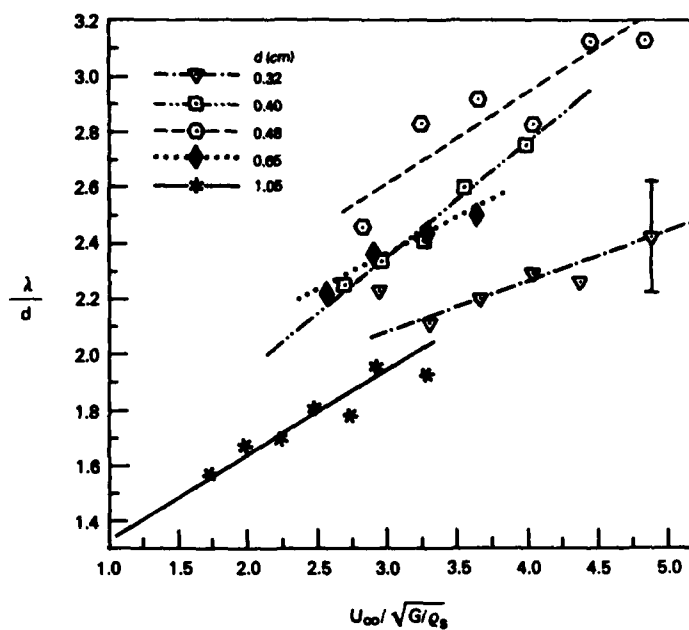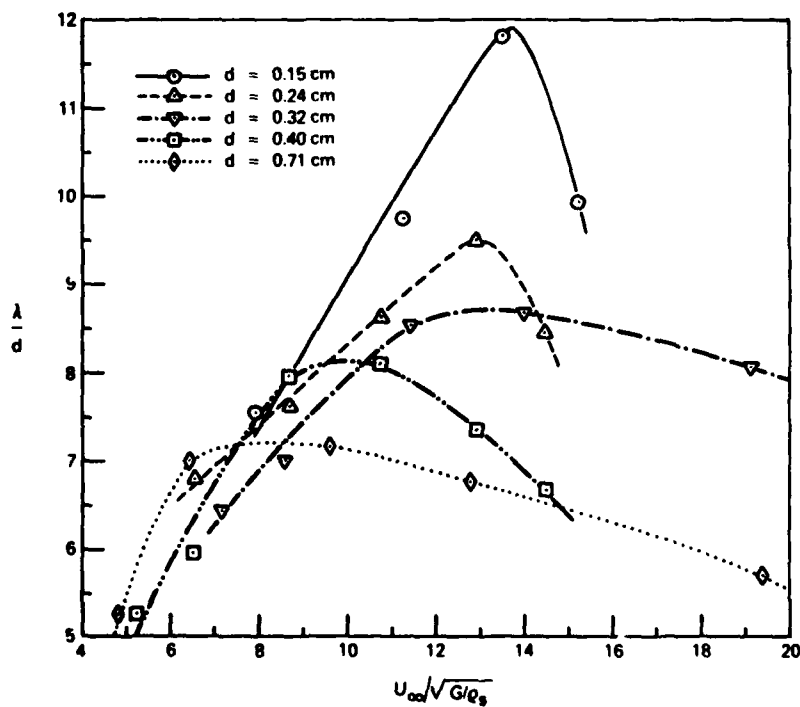
a. Elastic Coatings

b. Viscoelastic Coatings

Figure 4.   Wavelength Dependence on Thickness and Flow Speed (Normalized Plots)

16
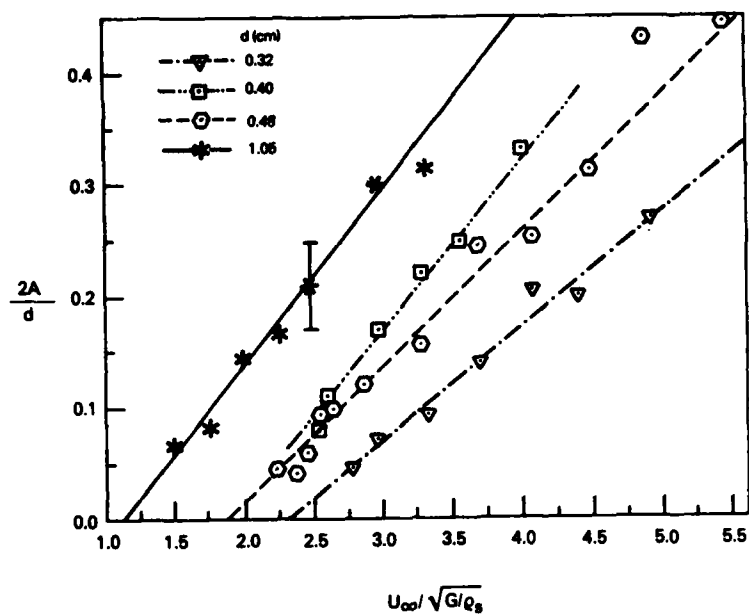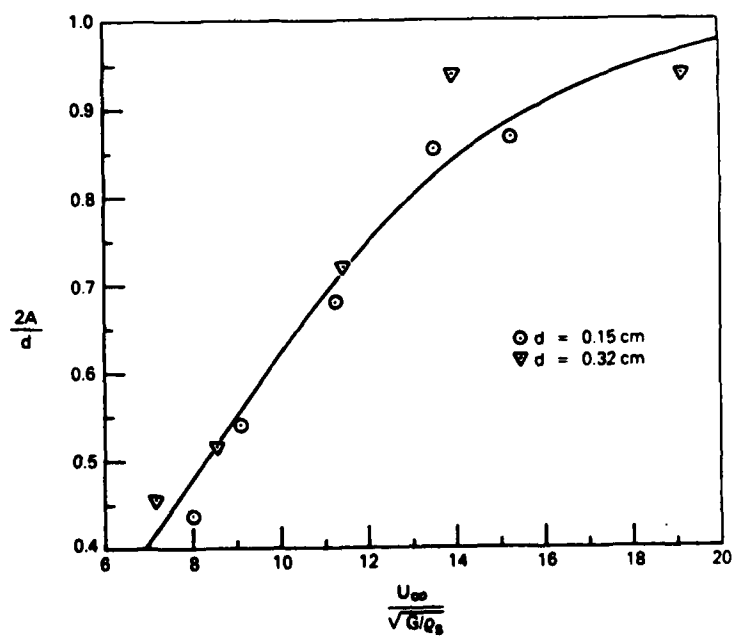
a. Elastic Coatings

b. Viscoelastic Coatings

Figure 5. Wave-Amplitude Dependence on Thickness and Flow Speed

17

where λ is the wavelength measured from the ciné films, P is the period measured from the Reticon camera's record, and U_∞ is the flow speed. As shown in Figures 6(a) and 6(b), the phase speed for the elastic waves are between 25 and 50 percent of U_∞. As noted by the error bars, there is some uncertainty in the data. Nevertheless, it appears that the phase speed for the elastic waves is a constant percentage of U_∞ independent of U_∞/c_t. On the other hand, the visco-elastic waves have an extremely low phase speed compared to other characteristic velocities in the fluid. The maximum value of c_p for these waves was 5 percent of U_∞. For the waves on the viscoelastic surface, the phase speed increases as the flow speed or the thickness increases. The dependence on flow speed appears to be given approximately by a power law:

$$c_p \sim U_\infty^{2.6}$$

4. DISCUSSION

A solid in vacuum can sustain free surface waves that may be modelled as a linear combination of waves having displacements perpendicular to or parallel to the propagation direction. These are called transverse and longitudinal displacement waves, respectively. For a linear-elastic solid, the propagation velocity of the transverse waves is $c_t = \sqrt{G/\rho_s}$, and that of the longitudinal waves is $c_\ell = \sqrt{(\lambda+2G)/\rho_s}$, where G and λ are elastic constants and ρ_s is the density of the solid. For a nearly-incompressible solid, $\lambda >> G$ and $c_\ell \to \infty$. The free surface wave dispersion relationship for a finite thickness solid has been reported by Gad-el-Hak et al [8].

To determine the effects of the fluid motion on the compliant surface, the analysis should be extended to include the surface stresses induced by the fluid moving over the compliant coating. Some general aspects of this case have been addressed by, among others, Benjamin [18,19], Landahl [20], and Kaplan [21]. Benjamin and Landahl have conducted stability analysis and have established that three types of instability waves may exist. The first type, labeled Class A, is an instability which is destabilized by the addition of dissipation or damping in the system. Duncan et al. [22] have suggested that pressure phase lags transfer energy from the flow to the interfacial wave system, thus stabilizing these waves. Static-divergence waves, commonly observed on viscoelastic surfaces excited with a turbulent boundary layer of sufficient strength, appear to be a member of this class. The second type, Class B, is stabilized by damping and destabilized by pressure effects, as for example in the case of wind waves. The third, Class C, corresponds to a Kelvin-Helmholtz type of instability, where the waves grow or decay primarily through reversible processes. Kaplan [21] has computed solutions for specific cases.

Assuming that the surface stress of primary importance due to the fluid is pressure, the effect of the fluid motion on the compliant surface can be simply modelled by considering the basic flow over the coating as inviscid and unsheared, and hence using potential flow theory to determine the surface pressure in terms of the surface displacement. Duncan et al. [22] have recently explored the dispersion relation for a one-layered, viscoelastic solid. The pressure applied at the surface was a generalization of the potential flow solution to include arbitrary amplitude reduction and phase shift. Their results are in qualitative agreement with the present experimental data. In the case of a viscoelastic coating with high damping, they find that the first instability occurring with increasing flow speed is a damping instability (Class A) which has phase speeds of a few percent of U_∞. When the damping is reduced sufficiently to approximate an elastic coating, the first instability found with increasing flow speed is a phase-lag instability (Class B) which has a much larger phase speed. Duncan and Hsu [23] extended the one-layer analysis to determine the response of a two-layer coating to pressure disturbances from a turbulent boundary layer.

Experimentally, conditions have been identified in which flow-induced deformations occur on a viscoelastic compliant surface. Boggs and Hahn [24] were the

18
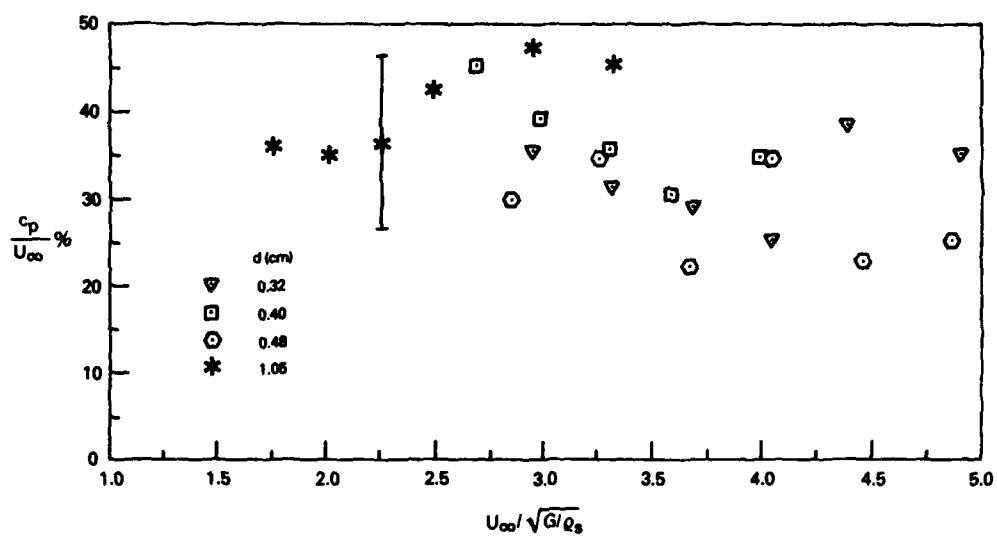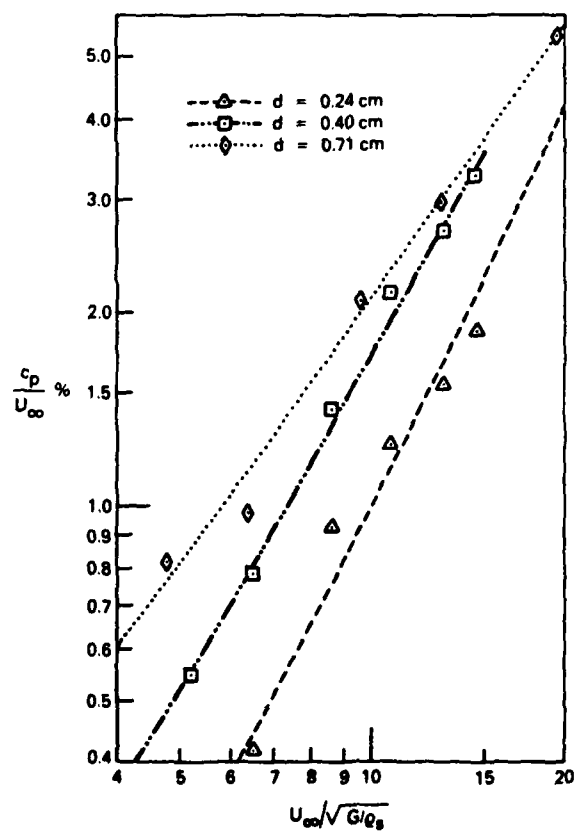
a. Elastic Coatings

b. Viscoelastic Coatings

Figure 6. Phase Speed for the Unstable Waves

19

first to point to the existence of a large amplitude, spanwise wave structure on a compliant surface/fluid interface due to the fluid motion. These "static-divergence" waves[3] appeared after the freestream exceeded an onset velocity threshold. The term static divergence is derived from the analogous static-instabilities that precede flutter on a flat plate exposed to a high speed flow [25,26]. In a series of experiments, Hansen & Hunston [10-13] and Hansen et al. [14,15] established several quantitative characteristics of the static-divergence waves, such as the conditions for their initiation, propagation speed and influence on hydrodynamic drag. Gad-el-Hak et al. [7,8] presented definitive data on the instabilities of a viscoelastic compliant coating.

No corresponding experimental data are available for Class B instabilities. It is anticipated from the theoretical work of Benjamin [19] and others that these instabilities may appear on compliant surfaces having little or no damping. Hence, the use of elastic coatings in the present investigation was intended to provide a data base for existing theories on the instability of elastic compliant coatings. The experimental results presented in Section 3 agree qualitatively with the theory by Duncan et al. [22]. The onset speed and the slow phase speed observed for the waves on the viscoelastic surface are the same as that predicted for Class A instability (static-divergence waves). On the other hand, the theory predicts a much higher phase speed for Class B instability occurring on surfaces with little or no damping. The phase speed of the elastic waves is an order of magnitude larger than that for the viscoelastic waves as seen in Fig. 6.

5. CONCLUSIONS

The flow-induced motion of a compliant surface was measured using a novel remote optical technique. Turbulent boundary layers were generated on a zero-pressure gradient flat plate. The 2-m long plate was towed in the range of speeds of 20 to 140 cm/sec in an 18-m water channel using a carriage riding on an oil film. A well that covers 20 percent of the working surface was used for placing the compliant material flush with the surrounding Plexiglas surface. The thickness of the coating was varied in the range of 0.2 to 1.0 cm.

Two different compliant materials were used in the present investigation. The first was an elastic gel made of gelatin and water. The second coating was a viscoelastic plastisol gel made by the heating-induced gelation of polyvinyl chloride resin, dioctyl phthalate and dibutyl tin maleate. The shear modulus of rigidity of both coatings was varied over a wide range (50 to 125,000 dyne/cm^2) by varying the percentage of gelatin or PVC in the mix.

The vertical displacement of the compliant surface was measured using the "Laser Displacement Gauge", which employs a Reticon camera equipped with an array of 256 photodiodes spaced 25 microns apart. A vertical beam of an argon-ion laser produced a bright spot when it intersected the compliant surface, which contained minute amounts of Rhodamin-6G fluorescent dye. The axis of the photodiode array was aligned with the vertical laser beam. Thus, the digital output resulting from the continuous scanning of the array indicated the vertical displacement of the compliant surface. The system had a frequency response of 1 kHz, and resolved vertical displacements as low as 0.002 cm.

Two different classes of hydroelastic instabilities were observed on the elastic surface and on the viscoelastic surface. The onset speed for these instabilities depends upon the coating's geometrical and mechanical properties. The elastic surface instability has a relatively high phase speed and a small wavelength, and its wave profile is symmetric as compared to the slow and highly nonlinear "static-divergence" waves observed on the viscoelastic surface. The experimentally determined wave characteristics compare qualitatively to existing theories on fluild/compliant surface interactions.

---

[3]Class A instability.

REFERENCES

1. Grosskreutz, R. (1971) "Wechselwirkungen Zwischen Turbulenten Grenzschichten und Weichen Wänden," Max-Planck-Institut für Strömungsforschung, Göttingen, No. 53.

2. Ash, R. L., Bushnell, D. M., Weinstein, L. M., and Balasubramanian, R. (1975) "Complaint wall Surface Motion and its Effects on the Structure of a Turbulent Boundary Layer," Proc. Fourth Biennial Symp. on Turbulence, eds. J. L. Zakin & G. K. Patterson, Univ. Missouri-Rolla, p. 220.

3. Dinklacker, A., Hessel, M., Meier, G. E. A., and Schewe, G. (1977) "Investigation of Pressure Fluctuations beneath a Turbulent Boundary Layer by Means of an Optical Method," Phys. Fluids 20, p. S216.

4. Rathsam, A. D., Mastny, G. F., Phillips, T. E., and Reischman, M. M. (1983) "Laser/Optics System for Measuring Microscopic Motion on Compliant Materials in Turbulent Boundary Layers," Proc. Eighth Biennial Symp. on Turbulence, eds. J. L. Zakin & G. K. Patterson, Univ. Missouri-Rolla, p. 30-1.

5. Liu, H.-T., Katsaros, K. B., and Weissman, M. A. (1982) "Dynamic Response of Thin-Wire Wave Gauges," J. Geophys. Res. 87, p. 5686.

6. Liu, H.-T., and Lin, J.-T. (1982) "On the Spectra of High-Frequency Wind Waves," J. Fluid Mech. 123, p. 165.

7. Gad-el-Hak, M., Blackwelder, R. F., and Riley, J. J. (1983) "Interaction of Compliant Surfaces with Transitional and Turbulent Boundary Layers," in Structure of Complex Turbulent Shear Flow, eds. R. Dumas & L. Fulachier, Springer, p. 20.

8. Gad-el-Hak, M., Blackwelder, R. F., and Riley, J. J. (1984) "On the Interaction of Compliant Coatings with Boundary Layer Flows," J. Fluid Mech. 140, p. 257.

9. Gad-el-Hak, M., Blackwelder, R. F., and Riley, J. J. (1981) "On the Growth of Turbulent Regions in Laminar Boundary Layers," J. Fluid Mech. 110, p. 73.

10. Hansen, R. J., and Hunston, D. L. (1974) "An Experimental Study of Turbulent Flows over Compliant Surfaces," J. Sound & Vibration 34, p. 297.

11. Hansen R. J., and Hunston, D. L. (1974) "An Experimental Study of the Hydro-dynamic Drag on Compliant Surfaces: Fluid Property Effects," Proc. 8th Int. Congress on Acoustics 2, p. 579.

12. Hansen, R. J., and Hunston, D. L. (1976) "Further Observations on Flow-Generated Surface Waves in Compliant Surfaces," J. Sound & Vibration 46, p. 593.

13. Hansen, R. J. and Hunston, D. L. (1983) "Fluid Property Effects on Flow-Generated Waves on a Compliant Surface," J. Fluid Mech. 133, p. 161.

14. Hansen, R. J., Hunston, D. L., Ni, C. C., and Reischman, M. M. (1980) "An Experimental Study of Flow-Generated Waves on a Flexible Surface," J. Sound & Vibration 68, p. 317.

15. Hansen, R. J., Hunston, D. L., Ni, C. C., Reischman, M. M., and Hoyt, J. W. (1980) "Hydrodynamic Drag and Surface Deformations Generated by Liquid Flows over Flexible Surfaces," in Viscous Flow Drag Reduction, ed. G. R. Hough, p. 439.

16. Hoyt, J. W. (1981) "A Flow-Visualization Study of Turbulent Spots on Solid and Compliant Surfaces," Proc. Seventh Biennial Symp. on Turbulence, eds. J. L. Zakin & G. K. Patterson, Univ. Missouri-Rolla, p. 32-1.

17. Jaeger, J. C., and Cook, N.G.W. (1976) Fundamental of Rock Mechanics, second edition, Chapman & Hall, p. 314.

18. Benjamin, T. B. (1960) "Effects of a Flexible Boundary on Hydrodynamic Stability," J. Fluid Mech. 9, p. 513.

19. Benjamin, T. B. (1963) "The Threefold Classification of Unstable Disturbances in Flexible Surfaces Bounding Inviscid Flows," J. Fluid Mech. 16, p. 436.

20. Landahl, M. T. (1962) "On the Stability of a Laminar Incompressible Boundary Layer over a Flexible Surface," J. Fluid Mech. 13, p. 609.

21. Kaplan, R. E. (1964) "The Stability of Laminar Incompressible Boundary Layers in the Presence of Compliant Boundaries," Sc. D. Thesis, MIT.

22. Duncan, J. H., Waxman, A. M., and Tulin, M. P. (1982) "Dispersion Relationships for Waves at the Interface between a Single Layer Visco-Elastic Compliant Coating and a Turbulent Flow," Hydronautics Tech. Report No. 8111-1.

23. Duncan, J. H., and Hsu, C. C. (1984) "The Response of a Two-Layer Viscoelastic Coating to Pressure Disturbances from a Turbulent Boundary Layer," AIAA 22nd Aerospace Sciences Meeting, Reno, AIAA-84-0535.

24. Boggs, F. W., and Hahn, E. R. (1962) "Performance of Compliant Skins in Contact with High Velocity Flow in Water," Proc. 7th Joint Army-Navy-Air Force Conference on Elastomer Research and Development 2, San Francisco, p. 443.

25. Weaver, D. S., and Unny, T. E. (1970) "The Hydroelastic Stability of a Flat Plate," J. Applied Mech. 37, p. 823.

26. Weaver, D. S., and Unny, T. E. (1973) "On the Dynamic Stability of Fluid-Conveying Pipes," J. Applied Mech. 40, p. 48.

PRACTICAL REQUIREMENTS OF TURBULENT BOUNDARY LAYER FORCING FUNCTION MEASUREMENTS WITH WAVE-VECTOR FILTERS

F. E. Geib, Jr.
David W. Taylor Naval Ship Research and Development Center
Bethesda, Maryland

ABSTRACT

A discussion is presented on the use of wave-vector filters to measure the pressure fluctuations that are produced on the surface of a body by the turbulent boundary layer. Wave-vector filters allow the forcing function to be examined in spectral space as a function of wave number and frequency. The discussion presents a summary of the techniques used in wave-vector filtering, how these techniques are implemented with linear arrays of flush-mounted pressure transducers, and the effects of changing various parameters. Practical problems of making measurements with a linear wave-vector filter array are pointed out, including the adequacy of facilities.

NOMENCLATURE

c	= speed of sound
d	= center-to-center spacing of transducers
f	= frequency
$\vec{k}$	= vector wave number
k_i	= components of vector wave number
k_i'	= specific value of a wave number component
k_c	= sonic wave number
p	= turbulent boundary layer pressure
D	= diameter of sensitive area of circular transducer
L	= a typical transducer dimension
N	= number of transducers in a linear wave-vector filter array
R	= radius of sensitive area of circular transducer
U	= an arbitrary speed
U_c	= convection speed of turbulent pressure fluctuations
U_∞	= speed of body through fluid (or fluid past body)
$\|S(\vec{k},\omega)\|^2$	= spatial and temporal response of wave-vector filter in Fourier space
ω	= radian frequency, $2\pi f$
ω'	= specific value of radian frequency
$\phi(\vec{k},\omega)$	= spectral density of turbulent pressure fluctuations

1. INTRODUCTION

The degree to which the turbulent boundary layer (TBL) on the surface of a vehicle is a noise source problem depends on how the various spatial and temporal scales in the TBL match the spatial and temporal scales of the structure. Most of the energy in the TBL is contained in that portion which convects along the surface at a speed about 2/3 of the free-stream speed, the convection speed U_c. While the pressure fluctuations in the convective region are quite intense, their spatial and temporal scales do not match well with the scales of typical large structures. In other regions, the pressure fluctuations are much weaker, but the scales do match well with large structures and can be the dominant source of structural response. However, all scales contribute to the TBL flow-noise problem, and each situation must be examined to determine the importance of the various regions of the TBL. In attempting to devise means of mitigating the adverse effects of the TBL, it is desirable to have an analytical description that can be used for making predictions. Turbulence is a nonlinear phenomenon, however, and it has not been possible to generate analytical models from first principles to describe turbulent pressure fluctuations. At present, semi-empirical analytical models are used for prediction purposes.

Over the past 25 years, experimenters have generated a large body of data on turbulent boundary layer pressure fluctuations [1,2]. Most of these data have been obtained as a function of length and time or length and frequency, and most of these data have been obtained for the convective region with its strong signals. It is frequently more illuminating to study the problem in terms of the Fourier transform variables, the vector wave number (or wave vector) $\vec{k}$ and the radian frequency ω [3]. Very little data have been obtained directly as a function of wave number and frequency [4-10].

Some numerical transformations of data to wave-number-frequency space have been performed [11,12], but these transformations require assumptions that may not be generally valid. The data used for these transformations were obtained using two pressure transducers flush-mounted in a boundary at various separation distances. Cross-correlation and cross-spectral density techniques were used to analyze the data. Because the magnitudes of the levels in the region of non-convective wave numbers are so low, the data do not permit extrapolations into these regions to be carried out with confidence.

Wave-vector filters provide a means of decomposing the turbulent boundary layer pressure field directly as a function of the Fourier variables, wave number, and frequency [3]. This paper will describe the wave-vector filter technique, discuss some of its advantages, particularly for measurements in the non-convective region, and discuss some of the problems that can be encountered. Some discussion of facility requirements for making measurements in the region of non-convective wave numbers is also included.

2. THE WALL PRESSURE FIELD

For a wall pressure field that is statistically homogeneous and stationary, the cross-correlation of the pressures at two points on the boundary is defined as

$$R(\vec{x},t) = \langle p(\vec{x'},t') \, p(\vec{x'}+\vec{x},t'+t) \rangle . \tag{1}$$

where the brackets $\langle \rangle$ represent a time average, $\vec{x}$ is the separation distance between the two points, and t is a time delay. The spectral density is obtained from $R(\vec{x},t)$ by taking the Fourier transform over space and time.

$$\phi(\vec{k},\omega) = (2\pi)^{-3} \iiint R(\vec{x},t) \, \exp[-i(\vec{k}\cdot\vec{x}-\omega t)] \, d\vec{x} \, dt , \tag{2}$$

where $i = \sqrt{-1}$, $\vec{k}$ is the vector wave number, ω is the radian frequency $2\pi f$, and the integration limits are from $-\infty$ to $+\infty$; unless otherwise stated, all integrations will be from $-\infty$ to $+\infty$. The inverse relationship is then

$$R(\vec{x},t) = \iiint \Phi(\vec{k},\omega) \exp[i(\vec{k}\cdot\vec{x}-\omega t)] \, d\vec{k} \, d\omega \ . \tag{3}$$

From equations (1) and (3), the overall mean-squared pressure at a point on the boundary is simply

$$\langle p^2(\vec{x}',t')\rangle = R(\vec{0},0) = \iiint \Phi(\vec{k},\omega) \, d\vec{k} \, d\omega \ . \tag{4}$$

Another quantity of interest is obtained from the Fourier transform of the auto-correlation $R(\vec{0},t)$,

$$\Phi(\omega) = \iint \Phi(\vec{k},\omega) \, d\vec{k} \ . \tag{5}$$

The quantity $\Phi(\omega)$ is the frequency spectrum that one attempts to measure by frequency filtering the output of a single, flush-mounted pressure transducer. In any measurement, however, the properties of the measuring instrument must be taken into account. For example, rather than $\Phi(\vec{k},\omega)$ or $\Phi(\omega)$, one actually obtains

$$\Phi_M(\vec{k},\omega) = |S(\vec{k},\omega)|^2 \, \Phi(\vec{k},\omega) \ , \tag{6}$$

and

$$\Phi_M(\omega) = \iint |S(\vec{k},\omega)|^2 \, \Phi(\vec{k},\omega) \, d\vec{k} \ , \tag{7}$$

where $|S(\vec{k},\omega)|^2$ describes the spatial and temporal response characteristics of the measuring instrument.

Past measurements of $R(\vec{x},t)$ have shown an approximate exponential decay in both the x_1 and x_3 directions, with the decay in the x_3 direction being much faster. The longitudinal correlations maximize at time delays corresponding to a speed about 2/3 the mean flow speed. This implies that the conjugate function $\Phi(\vec{k},\omega)$ should vary more rapidly with k_1 than with k_3 and should peak at some value of the frequency ω. With the assumption of separability, the spectral density should have a form somewhat like

$$\Phi_1(\vec{k},\omega) = \Phi_1(k_1;\omega-k_1 U_c) \, \Phi_3(k_3) \ , \tag{8}$$

where U_c is the convection velocity at which the pressure fluctuations are carried forward by the mean flow. The dependence on k_3 should be symmetric and slowly varying. The remaining discussion will concentrate on the more interesting dependence on k_1 and ω. The coordinate system is illustrated in Figure 1.
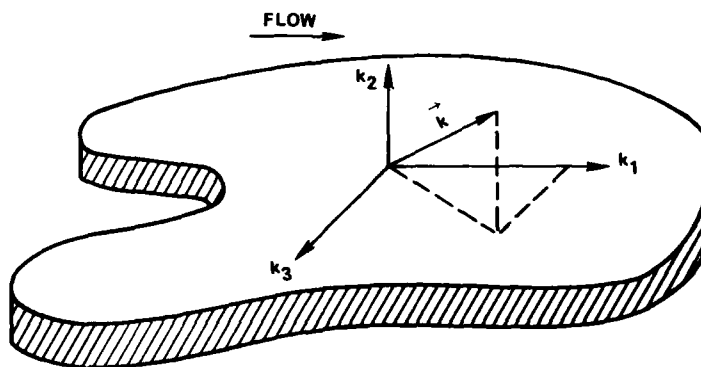

Figure 1 - Wave Number Coordinate System

The essential features of $\Phi(k_1,\omega)$ are illustrated in Figures 2 and 3. In Figure 2, the curves represent isobars of the magnitude of $\Phi(k_1,\omega)$. The line passing through the curves corresponds to $\omega = k_1 U_c$ and represents the convection speed. The magnitude of $\Phi(k_1,\omega)$ is greatest along this line. This region of large magnitude for the spectral density is termed the convective region. The line to the left in the figure corresponds to $\omega = k_1 c$, where c is the speed of sound in the fluid. If θ is the angle between the k_1-axis and the direction of propagation of a wave traveling at the speed of sound, then the trace wave number is $k_1 = |\vec{k}| \cos\theta$, where $|\vec{k}| = \omega/c$. Thus, k_1 is always less than or equal to ω/c for acoustic waves. The spectrum for such waves will lie along the sonic line if they are traveling in the k_1-direction and between the frequency axis and the sonic line, otherwise. This region is termed the super-sonic region. (Properly, Figure 2 should show four quadrants, with a line at $\omega = -k_1 c$ in the second quadrant, and with quadrants 3 and 4 being the images of quadrants 1 and 2, respectively. This would account for waves propagating upstream and the fact that ω can be negative.) The region in Figure 2 that lies between the isobars and the sonic line is termed the region of non-convective wave numbers, or low wave number region. This is a region of resonant response for many vehicles of interest.
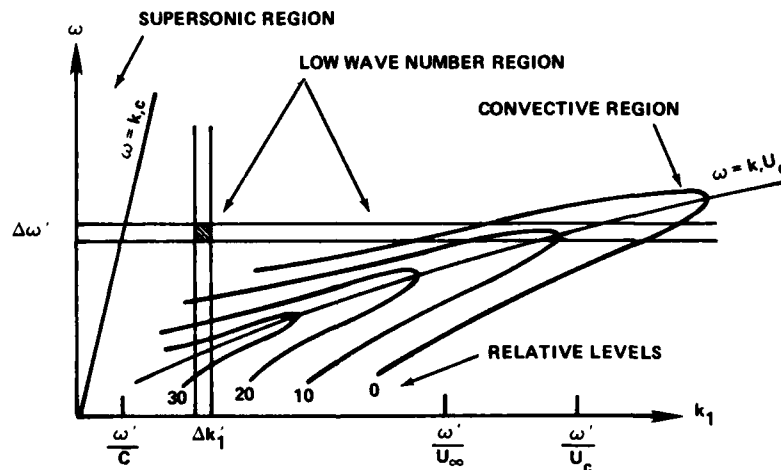
Figure 2 - Spectral Density Isobars

The variation in magnitude of $\Phi(k_1,\omega)$, as a function of k_1 at a particular frequency ω', is shown in Figure 3. The magnitude of $\Phi(k_1,\omega')$ in the supersonic region $-\omega/c < k_1 < \omega/c$ is unknown. Measurements in this region require an extremely quiet facility, since the spectrum of any extraneous acoustic noise is also in this region. If all extraneous noise in a facility traveled in the mean flow direction, the spectrum for the facility noise would lie on the sonic line in Figure 2 and would be seen as a spike at ω'/c in Figure 3. Experimental data for the low wave number region, $\omega/c < k_1 < \omega/U_\infty$, where U_∞ is the mean flow speed, are limited but do indicate that the magnitude of the spectral density is very small in this region [5-10]. The magnitude of the spectral density is significantly higher in the convective region, near $k_1 = \omega/U_c$, and is the region, therefore, about which most is known.

The determination of $\Phi(\vec{k},\omega)$ cannot be carried out successfully with a single flush-mounted pressure transducer. The output of the transducer will depend on its wave number response in accordance with equation (7). The wave number response of a single transducer is inversely proportional to its dimensions. If the transducer is small enough so that its wave number response extends to values

26

of $k_1 > \omega/U_c$, then the output will be dominated by the convective components. On the other hand, if the transducer is large, it will respond much less to the convective components but will not reject them completely. In both cases, the output will also include sonic and supersonic contributions.

Figure 3 - Regions of Boundary Layer Pressure Field
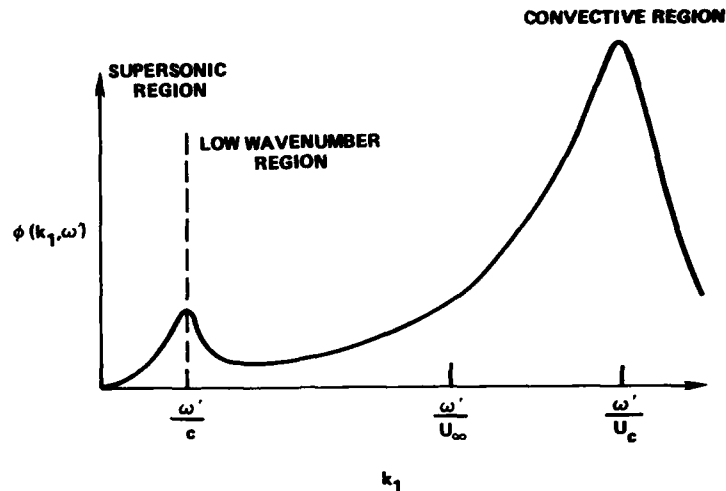
As in Figure 2, only the region of positive k_1 is shown in Figure 3. While this is the case for a number of the figures in this report, one must keep in mind that the negative region exists and that some of the functions are symmetric about $k_1 = 0$. It is sufficient for much of the following discussion to use only the positive k_1-region for illustration. Proper interpretation, however, requires a more thorough look at the functions in equation (7). For example, had the spectral density been shown for $-k_1$ in Figure 3, the levels would have been low and would not have shown a peak at $-\omega'/U_c$, since the spectral density is not symmetric about $k_1 = 0$. For a small single transducer whose output is dominated by convective components, the negative region is probably not important. For a wave-vector filter tuned to measure the spectral density in the low wave number region, the magnitudes in the negative region are comparable to those in the positive region and must be taken into account.

3. WAVE-VECTOR FILTER TECHNIQUE

In order to decompose the pressure field into its spatial and temporal components as represented by the wave number and frequency variables, we need an instrument that senses the energy in a frequency band centered at some frequency ω' and in a wave number band centered at some wave number k_1. As frequency filters are readily available, the problem centers on developing a spatial filter with appropriate characteristics which are known. The result is shown in the schematic in Figure 2 by the bands labeled $\Delta\omega$ and Δk_1 which intersect at some point in the $k_1-\omega$ plane. If the bandwidths are sufficiently small, the output of the combined system is the magnitude of the spectral density at ω' and k_1. An instrument specifically designed for this type of measurement is termed a wave-vector filter.

Flush-mounted pressure transducers are used to perform the spatial Fourier analysis of the signal. The output from the pressure transducers is then passed through the frequency filter which performs the temporal Fourier analysis of the signal.

In principle, any device with spatial extent that responds to a pressure excitation is a candidate as a wave-vector filter. In practice, the utility of the device depends on one's ability to define that response. Arrays comprised of condenser microphones [5,6,9,10] and mechanical structures comprised of thin plates or membranes [7,8] are examples of instrumentation that have been used. The sizes, spacing (for arrays), and other characteristics are carefully chosen to provide the desired wave number response. Both types have been mounted flush in the wall beneath a turbulent boundary layer and the outputs analyzed to infer the magnitude of the spectral density. Reference 8 provides a discussion of the use of membranes and thin plates as wave-vector filters. This report will concentrate on the use of linear arrays.

Figures 4 and 5 illustrate how the response function $|S(\vec{k},\omega)|^2$ can be tailored. Figure 4 shows the wave number response of a single flush-mounted pressure transducer. The curve is for a circular sensing area with a spatial sensitivity that is nonuniform across the sensing area. It is clear that the single flush-mounted pressure transducer acts like a low-pass filter to wave numbers. It senses all wave number components up to some value, and its response decreases rapidly above that point. For discussion purposes, the first zero will be used as the cutoff point rather than the 3 dB down point. The response curve shown in Figure 4 decreases as $|\vec{k}|^{-5}$ beyond the first zero. While the response at the higher wave numbers is very weak, it is not zero. As equation (7) shows, the output is the integrated product of the response function and the field function. If the field is intense at a high wave number where the response is weak, its contribution to the output can still be sufficient to dominate the result.
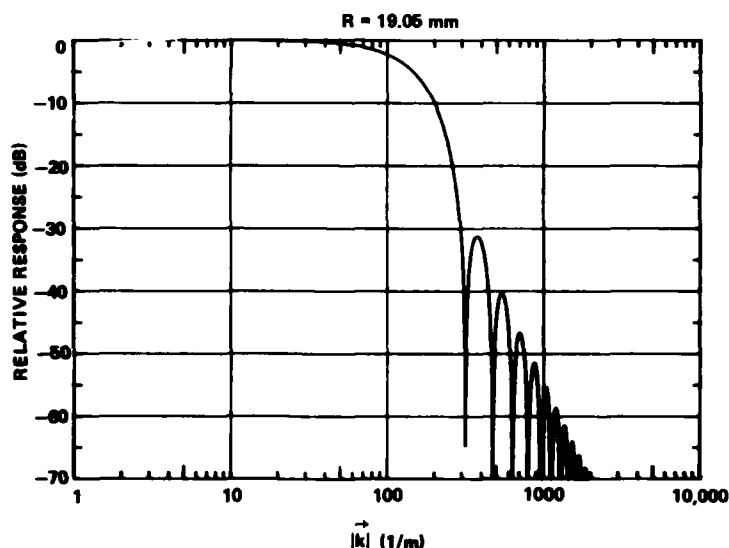
Figure 4 - Wave Number Response for Single, Circular Transducer
with a Non-Uniform Facial Sensitivity.

Figure 5 illustrates the response curve for a linear array made up of six flush-mounted pressure transducers of the type in Figure 4 aligned in the k_1-direction. An identical response exists for $-k_1$, due to symmetry of $|S(k_1,\omega)|^2$ about $k_1 = 0$. The total response for the array is the product of the single element response and the sinusoidal response due to the multiplicity of elements. The response of the large single element is utilized to reduce the magnitude of the array response at the higher wave numbers. The response curve in Figure 5 is for an array with the signals added out of phase; that is, plus, minus, plus,

28

minus, etc. This produces a response curve for the array that is most sensitive to wave numbers in a band centered at $\pm k_1 = \pi/d$, where d is the center-to-center separation distance between transducers. Note that the response is not a simple pass band with sharp skirts as can be had with frequency filters. Rather, the response is a complicated function having many lobes which exist over a wide wave number range and which are fixed for a given set of conditions. Thus, while we have achieved a device that responds best to particular bands of wave numbers, it is at the expense of having a complicated response curve. In essence, we have the spatial equivalent of a digital frequency analyzer. The wave number $|\pi/d|$ corresponds to the Nyquist sampling rate for the spatial frequency. The single element response is the equivalent of an anti-aliasing filter. Unfortunately, it is not a good anti-aliasing filter, and we have a response existing at higher wave numbers that can lead to problems in the interpretation of the data.
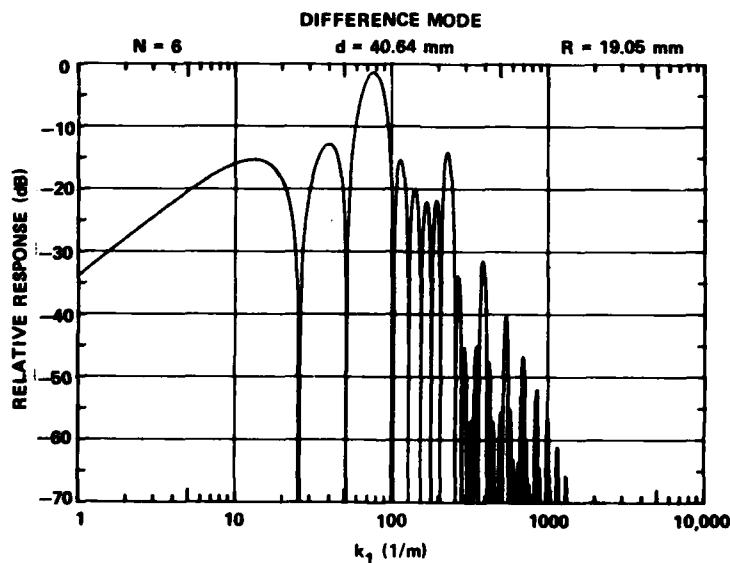
Figure 5 - Wave Number Response of a Linear Array

4. LINEAR ARRAYS AS WAVE-VECTOR FILTERS

The use of linear arrays as wave-vector filters involves a number of considerations that must be accounted for when designing the array. Table 1 illustrates a number of factors that affect the wave number response.

Table 1 - Parameters Affecting the Wave Number
Response of Linear Arrays

1. Spacing of Transducers, d
2. Method of Summing Transducer Outputs
3. Size and Shape of Sensitive Area
4. Length of Array, Nd (equivalent to number of transducers N, if d is constant)
5. Point Response of Sensitive Area
6. Shading
7. Deviations in Sensitivity and Phase

29

4.1 Spacing of Transducers

Figure 6 illustrates the effect of spacing and method of summing outputs. When an array is made up of a number of transducers spaced equally with center-to-center spacing d, the equations governing that portion of the wave number response due to the multiplicity of elements are the same as for diffraction gratings. Major response lobes (grating lobes) occur at multiples of $\pm k_1 d/\pi$, and minor response lobes (side lobes) occur in between. The magnitude of the side lobes decreases and their number increases as the number of elements increases. Since wave number is inversely proportional to distance, d must be large to perform measurements at low wave numbers and small to perform them at high wave numbers. Measurements at very low values of wave number may require a wave-vector filter array of impractical length, even if the number of elements is not large. Conversely, measurements at high wave numbers may require such small values of d that it is impractical to construct transducers that are sufficiently small.
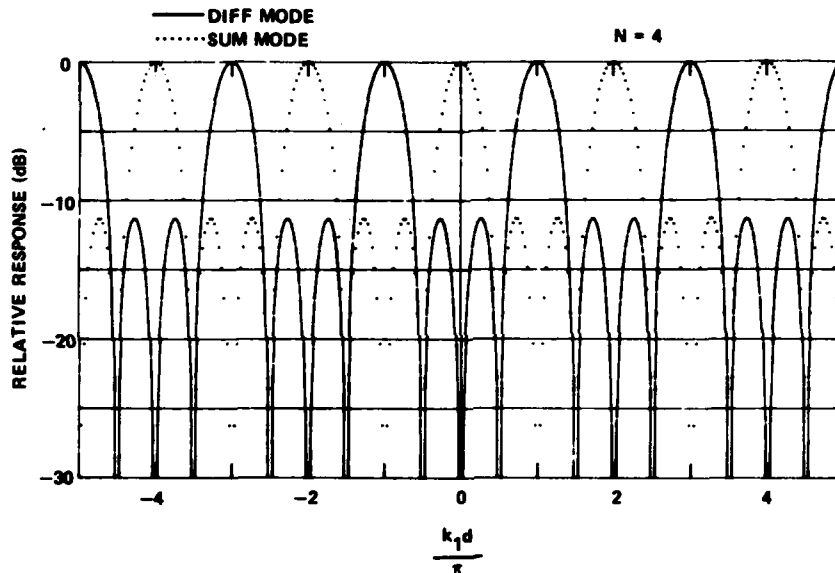
Figure 6 - Effect of Spacing and Method of Summing Outputs

4.2 Method of Summing Transducer Outputs

Figure 6 shows two curves obtained with different methods of summing the outputs. A four-element array has been assumed. The dotted curve, labeled SUM, is the response when the outputs of the array elements are added together directly (in phase). This produces a main response lobe at $k_1 = 0$ and additional grating lobes at even multiples of $\pm k_1 d/\pi$. The main response lobe is most sensitive to plane waves striking the surface normally, since the trace wave number for such waves is zero.

The second method of summing is the more valuable method when using the array as a wave-vector filter to measure the TBL pressure field components. In this mode of operation, labeled DIFF, the outputs of the array elements are added alternately out of phase, plus, minus, plus, minus, etc. This provides grating lobes at odd multiples of $\pm k_1 d/\pi$. Note that the response at $k_1 = 0$ is zero and that there are nulls between zero and $\pm k_1 d/\pi$. If a facility is designed so that all facility noise travels in the flow direction (or in the negative flow direction), then the nulls between 0 and $\pm k_1 d/\pi$ will be coincident

with the sonic lines at some frequency. In principle, all facility noise can then be cancelled.

It is also possible to steer the array to provide wave number response curves between those shown in Figure 6 [13]. This can be accomplished by adding time delays between the transducer outputs, or by adding phase shifts between the outputs after they have been individually Fourier transformed, and then summing. This can be readily accomplished with a digital computer processing system. The use of time delays allows one to steer the response lobe at $k_1\pi/d$, for example, along the $\omega = k_1c$ line. This technique, which is analagous to sonar processing, allows one to investigate such phenomena as facility noise. The resulting wave number response is frequency dependent, however, and one must use a different response curve for each frequency of interest. The technique of adding phase shifts to the Fourier transformed outputs of individual sensors prior to summing yields a wave number response that is independent of frequency. The curves shown in Figure 6 correspond to a phase shift of zero (SUM) and a phase shift of π (DIFF). For phase angles in between, the wave number response is not symmetric about $k_1d/\pi = 0$.

4.3 Size and Shape of Sensitive Area

The response illustrated in Figure 6 is not very useful due to the multiplicity of major wave number response bands. However, the effect of the finite side of the transducer, as shown in Figure 4, can be utilized to reduce the response of the lobes for wave numbers greater than $\pm k_1d/\pi$. The idea is to choose the size and spacing of the transducers so that the first null in the single element response curve of Figure 4 coincides with the main response lobes occurring at $\pm k_1d/\pi$. Since the total wave number response of the wave-vector filter array is the product of the single element response and the grating lobe response, the response lobes at $\pm 3k_1d/\pi$ will be cancelled, and all higher lobes will be strongly attenuated by the single element response. The result is a device designed to respond well to two bands of wave numbers and to respond very weakly to facility noise. The response of a square transducer with a uniform response kernel is proportional to $(\sin L/L)^2$, where L is related to the size of the transducer. The response at high wave numbers, relative to the transducer dimensions, decreases as $(k_1L)^{-2}$. A circular transducer with a uniform response kernel has a response proportional to $[J_0(L)/L]^2$. The response at high wave numbers, relative to the transducer dimensions, decreases as $(k_1L)_1^{-3}$.

4.4 Length of Array

The effect of increasing the number of elements in the array (thereby increasing its length) is shown in Figure 7. The wave number bandwidth of the main response lobes is inversely proportional to the total length of the array, Nd. The effect on the main lobe at k_1d/π of increasing the number of elements from 2 to 12 for an array operating in the difference mode is evident. Significant decreases in the bandwidth essentially require a doubling of the number of elements, thereby doubling the length of the array. The table of numbers to the right in Figure 7 show how the percentage bandwidth at k_1d/π decreases with increasing N. Several practical problems immediately present themselves. A very narrow wave number bandwidth will require a long array. The Farabee-Geib measurements [6,9,10] using a spacing of 2.7 cm, and a percent bandwidth would have required an array 5 meters long. Space for such a long array was not available. The cost for such an array would be prohibitive, and the experimental difficulties would be immense. In addition, the boundary layer would be changing in thickness over the long distance. For laboratory measurements of the TBL, practical wave-vector filter arrays lie in the range of 4 to 20 elements. To date, measurements have not been made with linear arrays having more than 12 elements.

An additional advantage of increasing the number of transducers in the array is a gain in the signal-to-noise ratio. The sensitivity of the array

31

increases as 20 log N, while the electrical noise of the array increases as 10
log N.

DIFFERENCE MODE

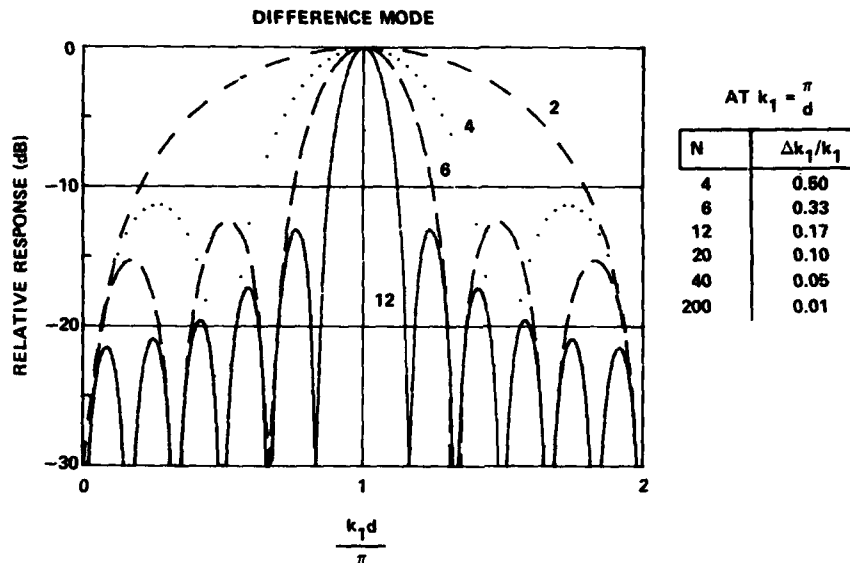| N	$\Delta k_1/k_1$
4	0.50
6	0.33
12	0.17
20	0.10
40	0.05
200	0.01

AT $k_1 = \frac{\pi}{d}$

Figure 7 - Effect of Number of Elements on Wave Number Bandwidth

4.5 Point Response of Sensitive Area

The graph in Figure 4 is for a circular transducer with a non-uniform
response kernel. The non-uniform response produces two effects, one desirable
and one undesirable. The response at high wave numbers depends on the derivative
of the point-sensitivity function at the transducer edge [5]. For the case
shown, the non-uniformity results in the desirable property that the response
decreases as $(k_1 L)^{-5}$ and, therefore, provides greater attenuation of convective
components. The undesirable property is an increase in the value of the wave
number for the first null. The effect of this is evident in the array response
curve shown in Figure 5. The null in the single element response did not cancel
the response lobes at $\pm 3k_1 d/\pi$ even though the transducers were closely packed.
The transducers would have had to overlap for the single element null to have
cancelled the lobes at $\pm 3k_1 d/\pi$. This is a serious problem. It is quite
possible for the output of the array to be dominated by the response lobes at
$\pm 3k_1 d/\pi$ rather than the lobes at $\pm k_1 d/\pi$. It is mandatory to know the wave
number response of the wave-vector filter in order to properly interpret data.

4.6 Shading

Another factor that can be used to control the wave number response of the
wave-vector filter array is shading. Spatial shading, which is not illustrated,
is obtained by varying the separation distances between transducers. This type
of shading can be used to eliminate the grating lobes at the higher wave numbers.
There is, of course, a tradeoff. Spatial shading increases the amplitude of the
side lobes.

Amplitude shading is illustrated in Figure 8. This type of shading reduces
the magnitude of the side lobes at the expense of increasing the bandwidth of the
main response lobes. Various types of amplitude shading exist. Figure 8 illus-
trates binomial shading. The amplitude weights for this type of shading are
proportional to the coefficients of a binomial expansion. Binomial shading has

32

the advantage of eliminating the minor response lobes (side lobes) that normally occur between the major response lobes (grating lobes). Another type of shading is Chebyshev which gives the narrowest major response lobe bandwidth for a specified minor response lobe amplitude.

DIFFERENCE MODE

N = 6   d = 40.64 mm   R = 19.05 mm

k$_1$ (1/m)
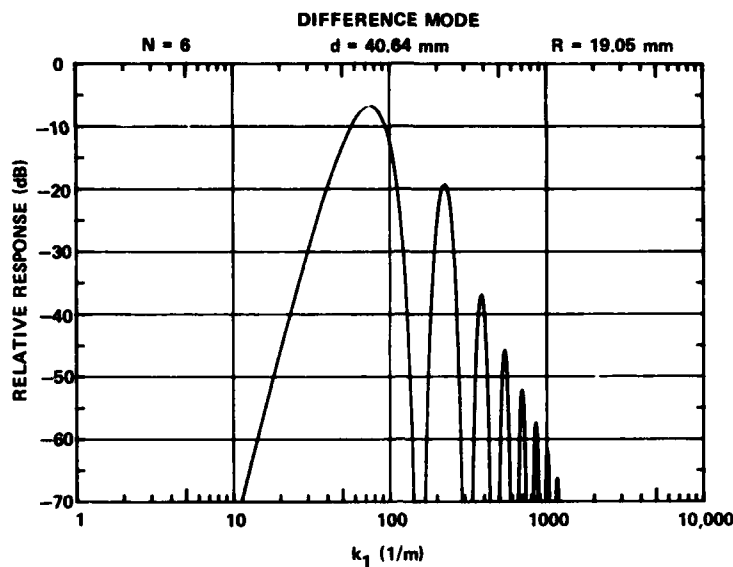
Figure 8 - Effect of Amplitude Shading with Binomial Weighting on Wave Number Response of Figure 5.

4.7 Deviations in Sensitivity and Phase

Deviations in the sensitivities or the phase between transducers do not affect the main response lobe very much. They do, however, strongly affect the cancellation regions [14]. Figure 9 uses the sum mode of operation to illustrate

SUM MODE, N = 6

BINOMIAL SHADING WITH ±0.5 dB DEVIATIONS

BINOMIAL SHADING

k$_1$d/π

Figure 9 - Effect of Deviations in Sensitivity on Cancellation.

33

the effect of deviations in sensitivity of ± 0.5 dB from the ideal in a six-element array using binomial shading. The theoretically infinite cancellation at k_1d/π has been reduced to about 20 dB. Deviations of only ± 0.1 dB reduce the cancellation to about 35 dB. While not illustrated, deviations in phase of only a few degrees between transducers have a similar effect. This represents a very severe experimental problem. It requires knowledge of the differences between transducers to a greater accuracy than one normally has to account for in acoustic experiments, if the beneficial effects of cancellation are a requirement.

Figure 10 shows how amplitude deviations of ± 0.5 dB affect the binomial-shaded response curve of Figure 8. The total rejection of signals between 1 and 10 inverse meters has been reduced to about a 24 dB rejection. It is evident that one must use shading techniques with care if they are being counted on for cancellation of portions of the signal.

DIFFERENCE MODE

N = 6   d = 40.64 mm   R = 19.05 mm

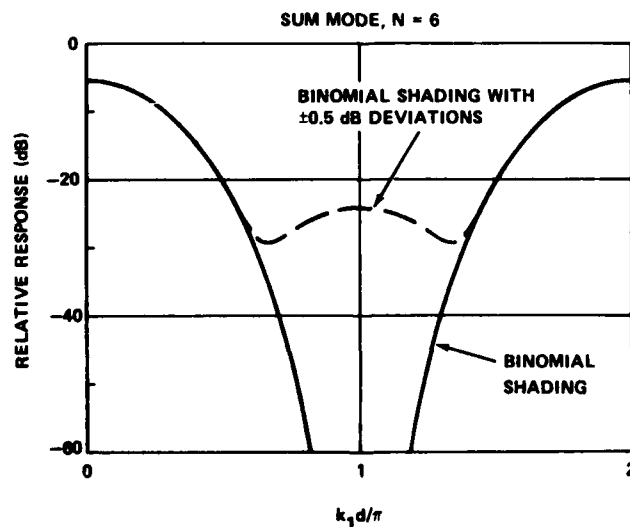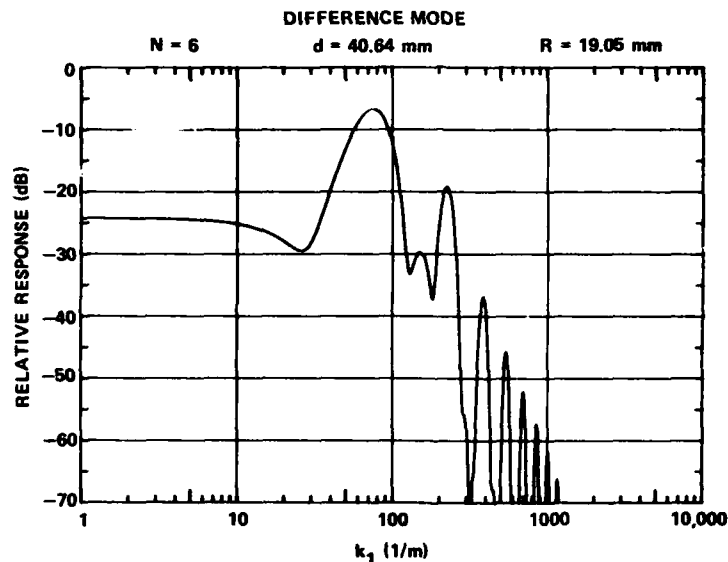Figure 10 - Effect of Deviations in Ideal Sensitivitaies
of ± 0.5 dB when Binomial Shading is Used.

5. FACILITIES

One of the problems encountered when planning an experiment to measure the TBL wall pressure field is the choice of facilities. This is especially true for measurements in the non-convective region where the magnitudes of the spectral density are very small. Air facilities are usually quieter than water facilities and it is usually easier to work in air. However, Reynolds numbers are much lower in air than in water and some experiments require water.

Figure 11 presents an example of the problems that can be encountered in water facilities. The 36-inch water tunnel at the David Taylor Naval Ship R&D Center (DTNSRDC) is a candidate for some type of measurements. Measurements in the non-convective region would be very difficult in this facility. The background noise levels in the facility are high due to its basic construction and the many pieces of machinery that are required for its operation. The background levels are essentially speed independent up to 10 m/sec and increase at higher speeds.

Two curves showing predicted low wave number levels are also shown in Figure 11. The predicted levels are from an equation Farabee and Geib [6] fitted to dimensionless data,

$$\frac{\Phi(\vec{k},\omega)_L \; U_\infty}{q^2 \delta^{*3}} = 2\times10^{-9} \left(\frac{\omega\delta^*}{U_\infty}\right)^{-4} \tag{9}$$

where $\Phi(\vec{k},\omega)_L$ is the measured level for the spectral density in the region of the predicted pressure levels because the two arrays have different wave number responses. Cancellation techniques would obviously have to be employed in order to reduce the effects of the background noise.
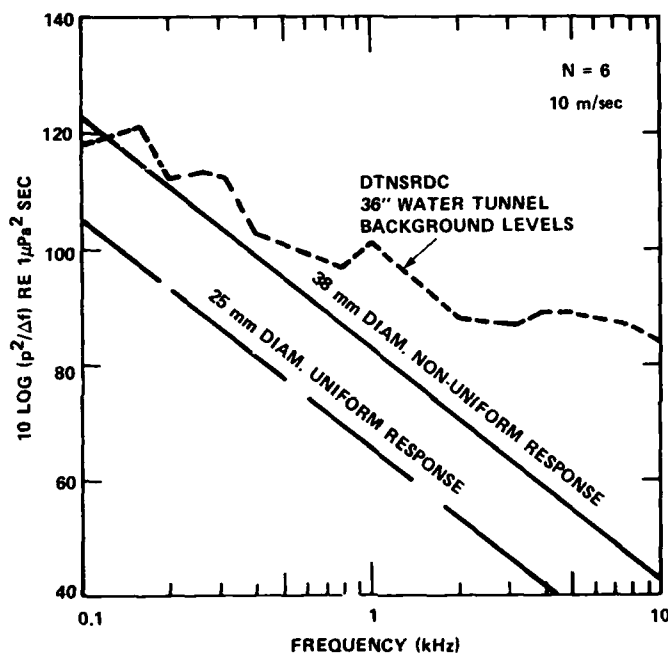
Figure 11 - Predicted Low Wave Number Levels in Water for
Two Different 6-Element Linear Arrays.

Water tunnels do have advantages. Among these is the long time available for data collection where conditions can be set and held constant. The advantages could lead one to consider a facility such as the 36-inch water tunnel even with the high background noise levels. A carefully planned experiment with accurate amplitude shading might succeed.

Other water facilities exist at DTNSRDC and elsewhere. They range from blowdown pipe facilities to water tunnels to buoyant body facilities. In addition to the background noise characteristics in these facilities, each has its own set of limitations such as size, type of flow, and length of time for data collection. Quiet buoyant body facilities, for example, can be found. However, the instrumentation has to run remotely, and the data collection time may be very short, leading to problems with statistical accuracy.

6. CONCLUDING REMARKS

The intent of this report has been to provide an introductory overview of the utilization of linear arrays of flush-mounted pressure transducers as wave-vector filters to measure turbulent boundary layer pressure fluctuations. The technique has been introduced and the dependence of the wave number response on various parameters has been discussed. An attempt has been made to point out a number of practical problems that must be considered when making wave-vector filter measurements.

Wave-vector filters are a useful measurement tool. They act to Fourier transform the spatial variable in the same manner that frequency filters act to Fourier transform the temporal variable. The output of the combination is a measurement that is a function of the Fourier variables, wave number and frequency. This is quite useful since many analytical studies are carried out in Fourier space, and direct comparisons can be made between predictions and measurements. Wave-vector filters are not a panacea, however. There are many factors that must be considered when designing an experiment that utilizes these devices. Design tradeoffs and the interplay between parameters must be considered.

At the present time, we have only reasonably adequate knowledge of the TBL pressure field for the convective region of spectral space. Our knowledge in the other regions, which are regions of great significance for naval applications, is insufficient. We need knowledge of the levels and the dependence on wave number and frequency in the non-convective regions of spectral space. We also need knowledge of the dependence on boundary layer parameters. Wave-vector filters are one of the better tools for obtaining this information.

ACKNOWLEDGMENT

REFERENCES

1. Willmarth, W.W., "Pressure Fluctuations Beneath Turbulent Boundary Layers," Annual Review of Fluid Mechanics, Vol. 7, Annual Reviews, Inc., Palo Alto, CA, 1975, pp. 13-38.

2. Ross, D., Mechanics of Underwater Noise, Pergamon Press, New York, 1976, pp. 184-196.

3. Maidanik, G., and Jorgensen, D.W., "Boundary Wave-Vector Filters for the Study of the Pressure Field in a Turbulent Boundary Layer," Journal of the Acoustical Society of America, Vol. 42, Aug. 1967, pp. 494-501.

4. Geib, F.E., Jr., and Remmers, G.M., "Measurement of Wall Pressure Fluctuations with a Wave-Vector Filter," Naval Ship R&D Center Report 3370, Apr. 1970.

5. Blake, W.K., and Chase, D.M., "Wavenumber-Frequency Spectra of Turbulent Boundary-Layer Pressure Measured by Microphone Arrays," Journal of the Acoustical Society of America, Vol. 49, Mar. 1971, pp. 862-877.

6. Farabee, T.M., and Geib, F.E., Jr., "Measurement of Boundary Layer Pressure Fields with an Array of Pressure Transducers in a Subsonic Flow," David Taylor Naval Ship R&D Center Report 76-0031, Mar. 1976.

7. Jameson, P.W., "Measurement of the Low Wavenumber Component of Turbulent Boundary Layer Pressure Spectral Density," proceedings of the Symposium on Turbulence in Liquids, University of Missouri, Rolla, Sep. 1975, pp. 192-200.

8. Martin, N.C., and Leehey, P., "Low Wavenumber Wall Pressure Measurements Using a Rectangular Membrane as a Spatial Filter," Journal of Sound and Vibration, Vol. 52, No. 1, May 1977, pp. 95-120.

9. Geib, F.E., and Farabee, T.M., "Measurements of Boundary-Layer Pressure Fluctuations at Low Wave Number on a Smooth Wall," paper presented at the 91st Meeting of the Acoustical Society of America, Apr. 1976.

10. Farabee, T.M., and Geib, F.E., "Measurements of Boundry-Layer Pressure Fluctuations at Low Wave Number on a Rough Wall," paper presented at the 91st Meeting of the Acoustical Society of America, Apr. 1976.

11. Wills, J.A.B., "Measurements of the Wavenumber/Phase Velocity Spectrum of Wall Pressure Beneath a Turbulent Boundary Layer," Journal of Fluid Mechanics, Vol. 45, 1970, pp. 65-90.

12. Maestrello, L., "Use of Turbulent Model to Calculate the Vibration and Radiation Responses of a Panel, with Practical Suggestions for Reducing Sound Level," Journal of Sound and Vibration, Vol. 5, May 1967, pp. 407-448.

13. Maidanik, G., "Flush-Mounted Pressure Transducer Systems as Spatial and Spectral Filters," Journal of the Acoustical Society of America, Vol. 42, No. 5, Nov. 1967, pp. 1017-1024.

14. Maidanik, G., "Influence of Deviations and Variations in Transducers on the Filtering Actions of Spectral Filters," Journal of the Acoustical Society of America, Vol. 55, No. 1, Jan. 1974, pp. 170-183.

AN INNOVATIVE FAST FOURIER TRANSFORM ARRAY TECHNIQUE FOR ')W WAVE-NUMBER MEASUREMENTS OF THE TURBULENT BOUNDARY LAYER FLUCTUATING PRESSURE FIELD

T. H. Hodgson and R. F. Keltie
Center for Sound and Vibration
North Carolina State University
Raleigh, North Carolina

ABSTRACT

The structure of the wall pressure field in a turbulent boundary layer as described by the three-dimensional spectrum $\phi_p(k_1,k_2;\omega)$ continues to generate considerable interest as a result of a variety of practical problems such as the coupling of the large scale flow structure to structural modes, analytical modeling of acoustic problems associated with structural radiation and sonar detection, and in the determination of controlling factors in turbulent boundary layer drag and flow noise.

An innovative measurement method is described for the determination of important parameters in the longitudinal wavenumber, k_1, and frequency, ω, spectrum $\phi_p(k_1;\omega)$ of the wall pressure. This spectrum has a dominant convective ridge of energy (basically hydrodynamic) with a considerably weaker region at supersonic phase speed corresponding to sound radiation. To date the low wavenumber or low frequency part of the spectrum has created a difficult measurement problem in that the energy levels are much lower than that of the convective ridge and also because of the complicated relationship between frequency and wavenumber in this region.

The method presented, which is a significant improvement on previous wavenumber filter methods, uses a Fast-Fourier-Transform approach in both the frequency and wavenumber domains. By use of a processed array of fifty transducers it is demonstrated that pressure spectrum measurements may be made at higher resolution than previously reported in the literature, while rejecting the convective pressure ridge by at least 60 dB and the sonic component by 30 dB. This should lead to a more accurate measurement of the all important low wavenumber plateau region of the spectrum in nearly anechoic experiments.

1. INTRODUCTION

Properties of the fluctuating pressure field under a turbulent boundary layer (TBL) flow have been studied to date for a period of over twenty years. The study of the pressure field rather than the turbulent velocity field came about from interest in the acoustic radiation generated by turbulent shear flows over surfaces in general.

As a result of the pioneering work by Townsend [1], it is now established that turbulent boundary layers may be characterized by two length scales, namely the boundary layer thickness δ (or displacement thickness δ^*) and the wall similarity length scale ν/u_τ, where ν is the fluid kinematic viscosity and u_τ is the mean wall shear velocity. The frequency of the wall pressure fluctuations may be non-dimensionalized to form a Strouhal number using either of these length scales. Over an intermediate range of wavenumbers of the turbulence the frequency spectrum of the wall pressure is known to depend on $\omega^* = \omega\delta^*/U_\infty$ where U_∞ is the flow velocity at the edge of the boundary layer, while at high frequencies the frequency spectrum depends on $\omega\nu/u^2_\tau$, see Willmarth [2]

The relation between wavenumber and frequency at intermediate and high wavenumbers, order $k_1\delta^*\gg1$, is relatively simple. Space and time fluctuations of the pressure field are related by a convection velocity U_c in the longitudinal direction where U_c is a slowly varying function of k_1 and ω depending on the velocities of the particular eddies as they are positioned in the normal direction x_2 to the surface. An average value of U_c is $\simeq 0.8\ U_\infty$. This convective "ridge" in the k_1 wavenumber spectrum or frequency spectrum forms the dominant energy contribution to the wall pressure field. However the low wavenumber or low frequency part of the spectrum has always posed a great measurement problem particularly in that the energy levels are much lower and also because the relation between wavenumber and frequency is much more complicated being strictly governed by the Navier-Stokes equations. Although it can be argued that the large eddy structure, i.e. low wavenumber, of the TBL pressure field is only weakly viscosity dependent nevertheless the turbulent boundary layer as a whole is a complicated feedback mechanism with the large eddy structure controlling the energy dissipated at the wall. Thus this may explain why the wavenumber-frequency spectrum has not been accurately modeled by analytical methods at this time.

One of the early controversies regarding the wall pressure description at low wavenumbers was the nature of the aeroacoustic radiation mechanism from the TBL pressure field over a rigid plane surface. Phillips, and later Powell, had predicted that the dipole radiation due to the wall pressure term in the Lighthill aeroacoustic theory would be zero in the case of vanishing Mach number $M_\infty\to0$. Expressed another way, this would mean that the surface integral of the two-point wall pressure correlation coefficient R_{pp} taken over the plane would vanish. This might be regarded historically as the first major problem of understanding the TBL pressure field at low wavenumber. The measurement difficulties likely to be encountered in this problem and the design of several quiet TBL flow facilities was thoroughly discussed by Hodgson [3]. He concluded that it was never possible to satisfactorily remove the effects of low wavenumber turbulence in a wind-tunnel facility. Besides fan noise or nozzle noise, the small (but significant) acoustic radiation from the TBL pressure field after reflection from other surfaces would always cause problems for measurement at low wavenumbers. It is interesting to note that even modern anechoic facilities still cannot completely reduce the spurious large eddy, low wavenumber disturbances, see for instance Blake and Chase [4].

Hodgson's solution to answering the Phillips-Powell controversy was to measure the TBL pressure field on the wing of a high-performance sailplane (a Schleicher Ka6R) where the conditions were truly free-field and where the presence of long wavelength turbulence in calm air was greatly reduced [5]. For a mean pressure gradient close to zero, measurements of the spatial correlation coefficients taken from reference 5 are shown in Figure 1 for the longitudinal x_1, transverse x_3 and 45° directions. All three correlation measurements reduced to zero value at large separations between the two pressure transducers, order $10\ \delta^*$, thus demonstrating the very low level of extraneous low wavenumber disturbances present in the experiment. To within the order of experimental accuracy the correlation area, corresponding to the $k=0$ case, did indeed integrate to zero confirming the Phillips-Powell result of negligible dipole radiation at vanishing Mach number M_∞ (= 0.06 in the experiment). The corresponding frequency spectrum, shown in Figure 2, illustrated two interesting results. Firstly there was an extensive "flat" region at low frequencies with a consistency of the data never demonstrated in wind-tunnel results. Secondly these results, it is believed,

demonstrated for the first time some characteristics of the true low wavenumber portion of the spectrum in that a Fourier transform of the spatial correlation curve of Figure 1 in the x_1 direction yielded a $\phi_p(k_1)$ spectrum shown in Figure 3 which was not compatible at low k_1 with the low frequency part of the frequency spectrum. That is, because of the negative loop in the spatial correlation (required by the Phillips-Powell theorem), the $\phi_p(k_1)$ spectrum falls at low k_1. That is there was no longer a simple convective relationship at low values of wavenumber and frequency.
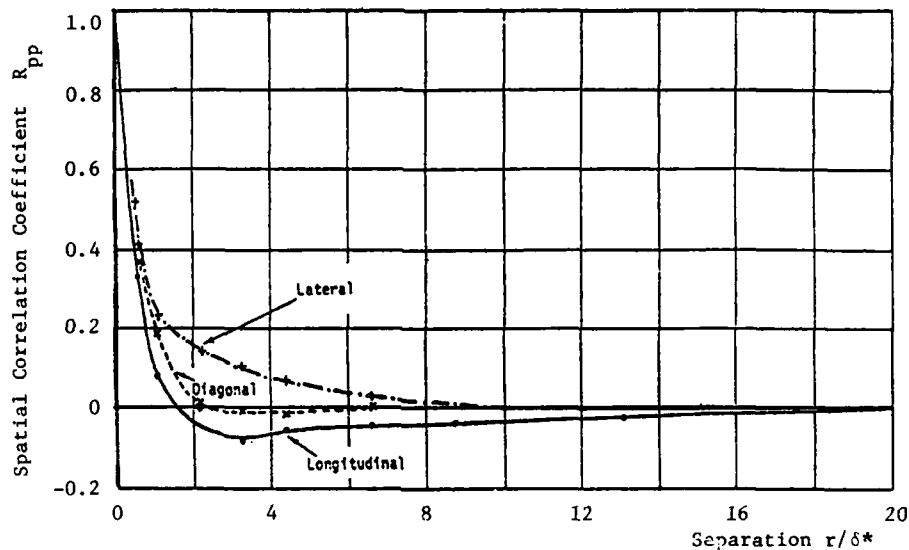

Fig. 1. Measurements of the longitutinal, transverse and 45° diagnonal TBL wall pressure spatial correlation coefficients on a sailplane, Hodgson ref. 5.
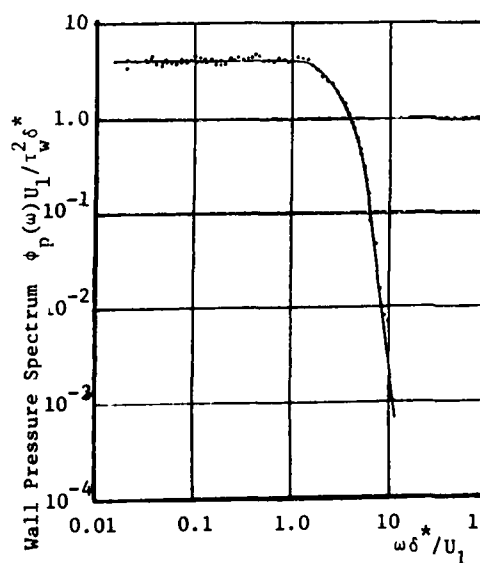

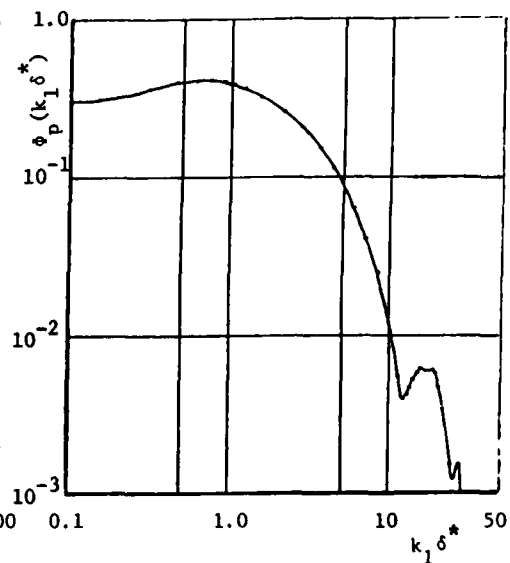Fig. 2. Measurement of TBL wall pressure frequency spectrum on a sailplane, Hodgson ref.5.

Fig. 3. Fourier transformed normalized TBL wall pressure wavenumber spectrum, Hodgson ref. 5.

41

2. THE WAVENUMBER-FREQUENCY SPECTRUM

The three-dimensional wavenumber-frequency spectrum $\phi_p(k_1, k_3; \omega)$ is the Fourier Transform of the space-time correlation coefficient $R_{pp}(r_1, r_3; \tau)$ where r_1 and r_3 are the spatial separations in the x_1, x_3 plane of the surface and τ is the time-delay between the two measurement pressure transducers. Recent interest has concentrated on the spectral shape of ϕ_p, particularly $\phi_p(k_1; \omega)$, since it is required in analytical solutions associated with both plate radiation and operation of sonar detection arrays. The nature of the $\phi_p(k_1, k_3; \omega)$ spectrum has been given by Ffowcs Williams [6,7] who extended the Phillips-Powell theory to small but finite Mach numbers. He identified the two separate sound radiating and hydrodynamic components of the TBL pressure field while reiterating Hodgson's experimental findings that any alteration in the acoustic environment would dramatically effect the low wavenumber part of the ϕ_p spectrum, emphasizing again the careful controls that must be made in order to measure the spectrum accurately. Ffowcs Williams was the first definitive work which illustrated a $\phi_p(k_1; \omega)$ spectrum with a strong convective ridge (basically hydrodynamic) and with a region of supersonic phase speed corresponding to sound radiation, see Figure 4 taken from reference 6. To date there has been considerable theoretical study of the complete three-dimensional wavenumber-frequency stectrum, see for instance Ffowcs Williams [7] and Chase [8]. In order to investigate the k_3 direction, transducers could be placed transversely to the flow direction as in reference 5. However, as Ffowcs Williams [7] has emphasized, actual quantitative measurement of the low-wavenumber plateau or its definite shape has not been achieved after some twenty-five years of study. So this paper concentrates on the spectrum shape in the k_1 direction where for a predominantly low Mach number flow most of the energy is concentrated around the k_1, axis, see reference 6 and 7.
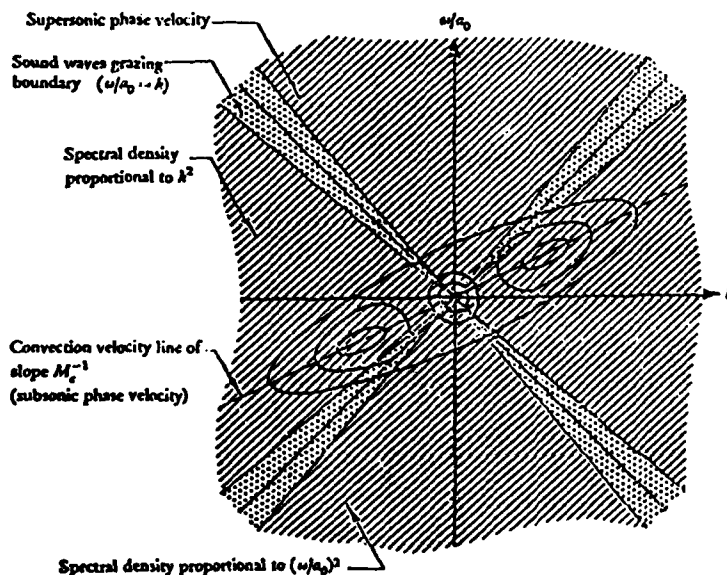

Fig. 4. Typical TBL wall pressure power spectrum for a predominantly subsonic flow, Ffowcs Williams ref. 6.

Ffowcs Williams predicted that at low wavenumbers below the convected ridge then the $\phi_p(k_1)$ spectrum integrated over all frequencies would vary as M^2 below a wavenumber of order M/δ^*. The low wavenumber portion of the spectrum was further analyzed by Bergeron [9], in particular the apparent singularity avoided by Ffowcs Williams at the acoustic critical wavenumber $k = \omega/c_o$ where c_o is the a͟c͟o͟u͟s͟t͟i͟c͟ velocity. By using a finite plate analysis Bergeron effectively re-m͟o͟v͟e͟d͟ t͟h͟e͟ singularity predicting a peak in the spectrum $\phi_p(k_1)$ with amplitude of o͟r͟d͟e͟r͟ ℓ/δ^* with bandwidth of order $\delta^*/M\ell$ where ℓ is likely to be the shorter d͟i͟m͟e͟n͟s͟i͟o͟n͟ of the finite-sized plate. Thus it is possible to understand why the $\phi_p(k_1; \omega_o)$ spectrum at given ω_o is, following Maidanik and Eister [10], likely to be of the form shown in Figure 5. The strong convective ridge is shown at $k_1 = \omega/U_c$ and the radiated sound peak at $k_1 = \omega/c_o$. The problem is to measure this $\phi_p(k_1; \omega)$ spectrum, where it has been mentioned previously that in wind-tunnels there is likely to be a problem around the acoustic peak due to radiated noise in the tunnel (since the disturbances travel at c_o) as well as low wave-number disturbances due to extraneous large wavelength turbulent disturbances.
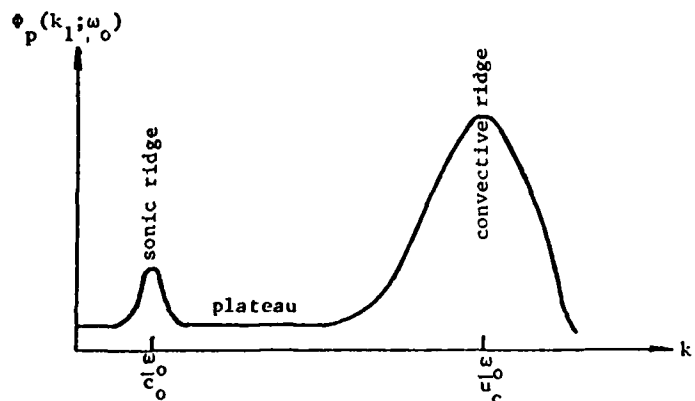
Fig. 5.   Speculated wall pressure spectral density $\Phi(k_1; \omega_o)$ showing the contributions due to the convective ridge and the radiated noise, Maidanik and Eisler ref. 10.

Measurements of $\phi_p(k_1; \omega)$ to date

Because of the problems at low wavenumbers referred to above, it seems that the spatial correlation measurement methods used by Hodgson [5] and also by Wills [11] were replaced in favor of a transducer array with signal processing so as to directly produce a wavenumber (or spatial) filter. Maidanik has described such filters which use relatively simple signal processing as "primitive" spatial filters. An array using four transducers in the longitudinal direction was described by Blake and Chase [4]. By alternating the phase of the transducer signals and summing, it is possible to produce a bandpass wavenumber filter which is enhanced further by purposely choosing the transducer response to behave as a low-pass wave-number filter.

More recent measurements by Farabee and Geib [12] using a six-transducer array in an anechoic wind-tunnel illustrate the method. Figures 6a, 6b show the measured wavenumber filter response functions for the common and alternating phased array (which incorporate the resolution characteristic of a single transducer). For the case quoted from reference 10 the alternating phased array behaves as a bandpass filter centered at $k_1\delta^* \approx 1.5$. Although $\phi_p(k_1; \omega_o)$ was not measured, the frequency spectrum at this particular value of $k_1\delta^*$ (i.e. a "slice" of the spectrum) was obtained which was felt to be 20 dB better in confidence than the Blake and Chase results, the latter possibly being contaminated by wind-tunnel noise

43
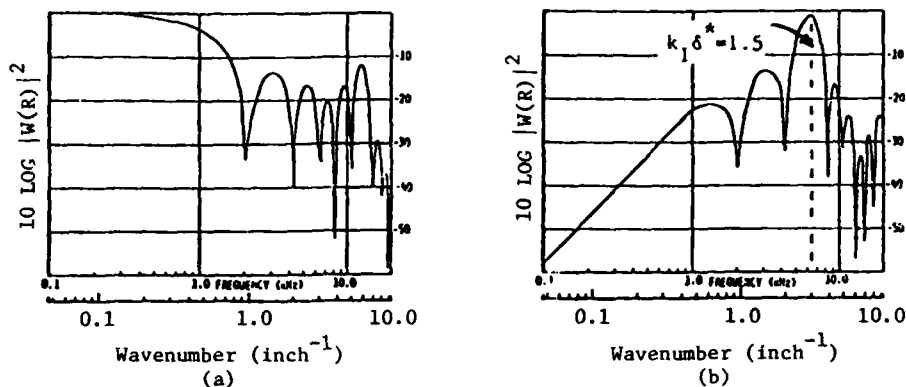
Fig. 6. Measured wavenumber response of (a) a six-element common-
phased array and (b) a six-element alternate-phased array,
Farabee and Geib ref. 12.

Maidanik and Eisler [10] have given an overview of these "primitive" wave-
number filters suggesting the use of irregular spacing, array steering, weight-
ing or shading of the transducer signals and single transducer shading. Mention
should also be made of other measurements using flexible plates or membranes as
wavenumber filters by Jameson and Martin and Leehey [13, 14] as well as analyti-
cal work by Aupperle and Lambert on wavenumber filter action by beams [15].

In summary, to date, no overall measurement of the $\phi_p(k_1; \omega)$ spectrum at low
wavenumbers relative to the convective ridge seems to have been confidently made
at this time. Figure 7, with axes $\omega^* = \omega\delta^*/U_c$ versus $k^* = k_1\delta^*$, is an informa-
tive plot in that it shows the areas of measurements made to date in the fre-
quency-wavenumber plane relative to the convective ridge and sonic line [16].
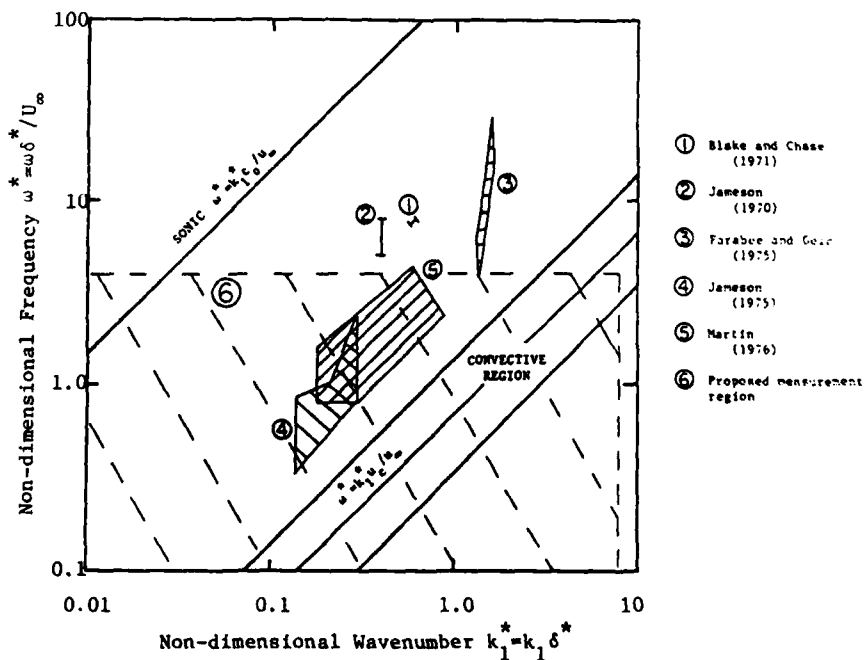
Fig. 7. The $(k_1^*; \omega^*)$ plane showing the regions of interest,
the regions of reported measurements and the pro-
posed measurement region.

3.   FFT ARRAY MEASUREMENT OF THE $\phi_p(\underset{\sim}{k}, \omega)$ SPECTRUM

As described earlier, the measurement of the low wavenumber region of the
TBL wall pressure spectrum may be characterized essentially as the measurement of
a relatively low amplitude signal in the presence of much higher amplitude signals.
That is, again examining Figure 5 for the spectrum $\phi_p(k_1; \omega_o)$ at given ω_o, the low-
wavenumber region is bounded at very low values by the sonic line and at the high
wavenumber extreme by the convective peak. Since the pattern is not truly frozen,
this convective peak has finite width and height, but is nevertheless of large
amplitude. The experimental solution to date has been to attempt to design a wave-
number filter that will admit data in the low wavenumber region and yet reject
both the sonic and convective components. Initial descriptions of this type of
array were first given by Maidanik and Jorgensen [17, 18, 19].

As mentioned previously, two types of arrays for which data have been pub-
lished are the common-phased array and the alternate-phased array. The responses
of such arrays for a flat transducer response are shown in Figures 8a and 8b
taken from reference 18. The first major peak of the common-phased array occurs
at $k_1 = 0$ while the first major peak of the alternate-phased array occurs at
$k_1 = N\pi/L$ where N is the number of transducers and L is the spatial extent of the
array. A key point in this approach is that the wavenumber response of the
pressure transducers is also used as a low-pass wavenumber filter in order to im-
prove the spatial filtering action and to further suppress the convective ridge.
This reduces all the response lobes except the first one, thus leaving it as the
dominant response lobe of the filter. For example, the array responses used by
Farabee and Geib [12] are shown in Figures 6a and 6b. Thus, the common-phased
array is a low-pass, spatial filter and the alternating-phased array is a band-
pass spatial filter. In both types, the highest side-lobe is only about 13 dB
down from the maximum response at the band-pass peak.

The technique proposed here is to also use an array of transducers, but with
a completely different signal processing methodology. Instead of electrically
summing the output of the transducers to form a single array output, the individ-
ual transducer outputs are kept distinct and used with a Fast Fourier Transform
(FFT) algorithm to produce a wavenumber spectrum. This method, which is outlined
below, is completely analogous to the transformation from the time domain to the
frequency domain by temporal sampling and the FFT algorithm as used in digital
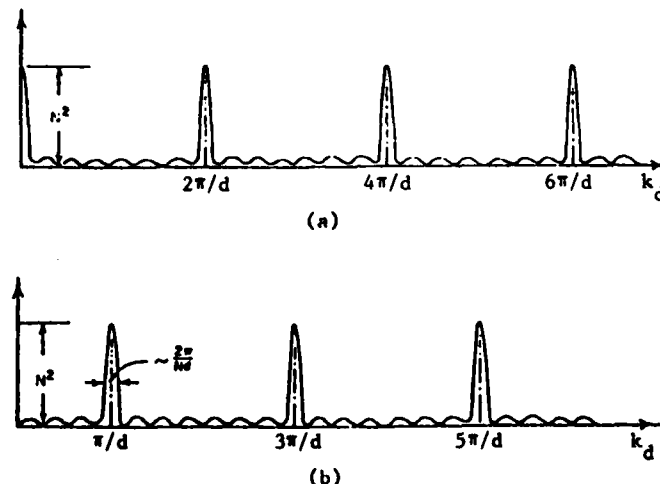frequency analyzers.

(a)

(b)

Fig. 8.   Wavenumber response of the N point-transducer
          equally-spaced wave-vector filter using (a)
          common-phased elements and (b) alternate-
          phased elements, Maidanik and Jorgensen ref. 10.

45

The two key advantages of the spatial FFT method that will be demonstrated below are:

1. the ability to measure different parts of the $k_1\delta*$ spectrum, including the convective part and the low wavenumber plateau simultaneously.

2. the ability to measure the low wavenumber portion while rejecting the convective ridge by at least 60 dB.

Theory

The theory underlying the spatial FFT method and implementation of the technique will now be discussed, see Bendat and Piersol [20] for a more detailed explanation.

Consider N transducers equally spaced at a distance h apart, aligned in the streamwise, x_1, direction. The outputs of these transducers, $p_n(x_n, t)$ represent the spatial sampling of the wall TBL pressure field $p(x_1, t)$ at the points $x_n = nh$, n = 0, 1, ..., N-1. Each of these signals may be frequency analyzed, either by analog or digital means, to yield the N outputs $p_n(x_n, \omega)$. These signals may then be used as inputs to an FFT algorithm to transform from the $(x_1; \omega)$ domain to the $(k_1; \omega)$ domain. As is well known from digital signal analysis, N data points in space (or time) will yield N/2 independent spectral lines in wavenumber (or frequency). These spectral lines occur at the wavenumbers:

$$k_m = m \frac{2\pi}{Nh} \quad ; \quad m = 0, 1, \ldots, \frac{N}{2} - 1 \qquad (2)$$

Thus, an immediate advantage of the spatial FFT over the summed array technique is that N/2 bands of information in wavenumber space are produced as compared to a single band in the summed array approach.

The highest wavenumber which is resolved is determined by the sensor spacing b according to the relation

$$k_{max} = \frac{\pi}{h} \qquad (3)$$

where k_{max} is the Nyquist or cut-off wavenumber. This constraint results from the familiar sampling theorem due to Shannon which states that at least two samples per wavelength (or period) are required to identify a sinusoid. The practical result is that components of the pressure field with wavenumbers greater than k_{max} cannot be resolved and fold-back or alias about k_{max}, resulting in a contamination of the computed spectral estimates in the range $0 \leq k \leq k_{max}$. One way to prevent this is to choose the spacing h small enough so that there is minimal data in the range $k > k_{max}$. Thus, spacing of the sensors is determined through estimates of the highest wavenumber component present.

The resolution or filter bandwidth of the N/2 spectral estimates is determined by the product of the sensor spacing and the number of sensors,

$$\Delta k = \frac{2\pi}{Nh} . \qquad (4)$$

Thus, for a given value of h, as the number of sensors increases, the number of spectral estimates also increase and the resolution bandwidth decreases. Of equal importance to the filter bandwidth is the filter roll-off characteristics of the FFT, and the control of this bandwidth is a major reason for the method chosen. In the present application it is desired to have minimal contributions from the convective peak in the spectral estimates of the low wavenumber region.

In FFT analysis, the filter roll-off is determined by the amplitude shading or "window function" applied to the N data points. For the case of uniform shading, the window function is rectangular, and the basic FFT filter response is

shown in Figure 9. The highest side-lobe level is -13 dB, with an asymptotic roll-off envelope of 6 dB/octave. Note that the side-lobe level is comparable to the summed array, but the roll-off characteristics are much more desirable.
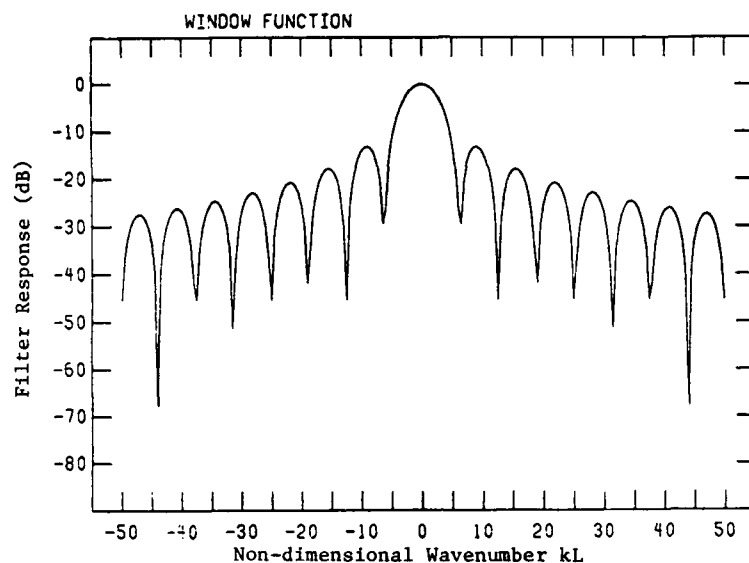
WINDOW FUNCTION

Fig. 9. The basic FFT filter shape for the uniform or rectangular window function.

Both the side-lobe level and the asymptotic roll-off may be adjusted by tapering each end of the data window. For example, the FFT filter response using the (cosine)^2 or "Hanning" window is shown in Figure 10. The highest side-lobe for this window is -32 dB with a roll off of 18 dB/octave, albeit at the expense of increasing the bandwidth of the main lobe. This window is one of the most frequently used in FFT frequency analyzers. It is the employment of this filter function shape that will allow the spatial FFT to be a useful tool in examining the low wavenumber region of the wall pressure spectrum.
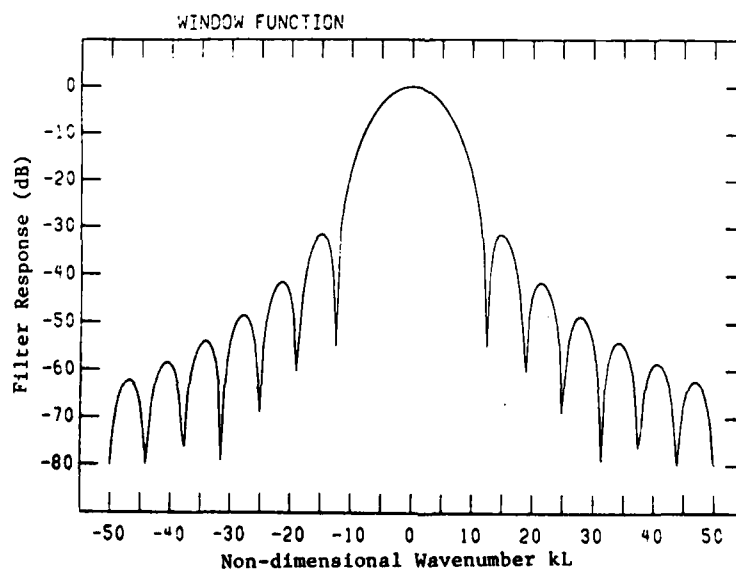
WINDOW FUNCTION

Fig. 10. The FFT filter shape for the (cosine)^2 or Hanning window function.

The primary parameters of importance in the array design are the sensor spacing h and the number of sensors N. The basic constraint in the present application is to fix the spacing h so that the convective wavenumber peak falls within the analysis range; that is, the Nyquist wavenumber must be greater than the convective wavenumber. If this occurs, then advantage may be taken of the dynamic range of the FFT to assure meaningful measurements at low wavenumber with negligible contribution from the convective peak. Using the non-dimensional parameters k_1^* and ω^* the convective peak is given by

$$(k_1^*)_c = (k_1\delta^*)_c = \omega^*\frac{U_\infty}{U_c} \qquad (5)$$

Imposing the restriction, say that the Nyquist wavenumber is equal to 1.5 times the convective wavenumber, the required sensor spacing is given by

$$h = \frac{\pi\delta^*U_c}{1.5\omega^*U_\infty} \qquad (6)$$

Assuming a typical value of $U_c/U_\infty = 0.8$, the required spacing h is shown in Table 1 for various values of δ^* and ω^*.

Table 1.

| $\delta^* = 0.1''$		$\delta^* = 0.25''$		$\delta^* = 0.5''$	
$\omega^* = 1$	$\omega^* = 10$	$\omega^* = 1$	$\omega^* = 10$	$\omega^* = 1$	$\omega^* = 10$
$h = .168''$	$h = .0168''$	$h = .419''$	$h = .0419''$	$h = .838''$	$h = .0838''$

Having determined the spacing based on the convective peak, the wavenumber resolution obtainable is strictly a function of N, the number of sensors. Thus the computed resolution is given by

$$\Delta k_1^* = \frac{3.75\omega^*}{N} . \qquad (7)$$

As an example, if $N = 50$, the resolution in terms of Δk_1^* is equal to 0.075 for $\omega^* = 1$ and is equal to 0.75 for $\omega^* = 10$.

Referring to Equation 6 and the example values of h presented in Table 1, it is clear that the maximum ω^* that may be investigated with this technique is determined by the transducer size. For example, assuming a representative value of $\delta^* = 0.2''$, the employment of innovative strain-gage pinhole transducers used by Hodgson and Brooks [21, 22] would permit measurements to be made in the range $\omega^* \leq 5$. This bound exists since the transducers' wavenumber responses have not been included in the above analysis, and the method described depends on the transducer spacing being small enough to ensure unambiguous measurements in the presence of the convective peak. Thus, the use of "large" transducers that attenuate the convective peak offers the potential of relaxing the constraint on the spacing, with the resulting increase in the range of ω^* that may be measured.

4. COMPARATIVE EXAMPLES

As an example of the characteristics of the spatial FFT process, consider the case of N = 50 transducers with a streamwise spacing given by Equation (6). From Equation (7), then, the spatial FFT will produce 25 lines in the k_1 spectrum at the values $k_1\delta*/\omega* = m(0.075)$, m = 0, 1, 2, ..., 24. The spatial filter response for the fifth spectral line, for example, is shown in Figure 11 as a function of the parameter $k_1\delta*/\omega*$. Note that the convective peak occurs at $k_1\delta*/\omega* = 1.25$ and the sonic line occurs at $k_1\delta*/\omega* = M_\infty$, the Mach number of the experiment. Considering a typical low speed test in air, the Mach number would fall in the range $0.05 < M_\infty < 0.1$. Thus, as shown in Figure 11, the measurement of the TBL wall pressure spectrum at $k_1\delta*/\omega* = 0.3$ would attenuate the convective peak by at least 70 dB, and the sonic line by approximately 40 dB.

Fig. 11. Typical spatial FFT filter response in the low-wavenumber region of the TBL wall pressure spectrum using the proposed measurement technique with N=50 transducers and the (cosine)^2 window function.

As mentioned previously, the side-lobe levels may be decreased further at the expense of increased main-lobe bandwidth. Figure 12, for example, shows the spatial filter response at $k_1\delta*/\omega* = 0.3$ using a (cosine)^4 window function instead of a (cosine)^2 window. The convective ridge is now attenuated by over 80 dB and the sonic line by about 50 dB. It should be noted that once the TBL pressure field has been sampled by the N transducers and recorded, multiple passes through the FFT algorithm may be made using any window function desired. Thus, the data may be analyzed repeatedly in order to obtain the maximum confidence in the spectral level measurements. Based on the design of sonar arrays, which are guided by introducing time delays between transducer signals, it might be expected that the above side-lobe rejections might not be achieved in practice due to transducer amplitude and phase errors, see for instance Quazi [23]. However, under laboratory conditions and using modern analog-digital techniques, it is standard practice to store the individual amplitude and phase calibrations of each transducer in digital memory and so avoid these errors. This is indeed so for the two-channel case which has made the two-microphone acoustic intensity meter a standard measurement instrument.
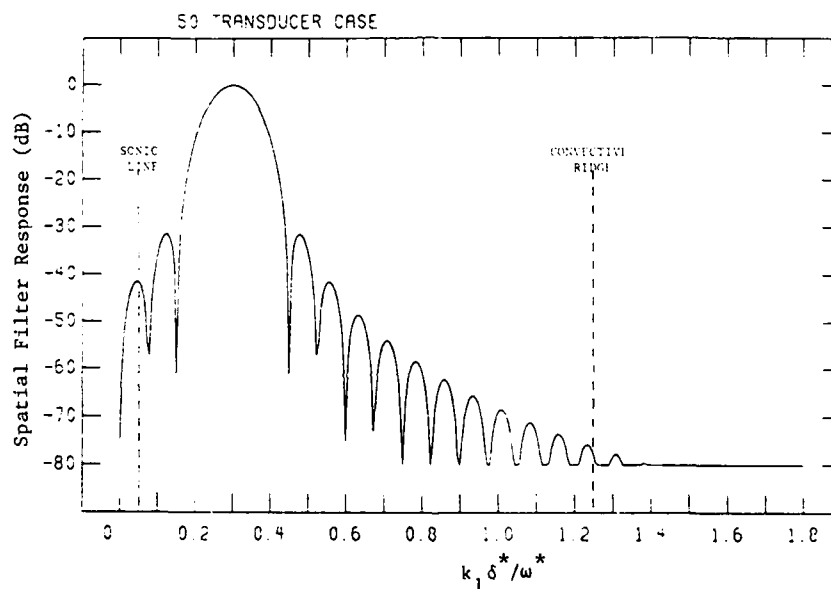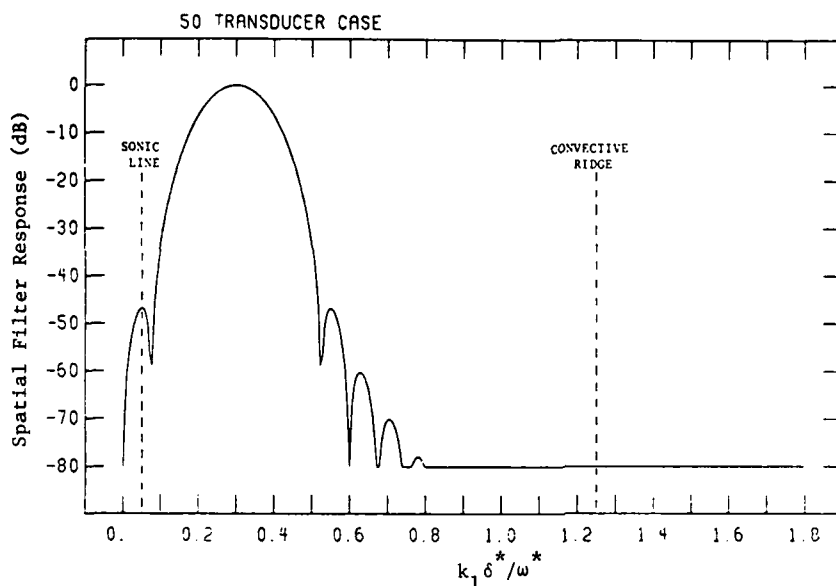
50 TRANSDUCER CASE

Fig. 12. Typical spatial FFT filter response in the low-wavenumber
region of the TBL wall pressure spectrum using the proposed
measurement technique with N=50 transducers and the $(cosine)^4$
window function.

Summarizing, as other workers using arrays have found, there must be a
compromise made between resolution of k* and ω*, see Figure 7. However, as shown
above, the FFT processed array has great advantage over previous methods. An
approximate estimate of the measurement region in the (k*; ω*) plane provided by
this approach is also plotted in Figure 7. In a practical case with the quoted
examples of δ* ≈ 0.2" and ω* ≈ 1 then capacitive transducers of 0.125" dia.
would suffice for the chosen spacing, while for values of ω* ≈ 5 then a smaller,
pinhole strain-gage transducer would be required because of the closer spacing
to achieve the wavenumber resolution. The method, with up to fifty transducers
in the array, is particularly suited to digital data acquisition which is in an
advanced state of development as a result of rapid development in micro-
circuitry.

REFERENCES

1. Townsend, A. A., Structure of Shear Flow Turbulence, Cambridge Univ. Press,
    1956.

2. Willmarth, W. W., "Pressure Fluctuations Beneath Turbulent Boundary Layers,"
    Annual Review of Fluid Mechanics, Vol. 7, 1975, pp. 13-37.

3. Hodgson, T. H., "Pressure Fluctuations in Shear Flow Turbulence," Ph.D.
    Thesis, University of London, 1962.

4. Blake, W. K. and Chase, D. M., "Wavenumber-Frequency Spectra of TBL Pressure
    Measured by Microphone Arrays," J. Acoust. Soc. Am., 49, Mar. 1971, pp. 862-
    877.

5. Hodgson, T. H., "On the Dipole Radiation from a Rigid and Plane Surface,"
    Proc. Purdue Noise Control Conf., July 1971, pp. 510-530.

6. Ffowcs Williams, J. E., "Surface-pressure Fluctuations Induced by Boundary-
    layer Flow at Finite Mach Number," J. Fluid Mech., 22, pt. 3, 1965, pp. 507-
    519.

7. Ffowcs Williams, J. E., "Boundary-layer Pressures and the Corcos Model: a Development to Incorporate Low-wavenumber Constraints," <u>J. Fluid Mech.</u>, 125, 1982, pp. 9-25.

8. Chase, D. M., "Modeling the Wavevector-Frequency Spectrum of Turbulent Boundary Layer Wall Pressure," <u>J. Sound Vib.</u> 70 (1), 1980, pp. 29-67.

9. Bergeron, R. F., "Aerodynamic Sound and the Low-wavenumber Wall Pressure Spectrum of Nearly Incompressible Boundary-layer Turbulence," <u>J. Acoust. Soc. Am.</u>, 54, Jan. 1973, pp. 123-133.

10. Maidanik, G. and Eisler, T., "Reasons and Means for Measuring the Spectral Density of the Pressure in a Subsonic TBL," <u>J. Sound Vib.</u>, 84(3), Oct. 1982, pp. 397-416.

11. Wills, J. A. B., "Measurements of the Wave-umber/Phase Velocity Spectrum of Wall Pressure beneath a TBL," <u>J. Fluid Mech.</u>, 45, pt 1, 1970, pp. 65-90.

12. Farabee, T. M. and Geib, F. E., "Measurement of Boundary Layer Pressure Fields with an Array of Pressure Transducers in a Subsonic Flow," International Congress on Instrumentation in Aerospace Simulation Facilities, 1975, pp. 311-319.

13. Jameson, P. W., "Measurement of the Low Wavenumber Component of TBL Spectral Density," Fourth Symposium on Turbulence in Liquids, Univ. of Missouri-Rolla, Sept. 1975, pp. 192-200.

14. Martin, N. C. and Leehey, P., "Low Wavenumber Wall Pressure Measurements Using a Rectangular Membrane as a Spatial Filter," <u>J. Sound Vib.</u>, 52(1), May 1977, pp. 95-120.

15. Aupperle, F. A. and Lambert, R. F., "Acoustic Radiation from Plates Excited by Flow Noise," J. Sound Vib., 26(2), 1973, pp. 223-245.

16. Geib, F. E., Private Communication.

17. Maidanik, G. and Jorgensen, D. W., "Boundary Wave-Vector Filters for the Study of the Pressure Field in a TBL," <u>J. Acoust. Soc. Am.</u> 42(2), 1967, pp. 494-501.

18. Maidanik, G., "Flush Mounted Pressure Transducer Systems as Spatial and Spectral Filters," <u>J. Acoust. Soc. Am.</u> 42(5), 1967, pp. 1017-1024.

19. Jorgensen, D. W. and Maidanik, G., "Response of a System of Point Transducers to TBL Pressure Field," <u>J. Acoust. Soc. Am.</u> 43(6), 1968, pp. 1390-1394.

20. Bendat, J. S. and Piersol, A. G., Random Data: <u>Analysis and Measurement Procedures</u>, John Wiley and Sons, Inc. 1971.

21. Brooks, T. F. and Hodgson, T. H., "Investigation of Trailing Edge Noise" IUTAM/ICA/AIAA Symposium, Mechanics of Sound Generation in Flows, Springer Verlag, 1979.

22. Brooks, T. F. and Hodgson, T. H., "Trailing Edge Noise Prediction from Measured Surface Pressures," <u>J. Sound Vib.</u> 78(1), 1981, pp. 69-117.

23. Quazi, A., "Array Beam Response on the Presence of Amplitude and Phase Fluctuations," <u>J. Acoust. Soc. Am.</u>, 72, July 1982, pp. 171-180.

USE OF RANDOM FORCES TO SIMULATE THE VIBROACOUSTIC RESPONSE OF A PLATE EXCITED BY A HYDRODYNAMIC TURBULENT BOUNDARY LAYER

G. Robert and J. Sabot

Laboratoire de Mecanique des Fluides et Acoustique
An Associated Laboratory of the Centre National
de la Recherche Scientifique
Ecole Centrale de Lyon
Ecully, France

ABSTRACT

A set of N random forces whose spatial location and spectral density are adjusted is proposed to simulate the wall pressure field beneath a hydrodynamic turbulent boundary layer.

The different steps of the present study are the following :

(i) Computation of the vibratory response of the plate (with simply supported edges) using the analytical formulation proposed by Corcos of the wall-pressure field cross-spectrum induced by a boundary layer. This computation is considered as a reference case later on.

(ii) Determination by an approximate numerical method, of the coordinates and the spectral density matrix of the N stationary random forces.

(iii) Comparison between the vibratory response calculated with the N random forces and the vibratory reference response.

For a hydrodynamic turbulent boundary layer in the 2 to 10 m/s velocity range, it is shown that the vibratory response of the plate is accurately reproduced by 5 random forces over a large frequency range.

NOMENCLATURE

a, b	Plate dimensions
g_i	Scalar associated to the ith force
$\overline{H}_{mn}(\omega)$	Modal frequency response function of the submerged plate
h	Plate thickness
$I_{mn}^{B.L.}(\omega)$	Boundary layer spectral density of generalized forces
$I_{mn}^{N}(\omega)$	Spectral density of generalized forces associated to the N forces.

N	Number of forces
p	Wall pressure
P	Number of simulated modes
U_∞	Flow velocity
$U_c(\omega)$	Convection velocity
$\ddot{w}$	Acceleration response
$\overline{W}_{mn}(\vec{r})$	Mode shape function of the submerged plate
$S_{FiFi}(\omega)$	Spectral density of the ith force
$S_{pp}(\omega)$	Spectral density of the wall pressure
$S_{\ddot{w}\ddot{w}}(\vec{r};\omega)$	Spectral density of the acceleration response of the point $\vec{r}$

1. INTRODUCTION

In many naval structures, the vibroacoustic response induced by boundary layers, wakes or jets, plays a vital role in limiting their ability to perform an assigned function. For example, sonar self-noise limits its ability to detect targets.

Because no appropriate anechoic water tunnel exists to experimentally study such underwater noise problems, the main objective of this paper is to provide the possibility of experimental investigations in a large water reservoir with no flow, rather than in an anechoic water tunnel.

The particular fluid/solid system considered here is a thin rectangular submerged plate excited on one side by a fully developed hydrodynamic turbulent boundary layer. A set of N random forces, whose spatial location and spectral density are adjusted, is proposed to simulate the wall pressure field beneath the boundary layer, as represented in Fig. 1.
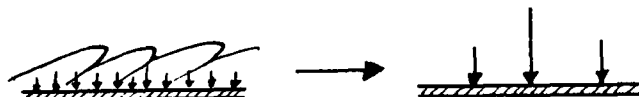
Fig. 1. Sketch of the proposed simulation.

2. EXCITATION-RESPONSE RELATIONS

If we assume the submerged plate to be a linear structure with time invariant deterministic properties, the cross-spectral density of its acceleration response $\ddot{w}(\vec{r};t)$ to a stationary random pressure $p(\vec{\rho};t)$ can be written [1]

$$S_{\ddot{w}\ddot{w}}(\vec{r}_1\vec{r}_2\omega) = \iint_{(ab)^2} \omega^4\, S_{pp}(\vec{\rho}_1\vec{\rho}_2\omega)\, \overline{H}^*(\vec{r}_1\vec{\rho}_1\omega)\, \overline{H}(\vec{r}_2\vec{\rho}_2\omega)\, d\vec{\rho}_1\, d\vec{\rho}_2 \quad (1)$$

where $\overline{H}(\vec{r},\vec{\rho};\omega)$ is the frequency influence function of the submerged plate and $S_{pp}(\vec{\rho}_1, \vec{\rho}_2; \omega)$ is the cross-spectral density of the pressure field. When

$S_{pp}(\vec{\rho}_1,\vec{\rho}_2;\omega)$ is known, it is necessary to compute $\overline{\overline{H}}(\vec{r},\vec{\rho};\omega)$ to obtain the response of the plate. This kind of computation is difficult because the fluid-solid interaction leads to an infinite system of coupled equations, i.e. to equations (2).

A simplified approach to this problem would be to neglect intermodal coupling and then to assume that the eigenfunctions $\overline{W}_{mn}(\vec{r})$ of the submerged plate are orthogonal. The response of the plate can be therefore written as follows :

$$S_{\scriptscriptstyle WW}(\vec{r}_1\vec{r}_2\,\omega) = \sum_{mn}\sum_{jk}\ \overline{W}_{mn}(\vec{r}_1)\ \overline{W}_{jk}(\vec{r}_2)\ \overline{H}^*_{mn}(\omega)\ \overline{H}_{jk}(\omega)\ \omega^4\ I_{mnjk}(\omega) \qquad (2)$$

where $I_{mnjk}(\omega)$ is the cross-spectral density between the generalized forces acting on the modes m,n and j,k. If we assume that the plate is lightly damped and that its natural frequencies are well separated, the cross terms in Eq. (2) can be neglected and we obtain :

$$S_{\scriptscriptstyle WW}(\vec{r}_1\vec{r}_2\,\omega) = \sum_{mn}\ \overline{W}_{mn}(\vec{r}_1)\ \overline{W}_{mn}(\vec{r}_2)\ \left|\overline{H}_{mn}(\omega)\right|^2\ \omega^4\ I_{mn}(\omega) \qquad (3)$$

2.1. Response of the plate to hydrodynamic turbulent boundary layer

In this case, the spectral density of the generalized force acting on mode m,n is :

$$I_{mn}^{B.L.}(\omega) = \iint_{(ab)^2}\ S_{pp}(\vec{\rho}_1\vec{\rho}_2\,\omega)\ \overline{W}_{mn}(\vec{\rho}_1)\ \overline{W}_{mn}(\vec{\rho}_2)\ d\vec{\rho}_1\,d\vec{\rho}_2 \qquad (4)$$

To calculate the spectral density $I_{mn}^{B.L.}(\omega)$ it is necessary to have a space-time description of the wall pressure beneath a turbulent boundary layer. The modelisation of such a convected random field raises theoretical and experimental difficulties, and only few attempts have been reported in the literature [2], [3], [4], [5]. In flow-induced vibration problems [6] many authors have used the analytical formulation of the wall pressure cross-spectrum suggested by Corcos [2]. For a simply supported or clamped rectangular plate, Corcos' formulation can be used to calculate the spectral density $I_{mn}^{B.L.}(\omega)$. The results of this calculation [7] show that $I_{mn}^{B.L.}(\omega)$ exhibits a peak value induced by a phenomenon of aerodynamic coincidence (wave matchings between the pressure wave and the flexural waves of the panel). This coincidence phenomenon does not influence the response of the structure above a critical frequency defined by the equality of the wall-pressure convection velocity and the flexural wave velocity. Below this critical frequency the response of the resonant modes of the structure can be enhanced by such a phenomenon.

In the present paper related to hydrodynamic problems, the flow velocity is usually small ($U_\infty \leqslant 15$ m/s), so that the hydrodynamic critical frequency is small and lower than the first resonant frequencies of the structure. In this situation one can use to calculate $I_{mn}^{B.L.}(\omega)$ the simplified formulation proposed by Davies [8].

$$I_{mn}^{B.L.}(\omega) \simeq S_{pp}(\omega)\ \omega^{-2}\ ab\ U_c^2(\omega)\ \alpha_1\alpha_2(1+\alpha_1^2)^{-1} \qquad (5)$$

where $S_{pp}(\omega)$ is the spectral density of the homogeneous turbulent wall pressure, a b the area of the plate, $U_c(\omega)$ a characteristic convection velocity, α_1 and α_2 the constants related to the spatial coherency of the pressure field. It is important to notice that from Eq. (5), the spectral density of the generalized force is the same for all the modes m,n.

Analytical formulations of $S_{pp}(\omega)$, $U_c(\omega)$, α_1 and α_2 have been proposed by Robert and Sabot [9]. These formulations will be used in the various computations presented in this paper.

2.2. Response of the plate to a set of N stationary random forces

If the N forces are not correlated, the spectral density $I_{mn}^N(\omega)$ of the generalized force acting on the mode m,n can be written :

$$I_{mn}^N(\omega) = \sum_{i=1}^N S_{F_i F_i}(\omega) \, \overline{W}_{mn}^2(\vec{\rho}_i)$$

(6)

where $S_{F_1 F_i}(\omega)$ is the spectral density of the force $F_i(i = 1 \text{ to } N)$ and $\vec{\rho}_i$ is the location of F_i on the plate.

The random response of the plate under the action of the N forces will be the same as that observed under the boundary layer if

$$I_{mn}^N(\omega) = I_{mn}^{BL}(\omega) \qquad\qquad \text{for all modes m,n} \qquad (7)$$

3. SIMULATION OF THE WALL PRESSURE FIELD BENEATH THE TURBULENT BOUNDARY LAYER

From Eq. (7), one can deduce that in order to replace the wall pressure field with a set of N random forces, one would have to solve an infinity of equations to find only 3N unknowns, (N spectral densities and 2N cartesian coordinates).

To overcome this difficulty,

i) we define a simulation which leads to a good representation of the vibratory response of only a finite number of successive modes (P modes).

ii) we introduce the following form for the spectral density of the punctual forces

$$S_{F_i F_i}(\omega) = g_i^2 \, S_{pp}(\omega) \, \omega^{-2}$$

(8)

where g_i is an unknown constant. This choice is suggested by Eq. (5) and by the purpose to define a simulation easy to use experimentally.

iii) we define a mean convection velocity among the P modes, as follows :

$$\tilde{U}_c = P^{-1} \sum_{J=1}^P U_c(\overline{\omega}_J)$$

(9)

where $\overline{\omega}_J$ is the natural pulsation of the Jth mode among the P modes.

Equations (5)-(9) lead therefore to the following approximate formulation for the simulation :

$$\left|\; \sum_{i=1}^N b_i^2 \, \overline{W}_J^2(\rho_i) = K \qquad J = 1 \text{ to } P \right. \tag{10a}$$

$$\left|\; g_i^2 = b_i^2 / K \; [ab\tilde{U}_c^2 \alpha_1 \alpha_2 / (1 + \alpha_1^2)] \right. \tag{10b}$$

where K and b_i are constants introduced for the numerical resolution. The simulation will be interesting if it leads tc a good reproduction of the vibratory response of a number P of the modes larger than the $3N$ unknowns ($2N$ cartesian coordinates for location of the N forces and N constants g_i). In such a perspective, only an approximate resolution of Eqs. (10a) is possible.

The resolution used in this paper is described as follows :

(a) in a first step, the plate surface is described by a finite number of points (nodes of a rectangular mesh) and the auxiliary constants, b_i, are selected from a finite number of fixed values.

(b) in a second step, only cne random force is considered ($N = 1$) and Eqs. (10a) are approximately solved by .ninimization of an appropriate cost function (least mean square method). Values of K are then calculated from Eqs. (10a) for each mode, and the amplification factors g_i are deduced from Eqs. (10b), where a mean value of K is introduced.

(c) in a third step, the response of the plate to the previous computed random force is compared to the response under the boundary layer.

(d) in a last step, the results obtained are improved by the successive addition of 1, 2, ... $N - 1$ forces and the corresponding computation of their locations and auxiliary constants b_i. Then, amplification factors g_i are estimated as above.

4. NUMERICAL RESULTS

The fluid/solid system considered in the present numerical study is defined as follows :

- the thin rectangular steel plate ($a = 0.3$ m ; $b = 0.16$ m ; $h = 0.001$ m) is assumed to be simply supported on its four edges

- the fully developed hydrodynamic turbulent boundary layer is characterized by its outer flow velocity $U_\infty = 8$ m/s and its displacement thickness $\delta^* = 1.92 \times 10^{-3}$ m.

In order to compare the P modes simulated response to their response to the turbulent wall pressure beneath the boundary layer, we have firstly computed the spectral density of the acceleration response of the plate induced by the turbulent flow. The result of this computation is shown in Fig. 2 (a) for a point located in the central region of the plate ($r_1/a = r_2/b = 0.47$).

4.1. Influence of the number of forces

The spectral densities of the acceleration response of the plate excited by 1, 3 or 5 random forces are shown in Figs. 2(b), 2(c) and 2(d) respectively. For these computations, we have chosen to reproduce the vibratory response of the twenty first modes ($P = 20$).

It can then be observed that for $N = 5$, we obtain a good simulation, since the difference between the response of the plate under the 5 forces and that under the boundary layer is always less than 1 dB.

4.2. Influence of the test-point location on the plate

In order to know if the previous results are valid for other points of the plate, we have computed the standard-deviation of the acceleration response for five new points on the plate ($r_1/a = r_2/b = 0.12$; 0.27 ; 0.47 ; 0.65 ; 0.82). The results obtained are shown in Fig. 3. It can be observed that the simulated response is still near the response under the boundary layer for each one of the selected points.
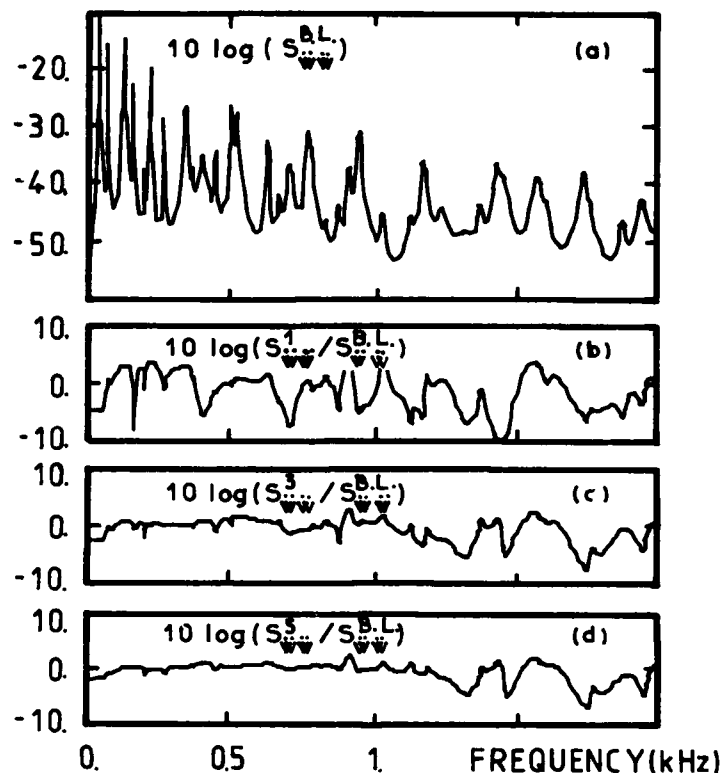
-20.
-30.
-40.
-50.

$10 \log (S_{ww}^{B.L.})$ (a)

10.
0.
-10.

$10 \log(S_{ww}^{1}/S_{ww}^{B.L.})$ (b)

10.
0.
-10.

$10 \log(S_{ww}^{3}/S_{ww}^{B.L.})$ (c)

10.
0.
-10.

$10 \log(S_{ww}^{5}/S_{ww}^{B.L.})$ (d)

0.   0.5   1.   FREQUENCY (kHz)

Fig.2. *Influence of the number of forces :*
a) spectral density of the acceleration response of the plate excited by a turbulent boundary layer (reference response) ; (b,c,d) comparison between simulated response and reference response (N = 1,3,5).
(Calculation conditions : P = 20, $r_1/a = r_2/b = 0.47$).

4.3. Influence of the flow velocity

It must be remembered that in the present method of simulation, the locations of the N random forces are not a function of the flow velocity. Only the amplification factor g_i applied to each one of the forces depends on the outer flow velocity U_∞. This interesting property is illustrated in Fig. 4 in which with the same location of the five random forces, we present the values of the standard-deviation of the acceleration response of the plate for five flow velocities. It can be observed that the simulation leads to very good results for all the velocities investigated.

4.4. Influence of the number of modes

The present method is based on the approximate resolution of P equations corresponding to the number P of modes for which we wish to obtain a restitution of the vibratory response. In order to obtain information about the influence of the parameter P on the simulated vibratory response, we have made computations for three values of P (P = 15, 20, 24). The corresponding results are presented in Fig. 5, which shows the difference between the simulated vibratory response and the vibratory response of the plate to the boundary layer. It can be observed that when P is increased, the quality of the simulation is also increased in a larger range of frequencies.

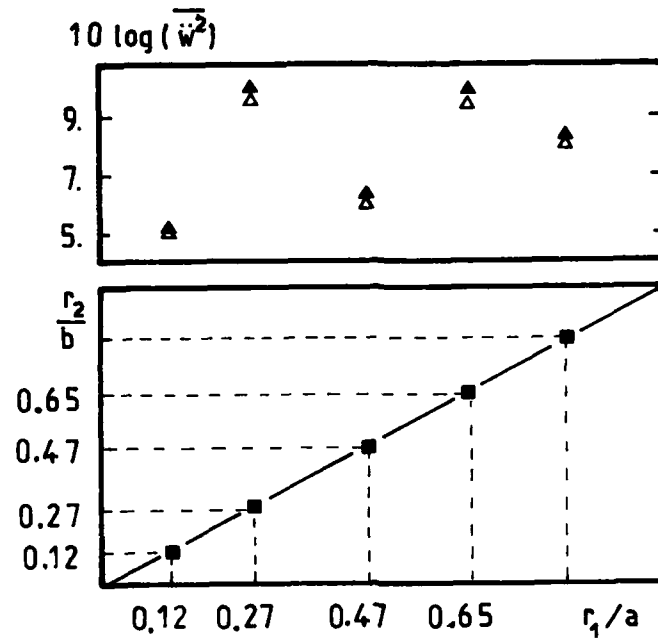*Fig. 3.* Comparison between simulated RMS response ▲ and reference response
△ for different locations on the plate.
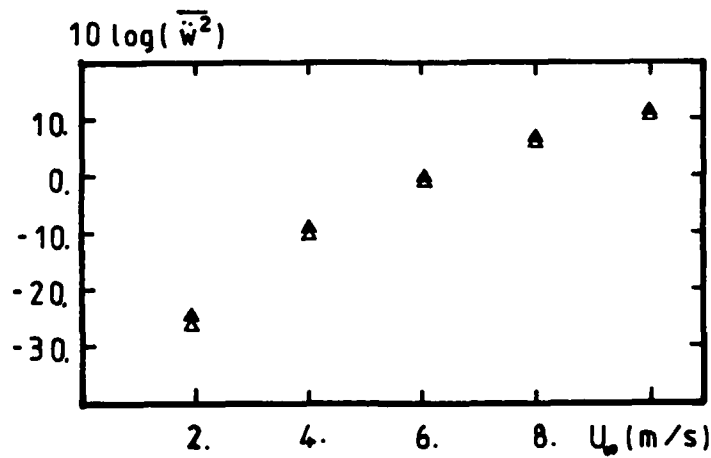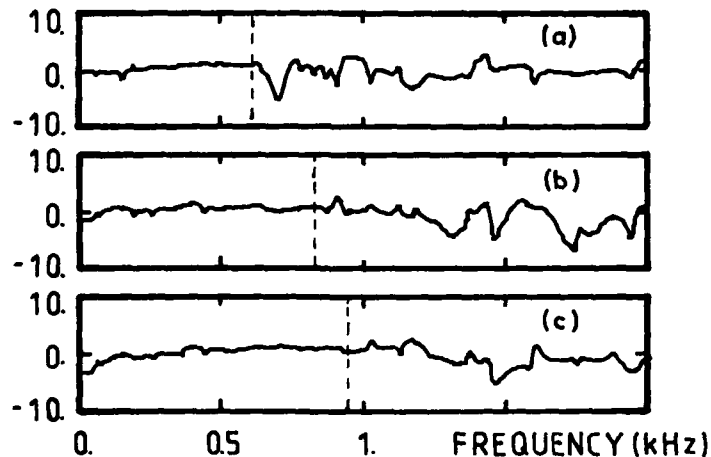(Calculation conditions : N = 5, P = 20).

Fig. 4. Influence of the flow velocity : ▲ simulated response ; △ reference
response.
(Calculation conditions : N = 5, P = 20, $r_1/a = r_2/b = 0.47$)

Fig. 5. Influence of the number of simulated modes :
Spectral density comparison between simulated response and reference
response (a) P = 15 ; (b) P = 20 ; (c) P = 24.
(Calculation conditions : N = 5, $r_1/a = r_2/b = 0.47$).

5. CONCLUSIONS

Numerical results obtained in this paper show that for a plate/hydrodynamic boundary layer fluid-solid system, it is possible to substitute for the turbulent wall pressure a limited number of random forces in order to obtain a good reproduction of the plate response over a large frequency range. For example with only five random forces, whose spatial location and spectral density are correctly adjusted, it is possible to reconstitute accurately the response of the first 24 modes.

The main advantage of the proposed method of simulation is that it is easy to perform experimentally. This is so because : (i) the location of the forces remains the same for all flow velocities investigated, and (ii) the spectral density of these forces can be readily obtained by an appropriate filtering of a white noise.

ACKNOWLEDGMENTS

REFERENCES

1. Lin, Y.K., "Probabilistic theory of structural dynamics", Mc Graw-Hill, 1967.

2. Corcos, G.M., "Resolution of pressure in turbulence", Journal of Acoustical Society of America, Vol. 35, N° 2, 1963, pp. 192-199.

3. Maestrello, L., "Use of turbulent model to calculate the vibration and radiation responses of panels with practical suggestions for reducing sound level", Journal of Sound and Vibration, Vol. 5, N° 3, 1967, pp. 407-448.

4. Chase, D.M., "Modeling the wave vector-frequency spectrum of turbulent boundary layer wall pressure", Journal of Sound and Vibration, Vol. 70, N° 3, 1980, pp. 29-67.

5. Ffowcs Williams, J.E., "Boundary-layer pressures and the Corcos model : a development to incorporate low-wave number constraints", Journal of Fluid Mechanics, Vol. 125, 1982, pp. 9-25.

6. Leibowitz, R.C., "Vibroacoustic response of turbulence excited thin rectangular finite plates in heavy and light fluid media", Journal of sound and Vibration, Vol. 40, n° 4, 1975, pp. 441-495.

7. Robert, G., "Modélisation et simulation du champ excitateur induit sur une structure par une couche limite turbulente", Thèse Ecole Centrale de Lyon, N° E.C.L. 84-02, 1984, France.

8. Davies, H.G., "Low frequency random excitation of water-loaded rectangular plates", Journal of Sound and Vibration, Vol. 15, N° 1, 1971, pp. 107-126.

9. Robert, G., Sabot J., "Rayonnement acoustique des structures excitées par une couche limite turbulente : influence de la modélisation du champ excitateur", Revue d'Acoustique, Vol. 67, 1983, pp. 272-279.

MEAN FLOW EFFECTS OF THE LOW-WAVENUMBER PRESSURE
SPECTRUM ON A FLEXIBLE SURFACE

A. P. Dowling
The University Engineering Department
Cambridge, United Kingdom

ABSTRACT

The Lighthill theory is extended so that it may be used to determine the flow noise induced by a turbulent boundary layer over a plane homogeneous flexible surface. The influence of the surface properties and the mean flow on the sound generation is brought out explicitly through the use of a Green function. The form of the low-wavenumber wall-pressure spectrum on a rigid surface with an arbitrary mean flow profile is determined. The effect of a coating layer is investigated.

1. INTRODUCTION

The sound generated by a turbulent boundary layer is influenced by surface flexibility and by the mean flow. We derive an expression for the low-wavenumber wall pressure spectrum in terms of a Green function and non-linear sources. The Green function brings out explicitly the influence of both the mean flow profile and surface flexibility. Chase and Noiseux [1] investigated the influence of a mean flow profile on the hard wall pressure spectrum. We extend that work to include surface compliance and investigate singularities in the surface pressure spectrum.

In underwater problems the Mach number of the mean flow is very small, and for low wavenumbers the flow only has an appreciable effect for spectral components whose surface phase speeds are nearly equal to the speed of sound. When the flow profile over a hard surface is neglected Ffowcs Williams [2] found that the pressure spectrum for these modes had a non-integrable singularity. Bergeron [3] analysed this singularity in more detail and showed that it arose from a two-dimensional form of Olbers' paradox because the turbulent source region is considered to be of infinite extent and the sound field from each source element

does not decrease rapidly enough for the integrated effect to be finite. In this paper we include the effect of an arbitrary mean boundary layer profile. It is found that this eliminates the singularity for all upstream propagating elements but enhances it for downstream propagating elements. For these downstream propagating components the singularity in the pressure spectrum is a double pole, and is stronger than the single pole found for uniform flow by Ffowcs Williams. This singularity is due to a 'trapped' mode, which propagates downstream supersonically in the boundary layer and subsonically in the flow outside it. The energy in this mode therefore remains trapped near the surface and only decays slowly with distance from the source. The influence of the boundary layer on these sonic elements is found to depend only on the free stream velocity and the displacement thickness of the boundary layer and to be independent of the details of the mean flow profile. Dowling [4] modelled the effect of the flow profile for long wavelength modes by a vortex sheet positioned at a height h above the surface. Consideration of an arbitrary mean flow profile shows that the vortex sheet result always describes the effect of a mean flow profile on the spectral elements with sonic phase speeds (the only elements much influenced by the mean flow), even when the boundary layer height is not small compared with the surface wavelength. This is because modes with sonic surface wave speeds have infinite wavelengths normal to the surface. In particular, by solving the problem for an arbitrary mean flow profile, we find where the equivalent vortex sheet should be positioned; at a height h above the surface equal to the boundary layer displacement thickness.

The influence of a coating layer over a hard surface is investigated. It is found that if the sound speed in the coating is greater than that in the fluid it is possible for the coating to eliminate the singularity for downstream propagating modes. A coating with a low sound speed has an adverse effect on the surface pressure and can even introduce new singularities into the wall pressure spectrum.

2. THE SURFACE PRESSURE ON A FLEXIBLE WALL

Consider a turbulent boundary layer flow over a plane, homogeneous, flexible wall. In our problem the flexible wall is assumed to be only linearly disturbed from its rest position $y_3 = 0$, and the mean flow $U(y_3)$ is assumed to be a function of y_3 only, as shown in Figure 1. Far from the surface $U(y_3)$ tends to the free-stream velocity U_1 and $U(0) = 0$. The impedance is uniform over the whole surface and the relationship between surface pressure perturbation p' and displacement ξ can be conveniently expressed in terms of their Fourier transforms:

$$\bar{p}(0,\underline{k},\omega) = Z(\underline{k},\omega)\bar{\xi}(\underline{k},\omega) \tag{1}$$

where $\bar{p}(y_3,\underline{k},\omega) = \int p'(\underline{y},\tau)e^{-i(\omega t+k_1 y_1+k_2 y_2)}dy_1 dy_2 dt$.
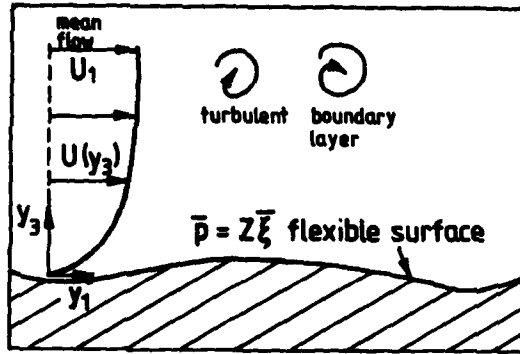
<u>Figure 1</u> The geometry of the flexible surface and turbulent boundary layer

We write the instantaneous particle velocity as $\{U(y_3),0,0\} + \underline{u}'$. Then by differentiating the equation of mass conservation with respect to time and subtracting from it the divergence of the momentum equation we obtain:

$$\frac{\partial^2 \rho}{\partial \tau^2} - U^2 \frac{\partial^2 \rho}{\partial y_1^2} - 2U \frac{\partial^2(\rho u_i')}{\partial y_1 \partial y_i} - 2 \frac{dU}{dy_3} \frac{\partial}{\partial y_1}(\rho u_3') - c_1^2 \nabla^2 \rho = \frac{\partial^2 T_{ij}}{\partial y_i \partial y_j} \qquad (2)$$

$T_{ij} = \rho u_i' u_j' + (p' - c_1^2 \rho')\delta_{ij} - \sigma_{ij}$, σ_{ij} is the viscous stress tensor and c_1 is the unperturbed value of the sound speed in the fluid. Finally the mass equation and 3-component of momentum equation can be used to eliminate $\text{div}(\rho\underline{u}')$ and $\partial(\rho u_3')/\partial y_1$ respectively to show that:

$$\frac{1}{c_1^2}\left(\frac{\partial}{\partial \tau} + U\frac{\partial}{\partial y_1}\right)^3 \rho + 2\frac{dU}{dy_3}\frac{\partial^2 \rho}{\partial y_1 \partial y_3} - \left(\frac{\partial}{\partial \tau} + U\frac{\partial}{\partial y_1}\right)\nabla^2 \rho$$

$$= \frac{1}{c_1^2}\left\{\left(\frac{\partial}{\partial \tau} + U\frac{\partial}{\partial y_1}\right)\frac{\partial^2 T_{ij}}{\partial y_i \partial y_j} - 2\frac{dU}{dy_3}\frac{\partial^2 T_{3j}}{\partial y_1 \partial y_j}\right\} \qquad (3)$$

We solve this by introducing $\bar\rho(y_3,\underline{k},\omega)$ and $\bar T_{ij}$ the Fourier transforms of the density perturbation and T_{ij} respectively. For convenience we take $\bar\rho + \bar T_{33}/c_1^2$ as our variable. The equation for $\bar\rho + \bar T_{33}/c_1^2$ can be written in self-adjoint form as:

$$\frac{\partial^2}{\partial y_3^2}\left(\frac{\bar\rho + \bar T_{33}/c_1^2}{\omega + Uk_1}\right) + f\frac{\bar\rho + \bar T_{33}/c_1^2}{\omega + Uk_1} = \frac{1}{c_1^2}\left\{\frac{k_\alpha k_\beta \bar T_{\alpha\beta} + \gamma^2 \bar T_{33}}{\omega + Uk_1} - 2ik_\alpha \frac{\partial}{\partial y_3}\left(\frac{\bar T_{\alpha 3}}{\omega + Uk_1}\right)\right\} \qquad (4)$$

where α and β are summed over 1 and 2,

$$f(y_3,\underline{k},\omega) = \frac{(\omega + Uk_1)^2}{c_1^2} - k_1^2 - k_2^2 + \frac{d^2 U}{dy_3^2}\frac{k_1}{\omega + Uk_1} - 2\left(\frac{dU}{dy_3}\right)^2\frac{k_1^2}{(\omega + Uk_1)^2}$$

and $\gamma = \{(\omega + Uk_1)^2/c_1^2 - k_1^2 - k_2^2\}^{\frac{1}{2}}$ with the sign of the square root chosen so that γ has the same sign as ω when γ is real and $\text{Im}\gamma$ is negative when γ is purely imaginary.

Outside the boundary layer the flow is only linearly disturbed from the free stream velocity $\{U_1,0,0\}$ and $\bar T_{ij} = 0$. Since the disturbances must either decay at large y_3 or be outward propagating sound waves,

$$\frac{\partial \bar\rho}{\partial y_3} = -i\gamma_1 \bar\rho \quad \text{for large positive } y_3 \qquad (5)$$

66

$\gamma_1, = \{(\omega+U_1 k_1)^2/c_1^2 - k_1^2 - k_1^2\}^{\frac{1}{2}}$, is the limit of γ as y_3 tends to infinity. Very near the surface $y_3 = 0$ the flow is only linearly disturbed and $p' = c_1^2 \rho'$. The linearised 3-component of the momentum equation and the surface condition (1) then give:

$$\rho_1 \omega^2 \bar{\rho} = Z \partial \bar{\rho}/\partial y_3 \tag{6}$$

since $U(0)$ is zero. ρ_1 is the mean value of density in the fluid.

We solve for $\bar{\rho}$ in equation (4) by introducing a Green function $G(y_3, x_3, \underline{k}, \omega)$ which satisfies:

$$\frac{\partial^2 G}{\partial y_3^2} + fG = \delta(y_3 - x_3) \tag{7}$$

Multiplying equation (7) by $(\bar{\rho} + \bar{T}_{33}/c_1^2)/(\omega + Uk_1)$ and subtracting from it the product of G and equation (4) we obtain:

$$\frac{\bar{\rho} + \bar{T}_{33}/c_1^2}{\omega + Uk_1} (x_3, \underline{k}, \omega) = \frac{1}{c_1^2} \int \left\{ G \frac{k_\alpha k_\beta \bar{T}_{\alpha\beta} + \gamma^2 \bar{T}_{33}}{\omega + Uk_1} + \frac{2ik_\alpha}{\omega + Uk_1} \frac{\partial G}{\partial y_3} \bar{T}_{\alpha 3} \right\} dy_3$$
$$+ \left[\frac{\bar{\rho} + \bar{T}_{33}/c_1^2}{\omega + Uk_1} \frac{\partial G}{\partial y_3} - G \frac{\partial}{\partial y_3} \left(\frac{\bar{\rho} + \bar{T}_{33}/c_1^2}{\omega + Uk_1} \right) \right]_0^\infty \tag{8}$$

The term at $y_3 = \infty$ is zero if we choose a Green function G such that,

$$\partial G/\partial y_3 \rightarrow -i\gamma_1 G \qquad \text{as } y_3 \rightarrow \infty \tag{9}$$

Similarly insisting that G satisfies the surface boundary condition:

$$\frac{\partial G}{\partial y_3} = G \left\{ -\frac{U'(0)k_1}{\omega} + \frac{\rho_1 \omega^2}{Z} \right\} \qquad \text{on } y_3 = 0 \tag{10}$$

$(U'(0) = dU/dy_3$ evaluated at $y_3 = 0)$ eliminates the contribution to (8) from $y_3 = 0$. These two boundary conditions together with equation (7) completely determine the Green function.

With this particular Green function, equation (8) gives the Fourier transform of the surface pressure perturbation as:

$$\bar{p}(0, \underline{k}, \omega) = \omega \int \left\{ G \frac{k_\alpha k_\beta \bar{T}_{\alpha\beta} + \gamma^2 \bar{T}_{33}}{\omega + Uk_1} + \frac{2ik_\alpha}{\omega + Uk_1} \frac{\partial G}{\partial y_3} \bar{T}_{\alpha 3} \right\} dy_3 \tag{11}$$

We now have the surface pressure given explicitly in terms of a Green function and nonlinear sources. It remains to calculate the Green function which we do by the method used by Chase and Noiseux [1].

3. CALCULATION OF THE GREEN FUNCTION

$G(y_3, x_3, \underline{k}, \omega)$ can be expressed in terms of two solutions $E(y_3)$ and $F(y_3)$ of the homogeneous equation:

$$\frac{\partial^2 E}{\partial y_3^2} + fE = 0 \tag{12}$$

where E satisfies the boundary condition at infinity (9),

$$\frac{\partial E}{\partial y_3} = -i\gamma_1 E \qquad \text{for large } y_3 \tag{13}$$

and F the surface boundary condition (10):

$$\frac{\partial F}{\partial y_3} = F\left\{-\frac{U'(0)k_1}{\omega} + \frac{\rho_1\omega^2}{Z}\right\} \quad \text{on } y_3 = 0 .\tag{14}$$

Since E and F are only defined to within an arbitrary constant we will choose,

$$E(0) = F(0) = 1\tag{15}$$

Then $G(y_3,x_3,\underline{k},\omega)$ is given by (see for example Morse and Feshbach [5]):

$$G(y_3,x_3,\underline{k},\omega) = \begin{cases} F(x_3)\ E(y_3)/W & y_3 \geq x_3 \\[2mm] E(x_3)\ F(y_3)/W & y_3 \leq x_3 \end{cases}\tag{16}$$

where W is the Wronskian, $F\ \partial E/\partial y_3 - E\ \partial F/\partial y_3$, and is independent of y_3. We will therefore evaluate W on $y_3 = 0$, where the boundary conditions (14) and (15) show that:

$$W = E'(0) + U'(0)k_1/\omega - \rho_1\omega^2/Z\tag{17}$$

$E'(0)$ denotes the value of the derivative $\partial E/\partial y_3$ at $y_3 = 0$. Substitution for W in (16) shows in particular that

$$G(y_3,0,\underline{k},\omega) = \frac{E(y_3)}{E'(0)+U'(0)k_1/\omega-\rho_1\omega^2/Z}\tag{18}$$

and the representation (11) becomes:

$$\bar{p}(0,\underline{k},\omega) = \frac{\omega}{E'(0)+U'(0)k_1/\omega-\rho_1\omega^2/Z}\int\left\{E(y_3)\frac{k_\alpha k_\beta \bar{T}_{\alpha\beta}+\gamma^2\bar{T}_{33}}{\omega+Uk_1} + \frac{\partial E}{\partial y_3}\frac{2ik_\alpha \bar{T}_{\alpha3}}{\omega+Uk_1}\right\}dy_3\tag{19}$$

This is equivalent to Chase and Noiseux's equation (28) (see reference [1]), extended to take into account surface flexibility. It is in a particularly convenient form because the influence of surface flexibility is displayed explicitly in the term $Z.E(y_3)$, the solution to equation (12) with boundary conditions (13) and (15), depends only on the mean flow profile and not in any way on the surface properties. The effect of a change in surface properties can be investigated by considering the function $[E'(0)+U'(0)k_1/\omega-\rho_1\omega^2/Z]^{-1}$ for different surface impedances. It remains for us to calculate $E(y_3)$.

E satisfies a linear second order differential equation (12) with the boundary conditions (13) and (15). This can easily be solved numerically for a particular mean flow profile. The results in Section 4 were obtained for a tanh-velocity profile $U(y_3) = U_1\tanh(y_3/\delta)$, where δ is a measure of the boundary layer height. To aid numerical integration the problem for $E(y_3)$ was cast into the form of a non-linear first order differential equation for $\phi(y_3)$. This technique was used by Michalke [6] when investigating flow stability. $\phi(y_3)$ is defined by:

$$E(y_3) = \exp\left[\int_0^{y_3} \phi(y_3')\ dy_3'\right]\tag{20}$$

Then $\phi, = \frac{1}{E}\frac{dE}{dy_3}$, satisfies

$$\frac{d\phi}{dy_3} = -\phi^2 - f\tag{21}$$

with boundary condition $\phi(\infty) = -i\gamma_1$. Rather than integrate over an infinite

range the spatial variable was changed to $z = \tanh(y_3/\delta)$. Then the resulting equation was integrated from $z = 1$, where ϕ is $-i\gamma_1$, to $z = 0$, using a Runge-Kutta-Merson method, thus determining $\phi(0) = E'(0)$ as required in (19). These values of $E'(0,\underline{k},\omega)$ are used in Section 4.

In fact the dominant flow effect does not depend on the details of the boundary layer profile. In order to see that and to interpret the results in Section 4 we will derive an asymptotic form for $E(y_3)$ valid for low values of the flow Mach number $M = U_1/c_1$. In underwater applications M is of the order of 0.01 and this limit is justified. We write $\eta = y_3/\delta$, $U(y_3) = U_1 V(\eta)$, $s_1 = k_1 c_1/\omega$ and $s_2 = k_2 c_1/\omega$. For sonic and supersonic phase elements $(s_1^2 + s_2^2)^{\frac{1}{2}}$ takes values of order unity. δ is of the order of the boundary layer height. We will not assume that $\omega\delta/c_1$ is small as in Chase and Noiseux's detailed calculations [1]. For a boundary layer of height 5 cm in water and a frequency of 5 kHz, $\omega\delta/c_1$ is about unity. When cast in terms of non-dimensional variables the problem for E is:

$$\frac{d^2E}{d\eta^2} + \delta^2\gamma_1^2 E = E\left[\left(\frac{\omega\delta}{c_1}\right)^2\left\{2Ms_1(1-V) + M^2s_1^2(1-V^2)\right\}\right.$$
$$\left. + \frac{2M^2s_1^2}{(1+MVs_1)^2}\left(\frac{dV}{d\eta}\right)^2 - \frac{Ms_1}{1+MVs_1}\frac{d^2V}{d\eta^2}\right] \tag{22}$$

We seek a solution for E as a power series in the Mach number M;
$E(\eta) = E_0(\eta) + ME_1(\eta) + \ldots$. Then

$$\frac{d^2E_0}{d\eta^2} + (\delta\gamma_1)^2 E_0 = 0 \tag{23a}$$

$$\frac{d^2E_1}{d\eta^2} + (\delta\gamma_1)^2 E_1 = \left[\left(\frac{\omega\delta}{c_1}\right)^2 2(1-V) - \frac{d^2V}{d\eta^2}\right] s_1 E_0 \quad . \tag{23b}$$

The solution for E_0, satisfying the boundary condition at infinity, is:

$$E_0(\eta) = Ae^{-i\delta\gamma_1\eta} \, , \quad \text{where A is a constant.} \tag{24}$$

$E_1(\eta)$ is then the solution of an inhomogeneous second order differential equation with constant coefficients and can be found in a straightforward way to give:

$$E_1(\eta) = As_1 e^{i\delta\gamma_1\eta} \int_\eta^\infty \left\{\frac{dV}{dS} + 2\left(\frac{\omega\delta}{c_1}\right)^2 X(S)\right\} e^{-2i\delta\gamma_1 S}\, dS \tag{25}$$

where $X(\eta) = \int_\eta^\infty (1-V(S))dS$.

A can be calculated from the boundary condition (15), $E(0) = 1$, and then $E(\eta)$ is determined to order M. In particular this gives:

$$\frac{dE}{d\eta}(0) = -i\delta\gamma_1(1+MB) - s_1 M\left\{\frac{dV}{d\eta}(0) + 2\left(\frac{\omega\delta}{c_1}\right)^2 X(0)\right\} \tag{26}$$

where $B = -2s_1 \int_0^\infty \left\{\frac{dV}{dS} + 2\left(\frac{\omega\delta}{c_1}\right)^2 X(S)\right\} e^{-2i\delta\gamma_1 S}\, dS$.

Returning to dimensional variables we have:

$$\frac{dE}{dy_3}(0) \;=\; -i\gamma_1(1+MB) - U'(0)\frac{k_1}{\omega} - 2k_1\omega M \frac{\delta_1}{c_1} \tag{27}$$

correct to order M. δ_1 is the boundary layer displacement thickness defined by $\delta_1 = \int_0^\infty (1-U(y_3)/U_1)dy_3$. We have retained the order M terms in this expression because it is possible for the leading term, $-i\gamma_1$, to vanish.

To lowest order in M, $E(y_3) = e^{-i\gamma_1 y_3}$ and the representation (19) gives:

$$\bar{p}(0,\underline{k},\omega) \;=\; \frac{D_i D_j}{E'(0)+U'(0)k_1/\omega-\rho_1\omega^2/Z} \int e^{-i\gamma_1 y_3}\, \bar{T}_{ij}(y_3,\underline{k},\omega)\, dy_3 \tag{28}$$

for modes with sonic and supersonic phase speeds. $D_\alpha = k_\alpha$ for $\alpha = 1,2$ and $D_3 = \gamma_1$. The terms in the numerator cannot all vanish simultaneously and so we have only kept the lowest order terms there. But in the denominator the leading order term can vanish and so terms of order M must be retained.

The wall pressure spectrum can be derived from the Fourier transform of the surface pressure in the usual way (see, for example, Dowling [4] for the details) and is given by:

$$P(\underline{k},\omega) \;=\; \frac{D_i^\dagger D_j^\dagger D_k D_\ell}{\left| E'(0)+U'(0)k_1/\omega-\rho_1\omega^2/Z \right|^2} \int e^{i\gamma_1^\dagger y_3 - i\gamma_1 y_3'}\, T_{ijk\ell}(y_3,y_3',\underline{k},\omega)\,dy_3 dy_3' \tag{29}$$

where the dagger denotes the complex conjugate and $T_{ijk\ell}$ is the cross-correlation of the turbulent sources:

$$T_{ijk\ell}(y_3,y_3',\underline{k},\omega) = \int \overline{T_{ij}(\underline{y},\tau)T_{k\ell}(y_1+\Delta_1,y_2+\Delta_2,y_3',\tau+\tau_0)}\; e^{-ik_\alpha\Delta_\alpha - i\omega\tau_0}d^2\underline{\Delta}d\tau_0 \tag{30}$$

If the acoustic analogy has been successful in extracting the essential field structure $T_{ijk\ell}$ should be independent of compressibility effects. $T_{ijk\ell}$ can therefore be estimated on the basis of incompressible flow theory. We will non-dimensionalize the integral in (29) and write:

$$\int e^{i\gamma_1^\dagger y_3 - i\gamma_1 y_3'}\, T_{ijk\ell}(y_3,y_3',\underline{k},\omega)dy_3 dy_3' = \rho_1^2 U_1^3 \delta_1^5 Q_{ijk\ell}(\delta_1\underline{k},\delta_1\omega/U_1) \tag{31}$$

Then the pressure spectrum simplifies to:

$$P(\underline{k},\omega) \;=\; \frac{D_i^\dagger D_j^\dagger D_k D_\ell}{\left| E'(0)+U'(0)k_1/\omega-\rho_1\omega^2/Z \right|^2}\, \rho_1^2 U_1^3 \delta_1^5 Q_{ijk\ell}(\delta_1\underline{k},\delta_1\omega/U_1) \tag{32}$$

$D_i^\dagger D_j^\dagger D_k D_\ell |E'(0)+U'(0)k_1/\omega-\rho_1\omega^2/Z|^{-2}$ describes how the turbulent field $Q_{ijk\ell}$ radiates sound within the boundary layer over the flexible surface. The product $D_i^\dagger D_j^\dagger D_k D_\ell$ describes the propagation of the different directional elements, but the main structure of the surface pressure spectrum comes from the $|E'(0)+U'(0)k_1/\omega-\rho_1\omega^2/Z|^{-2}$ term.

In the low Mach number limit, equation (27) shows that:

$$E'(0) + U'(0)k_1/\omega-\rho_1\omega^2/Z \;=\; -i\gamma_1(1+MB) - 2\omega k_1\delta_1 M/c_1 - \rho_1\omega^2/Z \;. \tag{33}$$

Without a mean flow profile and a flexible surface, $E'(0)+U'(0)k_1/\omega-\rho_1\omega^2/Z = -i\gamma_1$, which vanishes for spectral elements with sonic phase speeds. The mean flow profile therefore has most effect on the pressure spectrum near $\gamma_1 = 0$ where the leading order term in (33) vanishes. Then the $-i\gamma_1 MB$ term is negligible since

both γ_1 and M are small and the dominant effect of the mean flow profile is contained in the term $-2\omega k_1 \delta_1 M/c_1$. This was verified by numerical calculations for a tanh-velocity profile $U_1 \tanh(y_3/\delta)$. Integration shows that for such a mean flow velocity variation the displacement thickness δ_1 is equal to $\delta \log_e 2$. The values of $E'(0)+U'(0)k_1/\omega$ calculated numerically were compared with $-i\gamma_1-2\omega k_1\delta_1 M/c_1$ for a Mach number of 0.01, $\omega\delta/c_1 = 1$, and good agreement was obtained for a range of values of $k_1 c_1/\omega$.

The major effect, therefore, of the boundary-layer profile is independent of the details of the boundary layer depending only on its integrated effect through the displacement thickness δ_1 ($= \int_0^\infty (1-U/U_1)dy_3$). We now see that the vortex sheet analogy developed by Dowling [4] is able to describe the effect of a mean flow profile on sonic or supersonic spectral elements for all boundary layers, not just for boundary layers which are thin in comparison with the wavelength, $2\pi c_1/\omega$, as suggested in that paper. We can understand this physically because the main influence of the flow profile is on spectral elements with nearly sonic phase speeds for which $\gamma_1 \simeq 0$, and these modes have infinitely long wavelengths in a direction normal to the surface. In particular by including an arbitrary mean flow profile and making no further approximations other than assuming the Mach number to be small, we have found where the equivalent vortex sheet should be placed. It is at a height above the surface equal to the displacement thickness of the boundary layer.

4. THE WALL-PRESSURE SPECTRUM ON VARIOUS SURFACES

Equation (32) describes the influence of the surface structure and mean flow profile on the wall-pressure spectrum. In this section the form of the pressure spectrum is investigated for a couple of simple surfaces.

4.1 A Hard Surface

The normal displacement always vanishes on a hard surface and so Z is infinite. From (32) the surface pressure spectrum is given by:

$$P(\underline{k},\omega) = \frac{D_i^\dagger D_j^\dagger D_k D_\ell}{\left|E'(0)+U'(0)k_1/\omega\right|^2} \rho_1^2 U_1^3 \delta_1^5 Q_{ijk\ell}(\delta_1\underline{k},\delta_1\omega/U_1) \tag{34}$$

$\left|E'(0)+U'(0)k_1/\omega\right|^{-2}$ is plotted as a function of $k_1 c_1/\omega$ in Figure 2 for a flow with a velocity profile $U(y_3) = U_1\tanh(y_3/\delta)$ and $M = 0.01$, $\omega\delta/c_1 = 1$. In order to interpret these results we will consider the low Mach number limit.

Equation (33) gives:

$$E'(0) + U'(0)k_1/\omega = -i\gamma_1(1+MB) - 2\omega k_1\delta_1 M/c_1 \tag{35}$$

correct to order M. The denominator in (34) is therefore small near $\gamma_1 \simeq 0$, but it can only vanish when γ_1 is purely imaginary. Then the first term on the right-hand side of (35) is real and negative, and so from (35) $E'(0)+U'(0)k_1/\omega$ only vanishes if ω and k_1 have opposite signs, i.e. for downstream propagating modes. For upstream propagating modes $E'(0)+U'(0)k_1/\omega$ is always non-zero. The

pressure spectrum therefore has a double pole near $\gamma_1 = 0$ for downstream propagating spectral components, but it is always finite for upstream propagating elements.
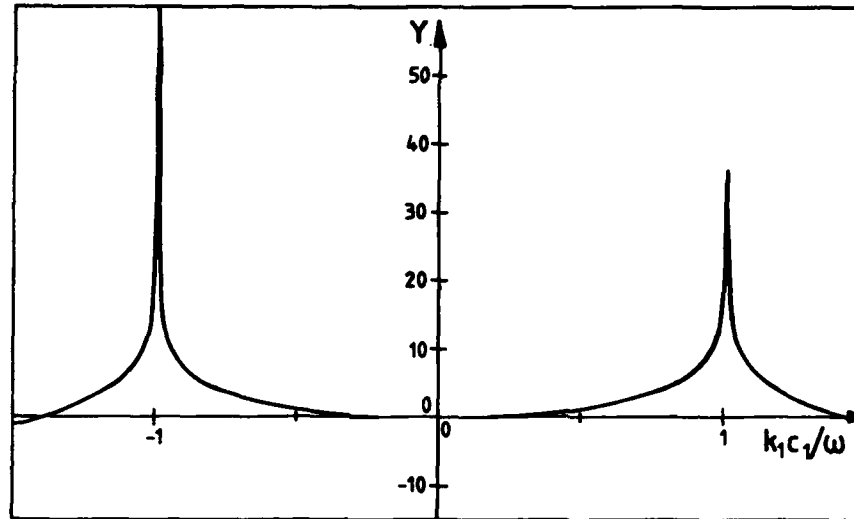

Figure 2   Plot of $Y = 20\log_{10}\left|\dfrac{\omega/c_1}{E'(0)+U'(0)k_1/\omega}\right|$ vs non-dimensional wave number for flow over a rigid wall with $M = 0.01$, $\omega\delta/c_1 = 1$, $k_2 = 0$

The curve in Figure 2 clearly demonstrates that the predicted pressure spectrum is larger for downstream propagating modes with sonic phase speeds than it is for upstream propagating modes. Roebuck and Richardson (1981, private communication) have observed this in underwater experiments.

Just as in Dowling [4] we can interpret the singularity for downstream propagating spectral elements as being due to modes which are supersonic within the slowly moving fluid in the boundary layer but subsonic in the faster moving fluid outside it. The energy in these modes therefore remains 'trapped' near the boundary layer, i.e. within a disk near the surface, and conservation of energy then suggests that downstream of the source the pressure disturbance will only decay like the inverse square-root of distance from the source, while upstream the disturbance will decay more rapidly. Hence the pressure decays more slowly with distance downstream of a source in the boundary layer than in a uniform stream, and this accounts for the stronger singularity in the pressure spectrum under an infinite region of turbulence.

It has been shown (Dowling [7]) that in the absence of a mean flow profile certain coating layers can have a beneficial effect on the surface pressure spectrum. We now go to investigate the effect of a coating layer over a hard surface.

4.2   A Coating Layer

We model the coating by a fluid layer of thickness T with density ρ_s and sound speed c_s. A sketch of the coating layer on a hard surface is given in

Figure 3. The impedance of the composite surface can be calculated in a straightforward way and we find:

$$Z = -\frac{\rho_s \omega^2}{\gamma_s} \cot \gamma_s T \qquad (36)$$

where $\gamma_s = (\omega^2/c_s^2 - k_1^2 - k_2^2)^{\frac{1}{2}}$. The pressure spectrum on the surface of the coating $x_3 = 0$ can then be obtained immediately from (32). In fact the pressure spectrum on the hard surface is of more practical interest since it can be compared more directly with the pressure on the uncoated plate. The relationship between the pressures on these two surfaces is:

Figure 3 A coating layer over a hard surface

$$\bar{p}(-T,\underline{k},\omega) = \bar{p}(0,\underline{k},\omega) \sec \gamma_s T \qquad (37)$$

and so the wall pressure spectrum on the hard surface is:

$$P(\underline{k},\omega) = \frac{|\sec\gamma_s T|^2 \; D_i^\dagger D_j^\dagger D_k D_\ell}{|E'(0)+U'(0)k_1/\omega - \rho_1\omega^2/Z|^2} \; \rho_1 U_1^3 \delta_1^5 Q_{ijk\ell}(\delta_1\underline{k},\delta_1\omega/U_1) \qquad (38)$$

where Z is given in (36). $|\sec\gamma_s T|^2 |E'(0)+U'(0)k_1/\omega-\rho_1\omega^2/Z|^{-2}$ is plotted in Figures 4 and 5 for different coating properties using values of $E'(0,\underline{k},\omega)$ obtained by numerical integration. We will explain these results by investigating the low Mach number, thin coating layer limit analytically.

When $c_s \gg |\omega|T$ and M is small:

$$E'(0) + U'(0)\frac{k_1}{\omega} - \frac{\rho_1\omega^2}{Z} \approx -i\gamma_1(1+MB) - 2\omega k_1\delta_1 \frac{M}{c_1} + \frac{\rho_1}{\rho_s}\left(\frac{\omega^2}{c_s^2} - k_1^2 - k_2^2\right)T \qquad (39)$$

This becomes small near $\gamma_1 = 0$, but can only vanish near there if:

$$\frac{\rho_1 T}{\rho_s c_1}\left(\frac{c_1^2}{c_s^2} - 1\right) - 2\frac{k_1\delta_1}{\omega}M > 0 \qquad (40)$$

Hence a coating with a sound speed higher than that in the surrounding fluid can eliminate the singularity that occurs on an uncoated hard surface for spectral elements propagating downstream with an approximately sonic phase speed. This is seen clearly by comparing Figures 2 and 4.

The inequality in (40) shows that a low-sound-speed coating can have an adverse effect and introduce new singularities into the surface pressure spectrum for upstream propagating modes which would be finite for an uncoated hard surface. This is illustrated in Figure 5. A comparison of Figures 2 and 5 shows that the low-sound-speed coating has introduced a new singularity into the surface pressure spectrum.
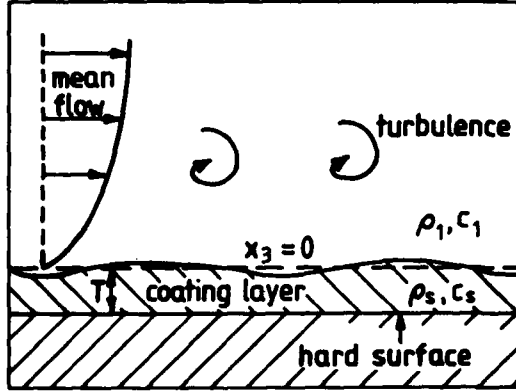
72

Figure 4 Plot of $Y = 20\log_{10}\left|\dfrac{\omega/c_1}{E'(0)+U'(0)k_1/\omega-\rho_1\omega^2/Z}\right|$ vs non-dimensional wave number for a high speed coating layer over a hard surface. $M = 0.01$, $\omega\delta/c_1 = 1$, $\omega T/c_1 = 0.5$, $c_s = 1.2c_1$, $\rho_s = 1.2\rho_1$, $k_2 = 0$
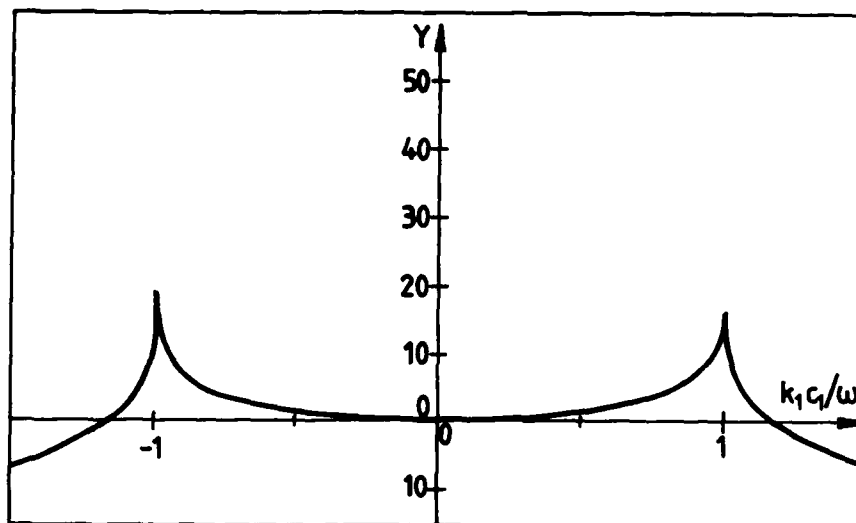

Figure 5 Plot of $Y = 20\log_{10}\left|\dfrac{\omega/c_1}{E'(0)+U'(0)k_1/\omega-\rho_1\omega^2/Z}\right|$ vs non-dimensional wave number for a low-speed coating layer over a hard surface. $M = 0.01$, $\omega\delta/c_1 = 1$, $\omega T/c_1 = 0.5$, $c_s = 0.9c_1$, $\rho_s = 1.2\rho_1$, $k_2 = 0$
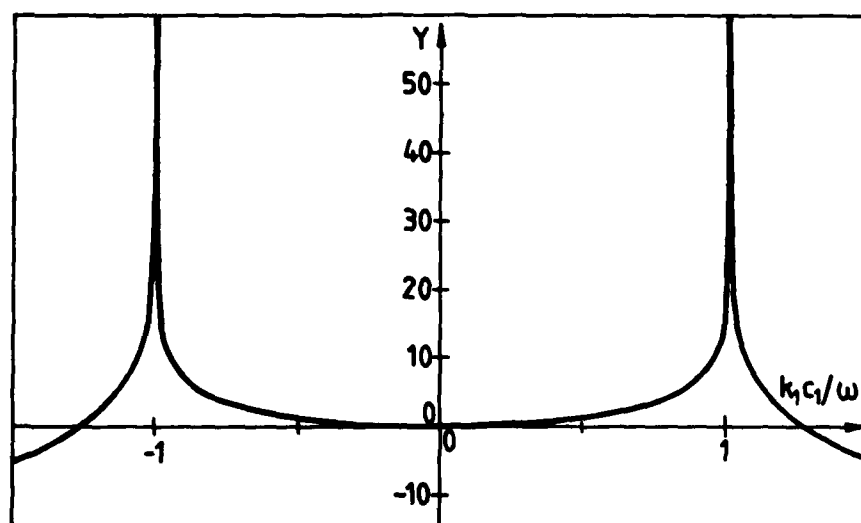
73

5. CONCLUSIONS

An expression for the low-wavenumber wall pressure spectrum under a turbulent boundary layer has been derived in a way which brings out explicitly the effects of the mean flow profile and the surface flexibility. It is found that the hard wall pressure spectrum has a singularity for spectral elements that propagate downstream with approximately sonic phase speeds, but that it is finite for all upstream propagating modes. It is shown that a coating with a sound speed greater than that of the fluid can eliminate the singularities in the pressure spectrum for these downstream propagating modes, but that a low-sound-speed coating has an adverse effect.

REFERENCES

1. Chase, D.M. and Noiseux, C.F., "Turbulent wall pressure at low wave-numbers: Relation to nonlinear sources in planar and cylindrical flow," Journal of the Acoustical Society of America, Vol.72, 1982, pp.975-982.

2. Ffowcs Williams, J.E., "Surface-pressure fluctuations induced by boundary-layer flow at finite Mach number," Journal of Fluid Mechanics, Vol.22, 1965, pp.507-519.

3. Bergeron, R.F., "Aerodynamic sound and the low-wavenumber wall-pressure spectrum of nearly incompressible boundary-layer turbulence," Journal of the Acoustical Society of America, Vol.54, 1973, pp.123-133.

4. Dowling, A.P., "Flow-acoustic interaction near a flexible wall," Journal of Fluid Mechanics, Vol.128, 1983, pp.181-198.

5. Morse, P.M. and Feshbach, H., Methods of Theoretical Physics, McGraw-Hill, 1953.

6. Michalke, A., "On spatially growing disturbances in an inviscid shear layer," Journal of Fluid Mechanics, Vol.23, 1965, pp.521-544.

7. Dowling, A.P., "The low wavenumber wall pressure spectrum on a flexible surface," Journal of Sound and Vibration, Vol.88, 1983, pp.11-25.

INFLUENCE OF DIRECTIONAL SURFACE IMPEDANCE ON
THE LOW WAVENUMBER PRESSURE SPECTRUM

A. J. Kalinowski
Naval Underwater Systems Center
New London, Connecticut

ABSTRACT

Dowling has extended the Lighthill sound analog so that the flow induced noise resulting from fluid passing over a compliant surface can be computed, by knowing the compliant surface impedance as a function of the in-plane wavenumber and frequency. The implementation of the complete theory requires, as yet, unavailable experimental information about certain turbulent source terms, consequently, results are given here in the form of a fluid pressure spectrum multiplier, rather than the actual pressure spectrum itself. The Dowling extension was previously applied to surfaces whose surface impedance was dependent on the wavenumber vector magnitude but independent of the vector direction. For slow mean flow field velocities, the computed pressure spectrum multiplier likewise exhibits a similar independence on the wavenumber vector direction. In this paper, surfaces which exhibit both a magnitude and direction dependent impedance are examined and their influence on the shape of the corresponding fluid pressure spectrum multiplier is investigated.

NOMENCLATURE

C_a	acoustic sound speed of fluid (in./sec)
C_p	backing plate flexure wave speed (in./sec)
C_m	backing plate membrane wave speed (in./sec)
C_d	dilational wave speed in layer (in./sec)
C_s	shear wave speed in layer (in./sec)
D_{ij}	spectrum shape terms
D	layer thickness (in.)
h	turbulent boundary layer thickness (in.)
k_1, k_2	spectrum streamwise, spanwise wavenumbers (in.$^{-1}$)
k	magnitude of wavenumber vector, $\bar{k} = k_1 \bar{i} + k_2 \bar{j}$, (in.$^{-1}$)
k_a	ω/c_a, acoustic wavenumber
M_c	compliant surface wall pressure spectrum multiplier
M_r	rigid surface wall pressure spectrum multiplier
p	fluid pressure (psi)
p_o	equation of state reference pressure (psi)
$Q_{ijk\ell}$	integrated turbulent source terms
$R = (1 + U_1 k_1/\omega)$	flow correction parameter
$\dot{u}_1, \dot{u}_2, \dot{u}_3$	solid layer velocity components (in./sec)

T	plate thickness (in.)
U_1	streamwise flow velocity (in./sec)
v_1, v_2, v_3	fluid velocity components (in./sec)
$X(k_1,k_2,\omega)$	surface displacement impedance $= (i\omega Z$ (lb/in.^{3})
$Z(k_1,k_2,\omega)$	surface velocity impedance $(p/\dot{u}_3)$ (lb-sec/in.^{3})
ρ_0	at-rest fluid mass density (lb - sec^2/in.^{4})
ρ_ℓ	layer mass density (lb - sec^2/in.^{4})
ρ_p	plate mass density (lb - sec^2/in.^{4})
$\eta_{p1}, \eta_{p2}, \eta_{p12}$	plate damping parameters
η_s, η_d	shear and dilatation isotropic damping parameters
ω	spectrum frequency $(2\pi f)$ (rad/sec)

INTRODUCTION

In this paper, we address the problem of estimating the wall pressure spectrum existing at the interface between a compliant surface and viscous fluid, while a turbulent flow field of mean flow velocity, U_1, is passing over the semi-infinite representation of the compliant surface. The turbulence in the boundary layer existing at the deformable fluid-surface interface generates sound components that are different than those present for the same flow, U_1, passing over a rigid surface. The notion that the sound field generated by a turbulent boundary layer is greatly influenced by the surface interface properties has been considered by Ffowcs-Williams (1). Some of the early attempts at predicting the wall pressure spectrum, considered the compliance, but not the compressibility of the fluid (2), while others, treated the compressibility but not the compliance (3). Dowling, (4), extended the Lighthill sound analogy (5) and allowed for both compressibility and compliance simultaneously while including the effect of the mean flow profile in the turbulent boundary layer. This last work is particularly significant because the formulation is in a generalized form which permits one to evaluate a candidate compliant surface and corresponding pressure spectrum once the surface velocity impedance $Z(k_1,k_2,\omega)$, is defined as a function of the streamwise and spanwise wavenumbers, k_1, k_2 and frequency ω. The effect of the mean flow is described by terms appearing in the spectrum formula having the form $(1 + U_1 k_1/\omega)$. In underwater applications, which will be the central focus of this paper, the flow speed, U_1, is substantially smaller than the acoustic sound speed, C_a, consequently for sonic or supersonic spectral elements, $(U_1 k_1/\omega)$ can be dropped in comparison to unity. This approximation simplifies the analytical form of the spectrum and Dowling, (6), has given guidelines regarding the expected alteration of the pressure spectrum as a consequence of changing wave speeds for a surface model consisting of an isotropic material (having zero shear modulus) attached to a thin flexible backing plate.

In the work presented herein, the reference (6) Dowling compliant surface model is generalized in the following respects:

1. the upper layer has different boundary conditions (selected as options) in the streamwise and spanwise directions (e.g., slip vs fixed base attachment conditions)

2. the upper layer has a non-zero shear modulus

3. the lower plate has membrane stiffness

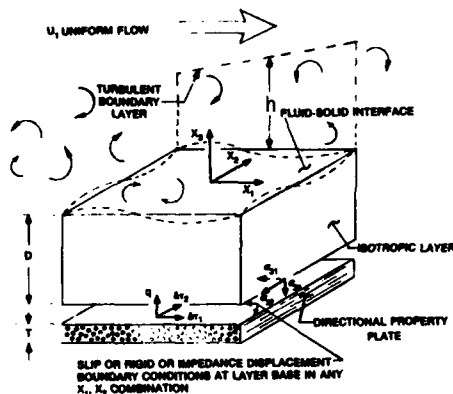4. the lower plate has optional directional material properties.
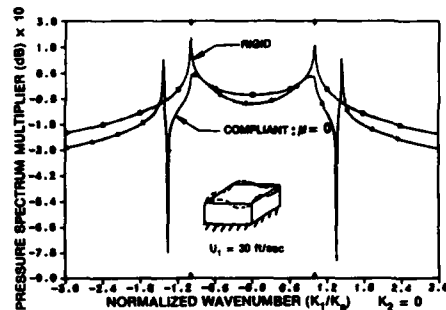
FIGURE 1. SURFACE IMPEDANCE MODEL

FIGURE 2. INFLUENCE OF FLOW SPEED ON SYMMETRY OF WALL PRESSURE SPECTRUM MULTIPLIER. 20 LOG₁₀(|R_u M_u|), FOR BASE CASE LAYER WITH FIXED BOTTOM AT k_u = ω/6.

A sketch of the different surface models is shown in Fig. 1, where various boundary condition combinations can potentially be examined. The mixing of unlike boundary conditions in the k_1, k_2, directions requires a three dimensional solution for the surface impedance. The resulting surface impedance will not depend on the magnitude of the wave vector number, $k^2 = k_1^2 + k_2^2$ alone but will depend on the individual components k_1, k_2 as well. For small $U_1 k_1$ in comparison to ω, the shape of the pressure spectrum shape is not substantially affected by flow velocity, U_1, consequently distortions of the pressure spectrum will mainly be altered by surface impedances, $Z(k_1, k_2)$ that depend on the direction and magnitude of the wavenumber vector.

The remainder of the paper will concentrate on examining the manner in which the above mentioned four modifications alter the shape of the pressure spectrum.

WALL PRESSURE SPECTRUM

The central result of (4) is given in form of a wall pressure spectrum, $P(\bar{k}, \omega)$, which is applicable to compressible or incompressible flow, namely

$$P(\bar{k}, \omega) = D_{ij} D_{k\ell}^* \, \rho_0^2 \, U_1^3 \, h^5 \, Q_{ijk\ell} \tag{1}$$

where ρ_0 is the at-rest acoustic noise density of the fluid, U_1 is the mean flow velocity, h is the boundary layer thickness, D_{ij} is the term which describes how the turbulent source terms, and $Q_{ijk\ell}$ radiate sound within the boundary layer over a compliant surface (usual indicial summation is implied over repeated indices where indices take on values 1,2,3) and * denotes complex conjugate.

The $Q_{ijk\ell}$ expression is a result of spatially integrating the spectrum function $\Gamma_{ijk\ell}$, where this quantity is the Fourier transform of the crosscorrelation of the turbulent sources.

Specifically,

$$Q_{ijk\ell} = \frac{1}{\rho_0^2 \, U_1^3 \, h^5} \iint \Gamma_{ijk\ell}(y_3, \, y_3', \, \bar{K}, \, \omega) \, dy_3 \, dy_3' \qquad (2)$$

with
$$\Gamma_{ijk\ell} = \iiint \overline{H \, T_{ij}(\bar{y},\tau) \, H \, T_{k\ell}(y_1 + \Delta_1, \, y_2 + \Delta_2, \, y_3', \, \tau + \tau_0)} \, \cdot$$

$$e^{-ik_\alpha \Delta_\alpha} \, e^{-i\omega\tau_0} \, d\Delta_1 \, d\Delta_2 \, d\tau_0 \qquad (3)$$

where H is a unit Heaviside function which is unity in the boundary layer and zero elsewhere, Δ_1, Δ_2, τ_0 are shift dummy variables for the correlation, over bar denotes an ensemble average and finally, T_{ij} represents the turbulent source terms employed in the Lighthill analogy.

Specifically, the source term is given by

$$T_{ij} = \rho v_i \, v_j + P_{ij} - (\rho - \rho_0) \, C_a^2 \, \delta_{ij} \qquad (4)$$

where ρ is the fluid mass density, v_i is the fluid particle velocity, P_{ij} is the compressive stress tensor, and δ_{ij} is the Kronecker delta function.

The details regarding the derivation of $Q_{ijk\ell}$ are rather lengthy and the reader is referred to the source (4) for additional details. The shape factors, D_{ij} are given by

$$D_{\alpha\beta} = \frac{X^* \omega^2}{E_c(\bar{K},\omega)}\left[k_\alpha \, k_\beta \, R^2\right] \qquad \alpha, \beta = 1 \text{ or } 2$$

$$D_{\alpha 3} = D_{3\alpha} = \frac{X^* \omega^2}{E_c(\bar{K},\omega)}\left[k_\alpha \gamma_1\right] \qquad (5)$$

$$D_{33} = \frac{X^* \omega^2}{E_c(\bar{K},\omega)}\left[\gamma_0^2 \, R^2\right]$$

where $X = i\omega Z$, thus $X^* = -i\omega Z^*$,

$$E_c(\bar{K},\omega) = i\omega^2 \gamma_1 X^* - \rho_0 \omega^4 \, R^2 + \rho_0 \omega^4 i\gamma_1 h + \omega^2 \gamma_0^2 h X^* R^2$$

and
$$\gamma_0 = \left[\frac{\omega^2}{C_a^2} - k^2\right]^{1/2} , \quad \gamma_1 = \left[\left(\frac{\omega R}{C_a}\right)^2 - k^2\right]^{1/2}$$

Here R is a parameter involving the effect of the velocity on the pressure spectrum and is defined by

$$R = 1 + U_1 k_1/\omega \qquad (7)$$

78

The root of γ_0 is chosen so that when γ_0 is real, γ_0 has the sign of ω and when γ_0 is purely imaginary (i.e., $k^2 > \omega^2/C_a^2$), then the imaginary part of γ_0 is made positive. The root of γ_1 is picked similarly, where γ_1 has the same sign as $R\omega$ when γ_1 is real and when γ_1 is purely imaginary, the imaginary part of γ_1 is made positive.

The surface impedance, $Z(\overline{k},\omega)$, is defined as the ratio of the surface-pressure perturbation, $p - p_0$, to the normal surface velocity $\dot{u}_3$ at wavenumber $\overline{k}$ and frequency ω. The three dimensional impedance derivation for the Fig. 1 layer-plate combination is lengthy and is treated in the appendix section.

Absolute Evaluation

The absolute evaluation of the Dowling wall pressure spectrum given by equation (1), requires that crosscorrelation of the turbulent source terms, T_{ij} be known in order to compute the $Q_{ijk\ell}$ terms appearing in the spectrum equation. In (4), it is suggested that the $Q_{ijk\ell}$ quantities should be independent of compressibility effects and therefore can be estimated on the basis of incompressible flow theory. This is no small task indeed. One possibility for computing the $Q_{ijk\ell}$ terms would be to employ a large eddy simulation computer of the type employed in reference (7), and employing the detailed flow structure, compute the source terms defined by equation (4), and subsequently compute the $Q_{ijk\ell}$ quantities. An alternative experimental approach would require measurements of the T_{ij} source terms throughout the three dimensional space within the boundary layer. This is a difficult task, since 81 terms are needed to fill $Q_{ijk\ell}$ array. Another question arises regarding whether the $Q_{ijk\ell}$ terms are only weakly affected by the motion of the surface. If this is true, these integrated source terms could be determined once for a flow over a rigid surface and reused in conjunction with the D_{ij} compliant surface terms to predict the spectrum. At this point in time, there does not appear to be enough information available, experimental or otherwise, to compute the full $Q_{ijk\ell}$ expression.

Relative Evaluation

The next best approach would be to examine the multiplier, $D_{ij} D_{k\ell}^*$, operating on the $Q_{ijk\ell}$ terms in the equation (1) spectrum. The changes in these quantities could be used to give an indication of trends in the pressure spectrum. Searching for trends in all of the terms in the $D_{ij} D_{k\ell}^*$ array is not practical. Instead, one can observe that all of the components of the D_{ij} array, have the term $X^* \omega^2/E_c(\overline{k},\omega)$ as a common factor. Moreover, all of the information regarding the details of the surface compliance is included in this expression (noting that the compliance information is also affecting $E_c(\overline{k},\omega)$ since it is also a function of X^*). The compliant surface wall pressure multiplier then is defined as

$$M_c = \left| X^* \frac{\omega^2}{E_c(\overline{k},\omega)} \right| \tag{8}$$

and is used as a measure for comparing the relative effect of compliance on the wall pressure spectrum from one compliant surface to another. A single plot of M_c versus wavenumber is useful towards obtaining information about the shape and potential singularities in the spectrum. It is noted that the M_c multiplier is similar to the spectrum multiplier called, F, in reference (6). An additional plot of the corresponding multiplier when the surface is rigid would be even more valuable towards sorting out potentially good compliant surfaces from bad ones. The rigid multiplier, M_r, is obtained simply by taking the limit as the displacement surface impedance $X \to \infty$ in equation (8) which results in the expression

$$M_r = \left| \frac{\omega^2}{E_r(\bar{K},\omega)} \right| \tag{9}$$

where $E_r(\bar{K},\omega) = i\omega^2 \gamma_1 + \omega^2 \gamma_0^2 h R^2$

The units of M_r are length, consequently it is convenient to nondimensionalize M_c or M_r by dividing through by length scale, which is selected as the acoustic wavenumber, $1/k_a = C_a/\omega$. The plots of M_c or M_r we intend to make are holding ω = constant, consequently normalizing the plotted quantity with respect to ω creates no unusual distortion of the function but rather places the shape multipliers in a range more desirable for plotting purposes. Since the pressure spectrum is multiplied by $D_{ij} D_{k\ell}^*$, the M_c factor appears as a squared factor in the wall pressure spectrum, consequently the quantity we finally display is $(k_a M_c)^2$ where 10 times the $\log_{10}$ of this quantity (or equivalently, $20 \log_{10} |k_a M_c|$) is actually plotted since the range of the multiplier spans several orders of magnitude. Similarly, $20 \log_{10} |k_a M_r|$ is plotted for the rigid wall pressure spectrum.

Consequently, log plots of $|k_a M_c|$ compared to $|k_a M_r|$ will be used to judge the effectiveness of a candidate compliant surface as measured against the same flow over a rigid surface.

Spectrum Trends for Underwater Acoustics

In the case of underwater acoustics, the $U_1 k_1/\omega \ll 1$, therefore the R factor is ≈ 1.0. Consequently setting $R = 1$ in equations (5-8) leads to some substantial simplifications.

(i) Singularity Trends

After some algebraic manipulations, the multipliers can be written in the form

$$M_c \approx \left| \frac{1}{\sqrt{1 + (\gamma_0 h)^2}\,\left(i\gamma_0 - \dfrac{\omega^2 \rho_0}{\chi^*}\right)} \right| \tag{10a}$$

$$\left. \right\} \text{for } k^2 \le k_a^2$$

$$M_r \approx \left| \frac{1}{\sqrt{1 + (\gamma_0 h)^2}\,\gamma_0} \right| \tag{10b}$$

and

$$M_c \approx \left| \frac{1}{(1 + \tilde{\gamma}_0 h)\left(\tilde{\gamma}_0 + \dfrac{\omega^2 \rho_0}{\chi^*}\right)} \right| \tag{11a}$$

$$\left. \right\} \text{for } k^2 \ge k_a^2$$

$$M_r \approx \left| \frac{1}{(1 + \tilde{\gamma}_0 h)\,\tilde{\gamma}_0} \right| \tag{11b}$$

where $\tilde{\gamma}_0 = \left| \sqrt{k^2 - k_a^2} \right|$

Upon observing the above relations, it can be seen that the rigid surface multiplier, M_r, has a singularity at $\gamma_0 = 0$ and at $\tilde{\gamma}_0 = 0$, i.e., $k = \pm k_a$.

Next consider the case where the governing equations of motion for the deformable body produce a surface displacement impedance X, that is real and thus, $X^* = X$ (e.g., there is no complex phase angle between the surface load, ΔP, and the corresponding displacement response, u_3). The displacement impedance for an infinite plate supporting flexural waves is an example of this (e.g., equation A-28). Upon examining the denominator of Equation (10a), it can be seen there is no real value of X^* that makes the denominator zero and consequently, M_c has no singularities when $(k_1^2 + k_2^2) < k_a^2$. However, the

denominator of equation (11a) has a singularity when $X^* = -\rho_0 \omega^2 / \tilde{\gamma}_0$ and $k_1^2 + k_2^2 > k_a^2$.

When damping is included in the equations of motion for the structure, the surface impedance typically is complex, where $X = X_r + iX_i$, $X_i \neq 0$, thus $X^* = X_r - iX_i$. Substituting this last expression for X^* into equation 11a , it is observed that M_c no longer has singularities when $k^2 \geq k_a^2$ since the term in the denominator becomes

$([\tilde{\gamma}_0 + X_r \rho_0 \omega^2 / |X|^2] + i[X_i \rho_0 \omega^2 / |X|^2])$ and no value of X_r, X_i will make this whole term in parenthesis zero. For small damping, the peaks of the M_c multiplier singularities will be rounded off. In the range $k^2 \leq k_a^2$, substituting $X^* = X_r - iX_i$ into equation (10a) yields a term in the denominator of the form $([-\omega^2 \rho_0 X_r / |X|^2] + i[\gamma_0 - \omega^2 \rho_0 X_i / |X|^2])$, thus, it is possible, as a result of having a complex X, to introduce a new singularity at wavenumber (k_1', k_2') where $X_r(k_1', k_2') = 0$ and simultaneously, $X_i(k_1', k_2') = \rho_0 \omega^2 / \gamma_0$. Elastic solids without damping can also exhibit a non-real X, for example if the solid were an infinite solid in the x_3 direction with no shear modulus, the surface impedance is $Z = -\rho_0 C_d$, hence $X^* = i\rho_0 C_d \omega$.

(ii) Relative Magnitude Trends

Although the position of the singularities is important, of equal importance is the question of whether the compliant wall pressure spectrum is reduced in magnitude over the corresponding rigid surface spectrum. It is desirable to have $M_r/M_c \gg 1$ over a range of low wavenumbers in the domain of interest. Dividing equations (11) into (10) give such a measure and lead to the result

$$M_r/M_c = \left| i\gamma_0 - \omega^2 \rho_0 / X^* \right| / |\gamma_0| \quad \text{for } k^2 \leq k_a^2 \tag{12a}$$

$$M_r/M_c = \left| \tilde{\gamma}_0 + \omega^2 \rho_0 / X^* \right| / |\tilde{\gamma}_0| \quad \text{for } k^2 \geq k_a^2 \tag{12b}$$

Again, consider the case where X^* is real in the surface impedance equations, i.e., $X = X$. Therefore when $k^2 \geq k_a^2$, small positive X displacement impedances are desirable to insure $M_c < M_r$ and when $k^2 < k_a^2$, small $|X|$ impedances will insure $M_c < M_r$. Eventually as the surface impedance becomes softer and softer, i.e., as $X \to 0$, the implementation of an Eulerian coordinate system used in (4) for the fluid which interfaces with large Lagrangian deformations of the compliant solid surface would require some modifications in the analysis to properly treat the boundary condition across the fluid solid interface. Specifically when the

81

deformations are large, the fluid-solid boundary condition cannot be evaluated along the fixed Eulerian plane, $x_3 = 0$, but rather along the actual deformed surface of the solid surface.

In this paper, we have focused attention evaluating the spectrum at the fluid-solid interface. If one wishes the spectrum of response at some intermediate level within the solid, then an additional transfer function relation is needed which relates surface response to response at some other plane in the solid as was done for example in (6).

EXAMPLES OF INFLUENCE OF SURFACE TREATMENT ON WALL SPECTRA

The most general form of the compliant surface treatment in this paper is illustrated in Figure 1 and consist of an isotropic layer of thickness, D, (with optional dilatational damping parameter, n_d, and shear damping parameter, n_s as defined in the Appendix).

Various bottom attachment boundary conditions are treated, with emphasis on ones which result in surface impedances that depend on both the magnitude and direction of the wavenumber vector, $\bar{k}$. The derivation of the surface impedance X, for each of the cases considered herein is lengthy and is therefore discussed seperately in th Appendix. The number of parameters governing the pressure spectrum multiplier for the most general model (i.e. the upper layer-bottom plate combination) are substantial, consequently a selected set of demonstration examples are used to illustrate certain features. The spectrum frequency, f, is held constant at 6000 Hz in all spectrum results and corresponds to one employed in reference (6). A particular set of undamped material constants and material thickness for the upper isotropic layer will be referred to from herein as the "base case layer":

$$\lambda^r = 105035.2 \text{ (psi)}; \qquad \mu^r = 5082.3 \text{ (psi)}$$
$$\rho_\ell = .000072 \text{ (lb-sec}^2/\text{in}^4); \qquad D = 10 \div 2.54 \text{ (in)}$$

base case layer

where λ^r, μ^r are the real layer elastic Lame' constants, ρ_ℓ is the layer mass density and D the layer thickness. Throughout this paper, the fluid acoustic properties (for water) are taken as $\rho_0 = .000096$ (lb-sec $^2/\text{in}^4$), $b_0 = 345600.0$ (psi) where b_0 is the fluid bulk modulus. For reference purposes, the base case layer and fluid moduli and densities can be written in terms of the layer dilational wave speed, C_d, and shear wave speed, C_s, and fluid acoustic wave speed, C_a, where $C_a = 60,000$ in/sec, $C_d = (2/3) \cdot C_a$ and $C_s = C_d/\sqrt{51}$. The TBL thickness, h, is taken as 2.0 (in) in all examples.

Influence of Flow Speed on Pressure Spectrum

The compliant pressure spectrum multiplier relationship given by equation (8), holds for both liquids and gases, however the $U_1 k_1/\omega$ term will make the pressure spectrum weakly depend on both the magnitude and direction of the wavenumber vector $\bar{k}$, even when the compliance, X, depends only on the magnitude, k. To obtain a better understanding of how the pressure spectrum is affected by surfaces with wavenumber direction dependence, the simpler equations (10) and (11) are later used which are based on dropping the $U_1 k_1/\omega$ term in equations (8) and (9). Thus, any observed directionality dependance of the pressure spectrum will be due entirely on the directionality dependence of the surface impedance alone.

The weak dependence of the spectrum on the $U_1 k_1/\omega$ term, with water as the acoustic medium, can be illustrated by comparing the upstream ($+k_1$) and the downstrea· $- k_1$) modes for $k_2 = 0$. As an example, consider a base case layer ma .rial and thickness, where $C_d = (2/3)C_a$, and shear is omitted, i.e. $C_s = 0$ and where the flow velocity is $U_1 = 30$ ft/sec.

Since $C_s = 0$, the layer depends only on the dilational wave speed in the material. The surface impedance

$$X = -\omega^2 \rho_\ell \, \text{Tan}(\gamma_d \, D)/\gamma_d \quad \text{with} \quad \gamma_d = \sqrt{k_d^2 - k^2} \tag{13}$$

can be obtained from reference (6) by letting the attached plate mass $\to \infty$; or alternatively, employing the procedure given in the Appendix, but using only the dilatation potential ϕ in conjunction with boundary conditions corresponding to the first of (7-A) and third of (10-A). Substituting the equation (13) impedance with a 30 ft/sec flow velocity into the more general equations (8) and (9) lead to the result shown in Figure (2). In this plot and all similar ones shown later, the small diamond marks on the horizontal axis refer to the acoustic wavenumber. As pointed out in (4), for $U_1 \neq 0$, $E_r(k_1,0,\omega)$ will have zeros only when k_1 and ω are opposite in sign (i.e. for downstream propagating modes), consequently in the Figure (2) result, the $-k_1$ rigid curve spike near $k_1/k_a = -1$ has an infinite peak. Other than the rounding off of the rigid curve singularity, at $k_1/k_a = +1.0$, both the rigid and compliant surface wall pressure spectrum multipliers are not significantly altered, thus justifying the omission of the $U_1 k_1/\omega$ term. In fact, except for the rounded off peak, overlaying the curves generated by approximate equation (10) and (11) onto the Figure (2) curves gave differences that did not show up graphically. The spectrum with the $U_1 k_1/\omega$ term dropped is shown in Figure 3-a, and as seen, there is no significant difference between the two curves. In all cases that follow, the approximate equations (10) and (11) will be used to display results, further, since no new information exist for negative wavenumbers, only the plus values are considered.

Influence of Shear Modulus and Damping Spectrum

Here the effect of introducing shear resistance and damping into the isotropic layer model is examined. When shear effects are omitted, i.e. $C_s = 0$, the fixed bottom, 10 cm isotropic layer yields the spectrum shown in Figure 3-a. It is observed that the spike labeled dilatational effect occurred when the normalized spectrum wavenumber, k_1/k_a, was roughly equal to the normalized dilatational wavenumber $k_d/k_a = (\omega/C_d)/(\omega/C_a) = 3/2$, where $C_d = (2/3)C_a$ for this material. The singularities in the spectrum do not occur exactly at the singularities in the impedance, X, (for example, observing equations (10a) or (11a), clearly M_c is not infinite when X^* is infinite). However in this example, the impedance singularity, with the aid of equation (13), is at $\gamma_d D = \pi/2$, or equivalently at $k_1/k_a = [(3/2)^2 - (5/2D)^2]^{1/2}$. Because the Tan $(\gamma_d D)$ changes so rapidly when moving only slightly away from this root, the value of k_1 which makes $X^* = -\rho_0 \omega^2/\gamma_0^2$ in equation (11a) is also in the neighborhood of the impedance singularity.

The effect of the shear modulus on the form of the pressure spectrum can be achieved by redoing the same problem just described, except now the shear wave speed is set at $C_s = C_d/\sqrt{51}$, while maintaining the same dilational wave speed, $C_d = (3/2)C_a$, as before. The impedance for this case is developed in section (i) of the Appendix. The new spectrum multiplier is shown in Figure 3b. The effect of the shear modulus was to shift the dilatational peak slightly to the left and introduce a new spike that is labeled layer shear effect. Both spikes result in a compliant spectrum multiplier that locally rises above the rigid spectrum mulitplier. In Figure (3c), damping was introduced by assigning complex values to the Lame' constants corresponding to a dilatational damping ratio, n_d, of .05 and a shear ratio n_s, of 0.10. Further details about these constants are given in the Appendix. As shown by the figure, the damping substantially topped off the peaks in the compliant spectrum multiplier.
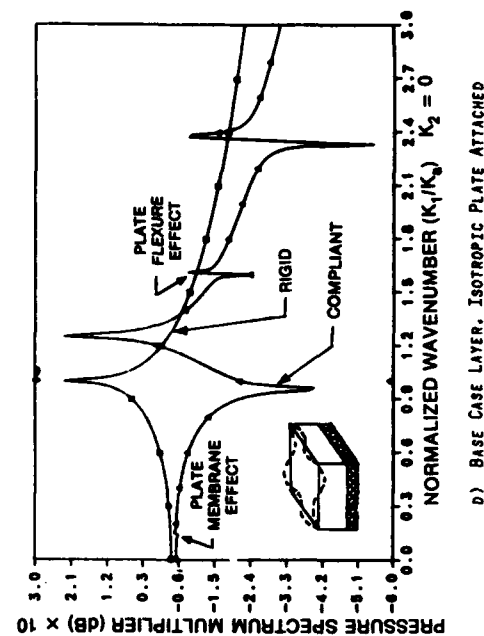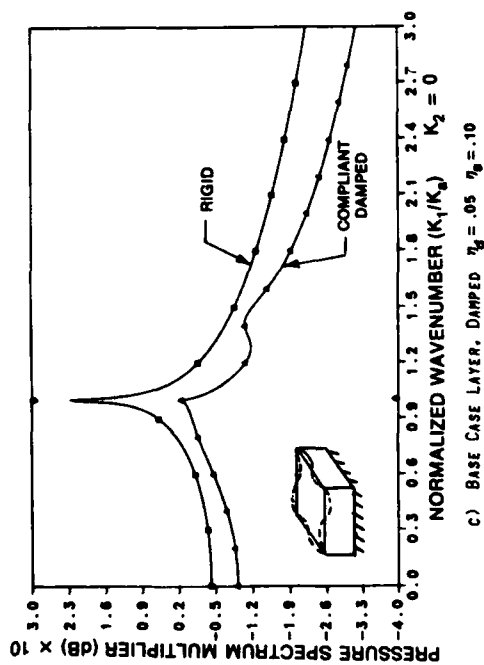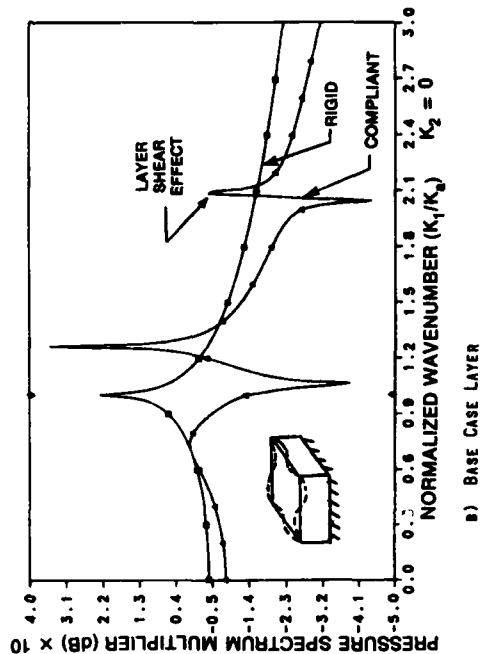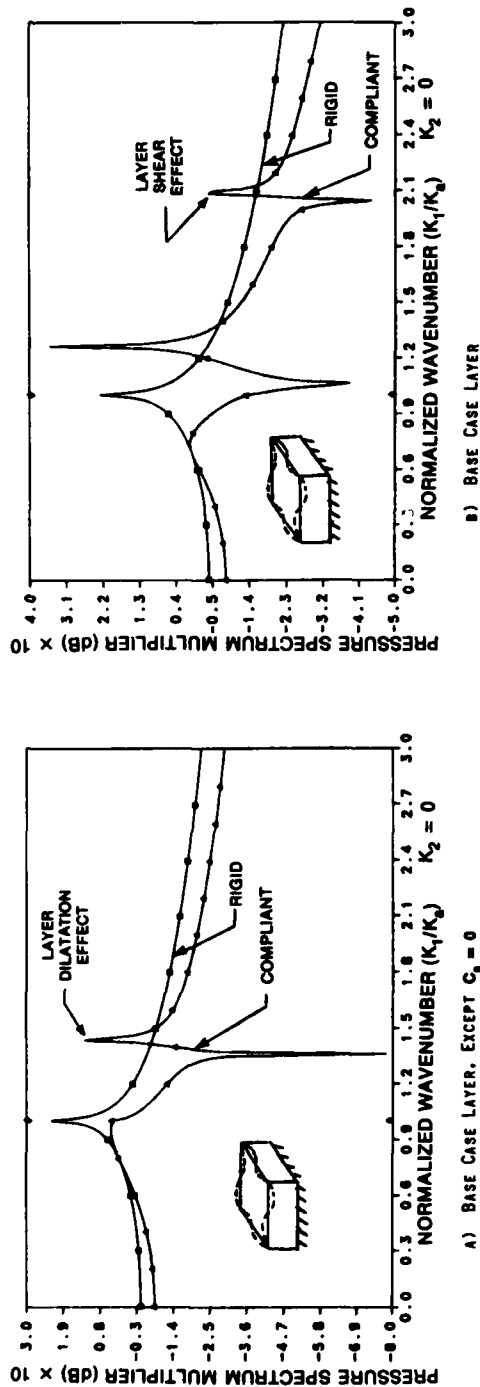
FIGURE 3. INFLUENCE OF VARIOUS ISOTROPIC SURFACE TREATMENTS ON WALL PRESSURE SPECTRUM MULTIPLIER, $20 \log_{10}(|k_a M_c|)$, AT $k_a = \pi/5$.

84

Influence of Plate Attachment on Pressure Spectrum

In this case, the fixed bottom is removed and is replaced with a 1 cm thick isotropic plate, which is attached to the base case layer on the top face of the plate and is free of surface tractions on the bottom face. The plate has a Young's modules of $E = 10.92 \times 10^6$ psi, a Poisson's ratio of $v=.3$, and a mass density of $\rho_p = .00017$. The equivalent orthotropic elastic constants that reduce to the isotropic case for the plate can be obtained from (9)

$$E_{11} = E_{22} = E/(1 - v^2), \quad E_{12} = v \, E_{11}, \quad G = E/[2(1 + v)] \tag{14}$$

and are employed in the layer-to-plate impedance formulation given in the Appendix. The plate parameters used here are in a range where the thin plate theory assumptions are valid at the frequency and plate thickness considered. The resulting spectrum multiplier is shown in Figure 3d where it is observed that dilational and shear peaks are roughly in the same position, but have been altered because the attached plate does not offer the same rigid bottom impedance boundary condition experienced by the Figure 3b case.

The membrane and flexure wave speeds of the freely propagating waves in the unattached plate alone are $k_m/k_a = .225$ and $k_f/k_a = 1.71$ respectively. The two new peaks, labeled plate membrane effect and plate flexure effect occur at roughly these respective normalized wave numbers. This case illustrates that the potential for unwelcomed spikes in the spectrum is greater with increased complexity of the surface configuration.

Influence of Directional Boundary Conditions on Pressure Spectrum

In this example, the notion of altering the shape of the pressure spectrum multiplier is considered. For example, it may be desirable to eliminate one or more spikes in the streamwise direction $(k_1,0)$ while allowing the the spikes to remain in the spanwise direction $(0,k_2)$. One way of exploring this possibility is to change the boundary condition in x_1 direction while leaving the x_2 direction boundary condition the same. Consider again the base case layer model, except here the shear traction, $\sigma_{31}(x_1,x_2,-D)$ at the layer bottom is released (i.e. set equal to zero) instead of the zero velocity boundary condition used previously. The impedance for this case is developed in part (ii) of the Appendix. Thus the Figure 3b case is resolved under the same conditions, except the layer bottom is allowed to slip in the x_1 direction. The new directional results are presented in Figure 4, where the spectrum curves in Figure 4a and 4b are cuts in the spectrum $\overline{k} = (0,k_2)$ and $(k_1,0)$ respectively. It is observed upon comparing these two plots, that the layer shear spike is removed from the $0 < k_1/k_a < 3$ range of interest along the k_1 at Figure 4b, while it remains along the k_2 cut, in Figure 4a. The transition from the $(k_1,0)$ cut to the $(0,k_2)$ cut can be viewed by plotting the spectrum multiplier versus the wavenumber direction (where $\theta = \arctan(k_2/k_1)$), while holding $k^2 = k_1^2+k_2^2$ = constant, and is illustrated in Figure 4c for three different values of $k/k_a = 1.2$, 1.89 and 2.99 respectively (note $\theta = 0^0 \rightarrow (k_1,0)$ and $\theta = 90^0 \rightarrow (0, k_2))$. For comparative purposes, the same type of plot for the new slip boundary condition is shown in the adjacent Figure 4d, drawn to the same scale. It is noted that the $\theta = 0^0$ spectrum levels of Figure 4c slipping boundary case are about equal or lower than the corresponding levels of 4d fixed boundary case.

Finally, another view of the overall full spectrum can be achieved by making a 3-dimensional carpet plot of the resulting spectrum. For example, in Figure 5 the totally fixed bottom (Figure 3b case) and x_1-slip bottom (Figure 4a, 4b case) are illustrated in Figure 5b and 5c respectively. All the plots in Figure 5 are labeled with the same contour levels, however the computer selected vertical scales might be slightly different. It is noted
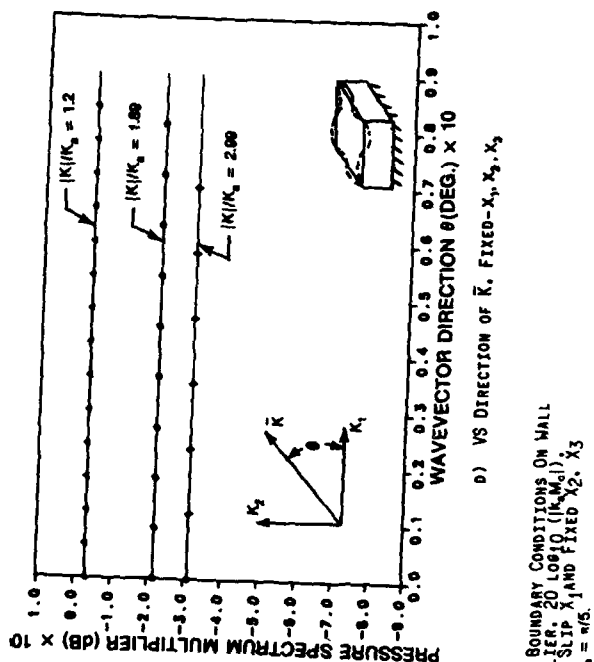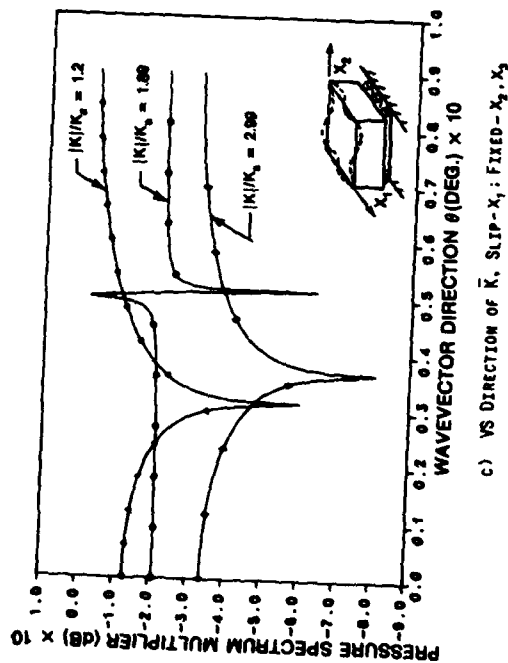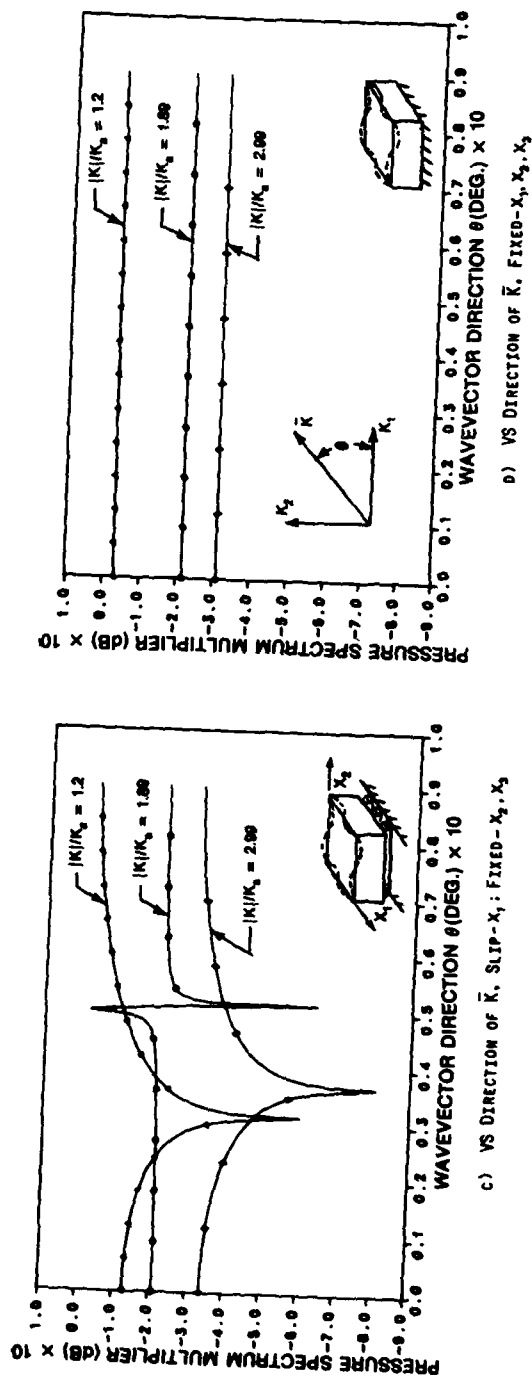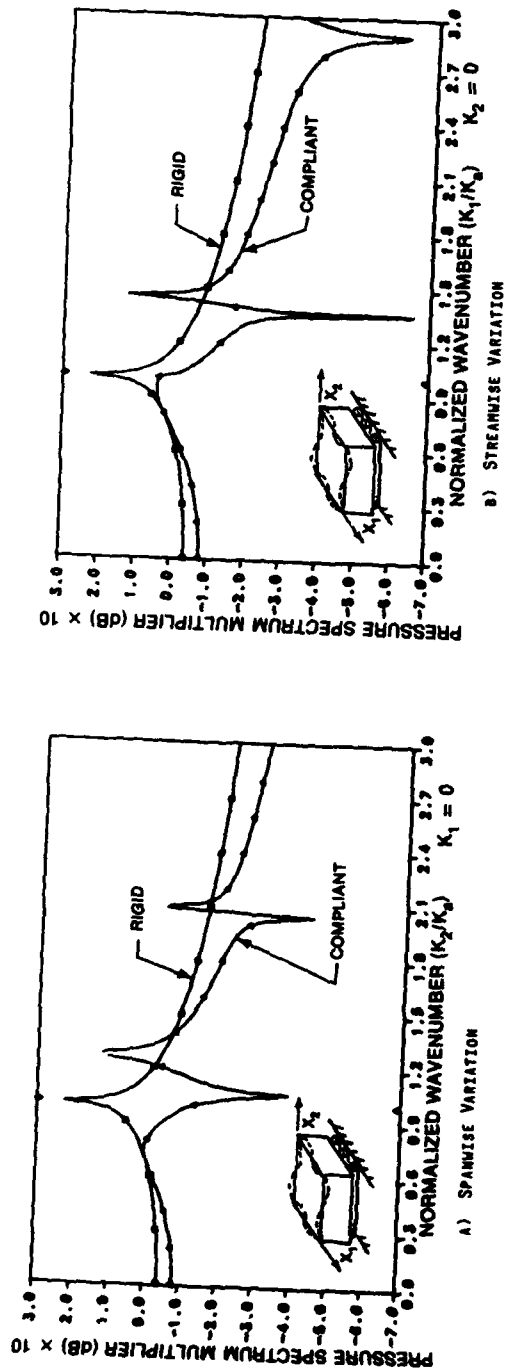
FIGURE 4. INFLUENCE OF DIRECTIONAL BOUNDARY CONDITIONS ON WALL
PRESSURE SPECTRUM MULTIPLIER, $20 \log_{10} (|K_m M_m|)$,
FOR BASE CASE LAYER WITH SLIP X_1 AND FIXED X_2, X_3
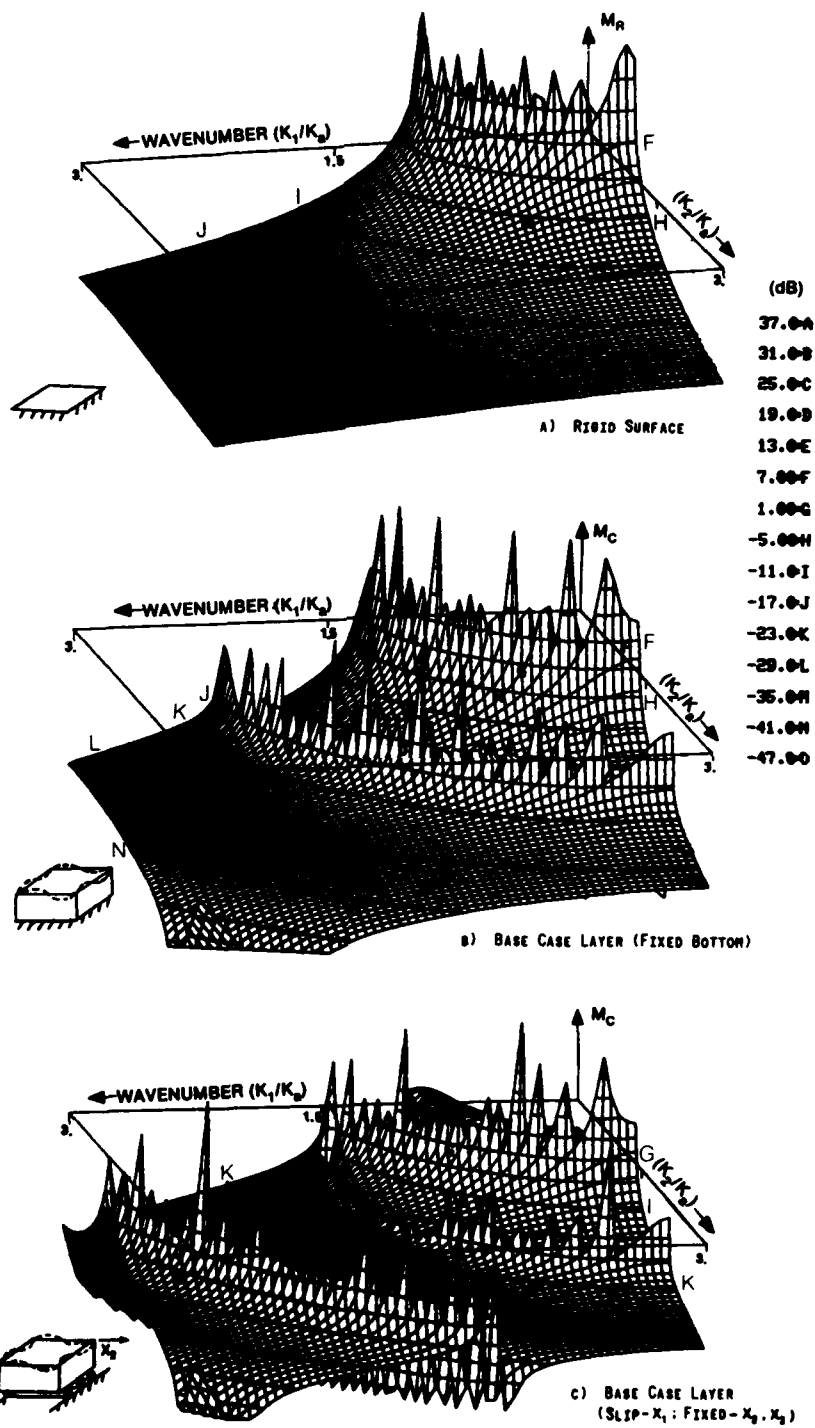BOUNDARY CONDITIONS AT $k_a = \pi/5$.

86

FIGURE 5. CARPET PLOT OF WALL PRESSURE SPECTRUM MULTIPLIER, $20 \log_{10}(|k_o M_c|)$, FOR BASE CASE LAYER AT $k_o = \omega/c$.

that the PATRAN plot routine used here, sampled the spectrum on a 61 x 61 rectangular (k_1, k_2) grid, consequently sharply peaked ridges appear to have a "bed-of-nails" appearance, whereas they actually have a smooth ridge appearance like the lip of a cup. In Figure 5c, the fade out of the shear spike ridge starting at $\bar{k}/k_a = (0.0, 2.1)$ is observed and it tends to smooth out at roughly $\bar{k}/k_a = (1.5, 1.5)$. For comparison purposes, the rigid wall spectrum is shown in Figure 5a.

Finally, it is noted that another singularity appears to arise in the neighborhood of $\bar{k}/k_a = (3.0, 3.0)$ in Figure 5c. It is speculated that this ridge is the result of some higher order singularities appearing in the impedance expression. The occurance of such high order singularities can be illustrated by examining the similar zero shear impedance layer governed by equation (13), where so long as γ_d is real, $\gamma_d D = \pi/2, 3\pi/2, 5\pi/2$, etc. would lead to other higher order singularities. The impedance singularities for the Figure 5c example are governed by the more complicated equation (A-12), where the zero of the denominator of equation (A-12) would be evaluted numerically, and the deformation mode of the surface would need to be examined in order to identify the physical nature of the singularity. This level of examination is beyond the intend of this demonstration problem and will not be pursued further here.

Influence of Directional Property Plate on Pressure Spectrum

In this example, the directional property of the impedance is introduced, by attaching a thin plate with directional material stress-strain properties to the bottom of the base case layer. This is the same as the case considered earlier in Figure 3d, except here, the stress-strain law moduli, E_{11}, E_{22}, E_{12}, G employed in equation (A-17) of the Appendix are not dictated by the isotropic conditions of equations (14), but rather these four quantities can all be set independently.

The motivation for selecting the constants is guided by the previous slipping boundary condition. Instead of totally releasing the x_1 direction surface traction (i.e., the slip condition, this effect is simulated by substantially reducing the streamwise direction in-plane modulus, E_{11}, while leaving the spanwise direction modulus equal to what it was for the isotropic case. This type of material behavior can be achieved through the use of fibrous materials imbedded in some sort of epoxy. For the case at hand, let the directional properties (superscripts o) be the following fractions of the previously used isotropic constants (superscripts i) in the example corresponding for Figure 3d:

$$E_{11}^o = E_{11}^i/10 = 12.0 \times 10^5 \; ; \qquad E_{22}^o = E_{22}^i = 12.0 \times 10^6$$

$$E_{12}^o = E_{12}^i/10 = 3.60 \times 10^5 \; ; \qquad G^o = G^i/4 = 1.05 \times 10^6$$

Upon using the above constants in conjunction with the layer-to-plate combined impedance relationship derived in the Appendix, the resulting pressure spectrum multipliers are shown in Figure 6a and 6b for the $\bar{k} = (k_1, 0)$ and $\bar{k} = (0,k_2)$ cuts respectively. Upon comparing Figures 6a and 3d, it is noted that the spanwise direction spectrum for the directional property plate is very similar to the homogeneous plate spectrum (noting that even though Figure 3d is plotted vs k_1, it is exactly the same as the spectrum plotted vs k_2). It is observed that, the corresponding Figure 6a plot in the streamwise direction is missing the shear spike, analogous to the slipping boundary case. Thus a traction release condition is simulated with soft moduli in the slip direction of interest.

The transition from the k_2 plane, containing the shear spike, into the k_1 plane can be better illustrated by comparing the Figure 7a carpet plot of

a) STREAMWISE VARIATION

$K_2 = 0$

NORMALIZED WAVENUMBER (K_1/K_o)

PRESSURE SPECTRUM MULTIPLIER (dB) × 10

COMPLIANT

RIGID

b) SPANWISE VARIATION

$K_1 = 0$

NORMALIZED WAVENUMBER (K_2/K_o)

PRESSURE SPECTRUM MULTIPLIER (dB) × 10

COMPLIANT

RIGID

c) DAMPING IN PLATE ONLY: $\eta_{p1} = \eta_{p2} = \eta_{p12} = .10$

$K_2 = 0$

NORMALIZED WAVENUMBER (K_1/K_o)

PRESSURE SPECTRUM MULTIPLIER (dB) × 10

DAMPING CUTOFF

RIGID

COMPLIANT DAMPED

COMPLIANT

d) DAMPING IN LAYER ONLY: $\eta_\ell = .05$, $\eta_s = .10$

$K_2 = 0$

NORMALIZED WAVENUMBER (K_1/K_o)

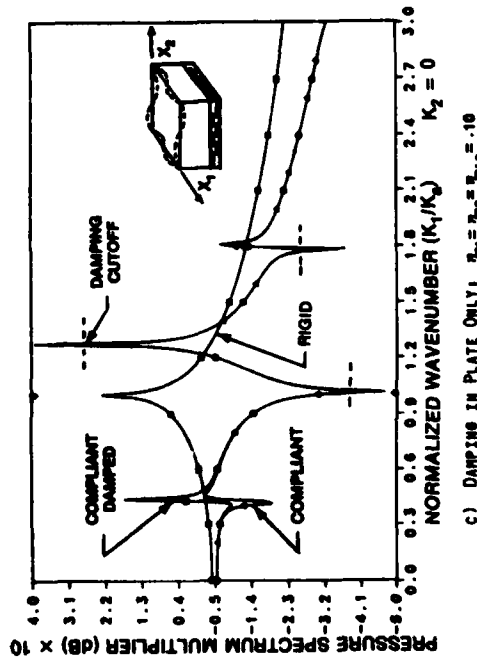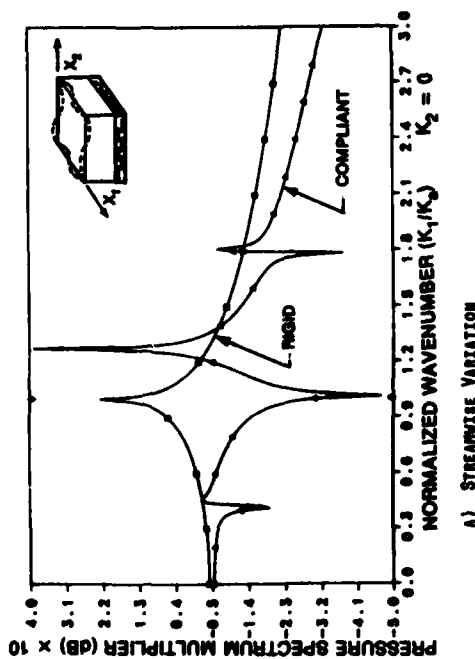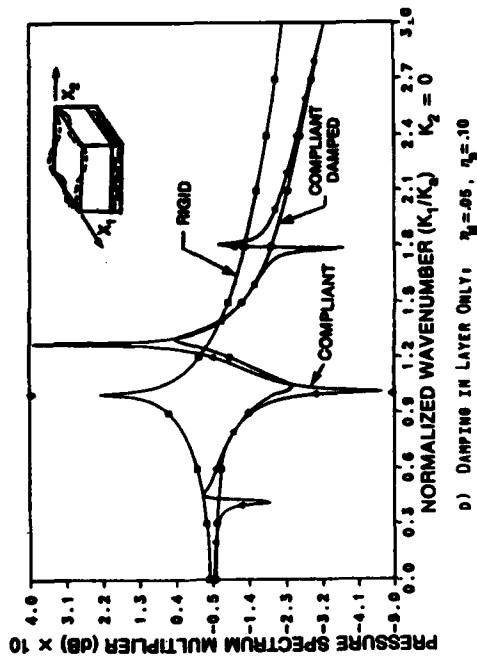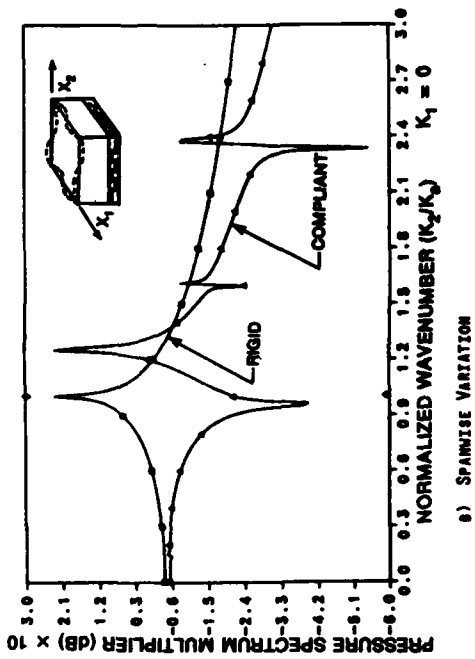PRESSURE SPECTRUM MULTIPLIER (dB) × 10

RIGID

COMPLIANT DAMPED

COMPLIANT

FIGURE 6. INFLUENCE OF ATTACHED DIRECTIONAL PROPERTY PLATE ON WALL PRESSURE SPECTRUM MULTIPLIER. 20 LOG10 (|$K_m M_m$|) AT $k_o = \pi/5$.

(dB)

37.0-A
31.0-B
25.0-C
19.0-D
13.0-E
7.00-F
1.00-G
-5.00-H
-11.0-I
-17.0-J
-23.0-K
-29.0-L
-35.0-M
-41.0-N
-47.00-O

A) ATTACHED ISOTROPIC PLATE

B) ATTACHED DIRECTIONAL MODULI PLATE:
$E_{11} = E_{22}/10$

C) ATTACHED DIRECTIONAL MODULI PLATE:
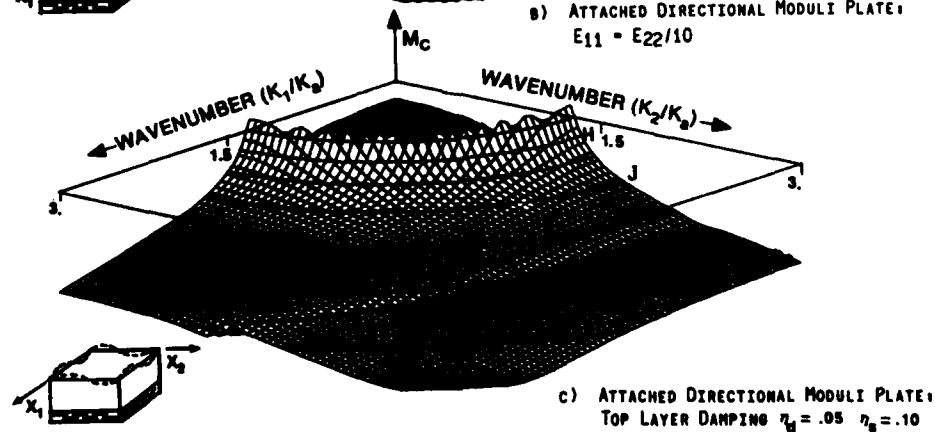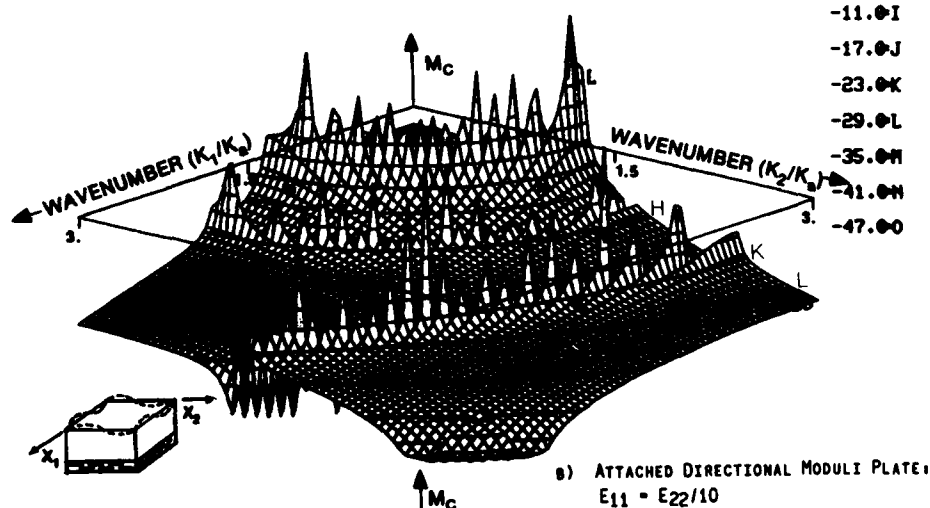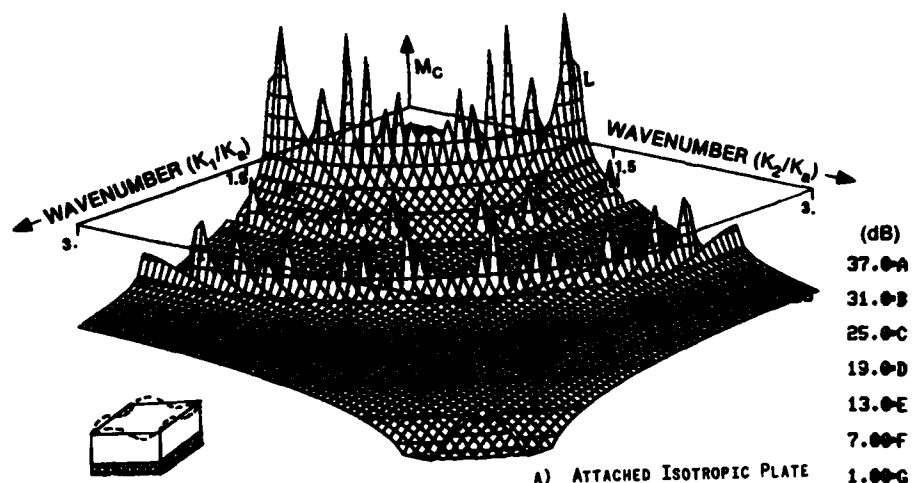TOP LAYER DAMPING $\eta_d = .05$ $\eta_s = .10$

FIGURE 7. CARPET PLOT OF WALL PRESSURE SPECTRUM MULTIPLIER, 20 $LOG_{10}(|k_a M_c|)$, FOR BASE CASE LAYER - DIRECTIONAL PROPERTY PLATE ATTACHMENT AT $k_a = \pi/5$.

the spectrum multiplier for the layer-homogeneous plate case (i.e., the carpet plot counterpart of Figure 3d) to the corresponding Figure 7b carpet plot for the layer-directional property plate case. In Figure 7a, the shear spike (third ridge of spikes from the origin) continues to travel from the M_c-k_2 plane to a corresponding position in the M_c-k_1 plane; however, in the Figure 7b plot, the shear spike starting in the M_c-k_2 plane, heads outward and away from intersecting with the k_1 axis over the range $0 \leq k_1/k_a \leq 3$.

The effect of plate damping is illustrated in Figure 6c by assigning the directional property plate damping parameters (defined in the Appendix) of $\eta_{p1} = \eta_{p2} = \eta_{p12} = 0.1$ while leaving the base case layer undamped. As shown, the damped and undamped spectrum multipliers are practically indistinguishable for $k_1/k_a > .6$ except for the rounded off spikes (the reduced peaks are indicated by the dashed lines). The damped plate evolves a new spike for $k_1/k_a < .6$ that is not present in the undamped case. The reason for this type of occurrence when damping is present was discussed earlier in the spectrum trends section. Next, the effect of layer damping is shown in Figure 6d by assigning the base case layer damping parameters of $\eta_d = .05$, $\eta_s = .10$ while leaving the plate undamped. In this case, the layer damping has a more dramatic effect on reducing the magnitude of the spectrum multiplier as compared to the plate damping case. The carpet plot counterpart of the Figure 6d layer damping case is shown in Figure 7c wherein the overall smoothing of spectrum multiplier is evident.

Finally, the influence of base case layer thickness and material variations on the undamped directional property plate-layer model spectrum just considered in Figures 6a and 6b is displayed in Figure 8. The spanwise and streamwise curves in Figure 8a and 8b repeat the Figure 6a, 6b case except the layer thickness D is halfed (i.e., 5 cm). For reference purposes, the results of the D and D/2 case are overlayed and as shown, the thinner layer appears to be a smoother curve with only one major spike over the wavenumber range considered. The Figure 8c example again is a repeat of the Figure 6a case for a directional property plate-layer surface except here, all other things held constant, the layer dilational wave speed is greater by a factor of 1.5, while the layer shear wave speed remains the same. For comparison purposes, both the original and new case are superimposed onto the same plot. The new 1.5 C_p case has removed the dilatational spike while leaving the shear layer peak and fluxure wave peak in about the same position as the previous C_p case.

CONCLUDING REMARKS

The study presented herein starts with an isotropic base case layer surface compliance and investigates the effect of various compliance alterations such as changes in boundary conditions, backing plate attachments, material properties, damping treatments and thickness. The appearance of spikes in the pressure spectrum multipliers is often dramatically altered by such variations. The results show that it is possible to shape the spectrum multiplier over some desired wavenumber-frequency domain by altering the boundary conditions and/or material properties.
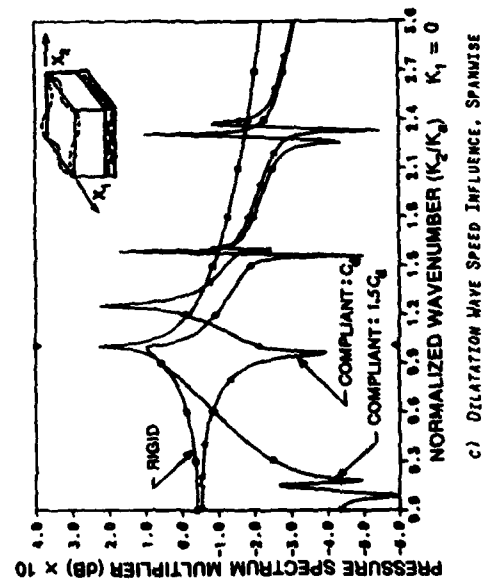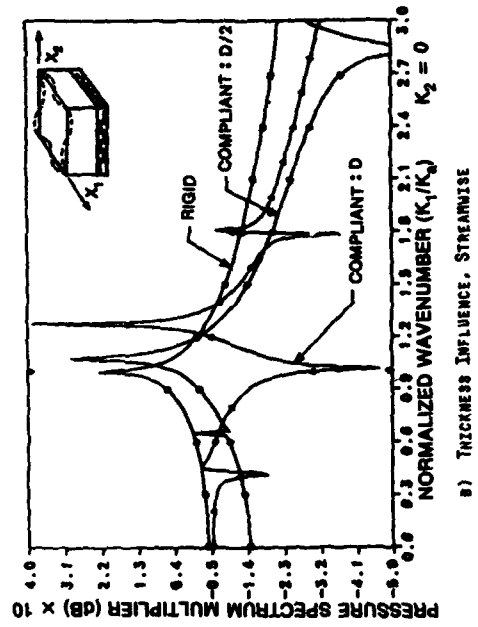
91

a) THICKNESS INFLUENCE, SPANWISE

b) THICKNESS INFLUENCE, STREAMWISE
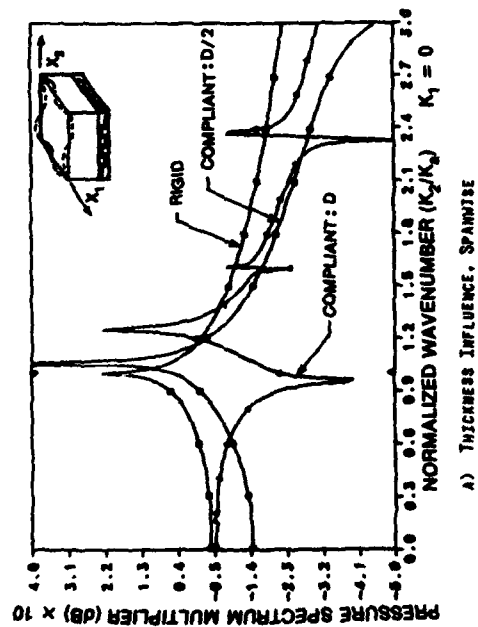
c) DILATATION WAVE SPEED INFLUENCE, SPANWISE

FIGURE 8. INFLUENCE OF THICKNESS AND MATERIAL VARIATION ON WALL PRESSURE SPECTRUM MULTIPLIER. $20 \log_{10}(|k_2M_1|)$ AT $k_2 = \pi/5$ FOR DIRECTIONAL PROPERTY PLATE ATTACHED TO BASE CASE LAYER.

92

APPENDIX

In this appendix, the development for obtaining the surface impedance for the general model shown in Fig. 1 is given. The procedure is broken up into two phases, where the first is for the isotropic layer with general non-symmetric boundary conditions and the second phase is concerned with attaching a plate with directional material properties.

Top Layer Impedance

The procedure is to load the surface of the solid, $x_3 = 0$, with a pressure distribution of the form

$$\sigma_{33}(x_1, x_2, 0, \omega') = -\Delta P_0 \, e^{i(k_1 x_1 + k_2 x_2 - \omega' t)} \tag{A-1}$$

where $-\omega' t$ is used rather than $+\omega t$ in order to be consistent with the referenced potential formulation (8) employed in this section. At the end of the derivation, the desired impedance can be obtained by replacing ω' with $-\omega$ to be consistent with the sign convention for ω used to derive the spectrum equation (1). Upon solving for the normal velocity, $u_3(x, y, 0, \omega')$, the velocity impedance is found from

$$Z(\omega') = -\sigma_{33}/\dot{u}_3 \tag{A-2}$$

Following the potential solution formulation (8) for linear elastic time dependent solutions, the equations of elasticity can be rewritten in terms of three uncoupled potential solutions, based on rewriting the displacement vector in the form

$$\bar{u} = \bar{L} + \bar{M} + \bar{N} \tag{A-3}$$

where for Cartesian Coordinates, L, M, N reduce to the simpler forms

$$\bar{L} = \bar{\nabla}\phi(x,t) \qquad \bar{M} = \bar{\nabla}\psi(x,t) \times \bar{j} \qquad \bar{N} = \bar{\nabla}\frac{\partial(\ell\chi)}{\partial x_2} - \bar{j}\,\nabla^2(\ell\chi) \tag{A-4}$$

The notation $\bar{i}$, $\bar{j}$, $\bar{k}$ refer to unit vectors along the corresponding x_1, x_2, x_3 coordinate directions. The arbitrary scale factor, ℓ, can be absorbed into a new potential, $\tilde{\chi} = \ell\chi$. The equations for determining $\phi, \psi, \tilde{\chi}$ are solutions to

$$c_d^2 \nabla^2\phi = \frac{\partial^2\phi}{\partial t^2} \qquad c_s^2 \nabla^2\psi = \frac{\partial^2\psi}{\partial t^2} \qquad c_s^2 \nabla^2\tilde{\chi} = \frac{\partial^2\tilde{\chi}}{\partial t^2} \tag{A-5}$$

The steady state solutions to these potential equations can be written as

$$\phi(\bar{x},t) = \left(\phi_0^I \exp[-i\gamma_d x_3] + \phi_0^R \exp[i\gamma_d x_3]\right)\exp[i(k_1 x_1 + k_2 x_2 - \omega' t)]$$

$$\psi(\bar{x},t) = \left(\psi_0^I \exp[-i\gamma_s x_3] + \psi_0^R \exp[i\gamma_s x_3]\right)\exp[i(k_1 x_1 + k_2 x_2 - \omega' t)] \tag{A-6}$$

$$\tilde{\chi}(\bar{x},t) = \left(\tilde{\chi}_0^I \exp[-i\gamma_s x_3] + \tilde{\chi}_0^R \exp[i\gamma_s x_3]\right)\exp[i(k_1 x_1 + k_2 x_2 - \omega' t)]$$

93

where $\gamma_d = \sqrt{k_d^2 - k^2}$, $\gamma_s = \sqrt{k_s^2 - k^2}$ and

$k_d = \omega/C_d$, $k_s = \omega/C_s$ and $k^2 = k_1^2 + k_2^2$ and C_d and C_s are the

dilatational and shear wave speeds in the solid layer. The root of γ_d, γ_s is selected as positive when ω' is plus and minus when ω' is negative. The solutions (A-6) will satisfy the field equations (A-5). The remaining step is to find the six amplitudes ϕ_0^I, etc. that satisfy the boundary conditions. Three types of boundary conditions will be used. A descriptive triplet of words will be used to describe the condition, where the first word refers to the x_1 direction condition, second word the x_2 direction and the third word the x_3 direction. In all cases the top boundary condition is the same, namely the normal stress in the negative of the surface pressure (i.e., enforcement of the condition described by equation (A-1))and that the low wavenumber in-plane surface shear stresses are negligible)

$$\sigma_{33}(x_1,x_2,0,\omega') = -\Delta P_o \exp^{(k_1 x_1 + k_2 x_2 - \omega' t)}$$

$$\sigma_{31}(x_1,x_2,0,\omega') = 0.0 \qquad \sigma_{32}(x_1,x_2,0,\omega') = 0.0 \qquad \text{(A-7)}$$

The enforcement of the boundary conditions require information about velocity and stress, so the following relations are needed to connect the potential solutions to the physical unknowns. These are obtained by substituting (A-6) in the stress strain law of linear elasticity, where λ, μ are the linear elastic Lame' constants.

$$\sigma_{33} = -\lambda k_d^2 \phi + 2\mu\left[\frac{\partial^2 \phi}{\partial x_3^2} + \frac{\partial^2 \psi}{\partial x_1 \partial x_3}\right] + 2\mu\left[\frac{\partial^3 \tilde{x}}{\partial x_3^2 \partial x_2}\right]$$

$$\sigma_{31} = \mu\left[2\frac{\partial^2 \phi}{\partial x_1 \partial x_3} + \frac{\partial^2 \psi}{\partial x_1^2} - \frac{\partial^2 \psi}{\partial x_3^2} + 2\frac{\partial^3 \tilde{x}}{\partial x_1 \partial x_2 \partial x_3}\right] \qquad \text{(A-8)}$$

$$\sigma_{32} = \mu\left[2\frac{\partial^2 \phi}{\partial x_2 \partial x_3} + \frac{\partial^2 \psi}{\partial x_1 \partial x_2} + 2\frac{\partial^3 \tilde{x}}{\partial x_3 \partial x_2^2} + k_s^2 \frac{\partial \tilde{x}}{\partial x_3}\right]$$

where equations (A-5) have been used to simplify equations (A-8). Substituting (A-4) into (A-3) and differentiating with respect to time gives the velocity components

$$\dot{u}_1 = -i\omega'\left[\frac{\partial \phi}{\partial x_1} - \frac{\partial \psi}{\partial x_3} + \frac{\partial^2 \tilde{x}}{\partial x_1 \partial x_2}\right]$$

$$\dot{u}_2 = -i\omega'\left[\frac{\partial \phi}{\partial x_2} - \frac{\partial^2 \tilde{x}}{\partial x_1^2} - \frac{\partial^2 \tilde{x}}{\partial x_3^2}\right] \qquad \dot{u}_3 = -i\omega'\left[\frac{\partial \phi}{\partial x_3} + \frac{\partial \psi}{\partial x_1} + \frac{\partial^2 \tilde{y}}{\partial x_3 \partial x_2}\right] \qquad \text{(A-9)}$$

in terms of $\phi, \psi, \tilde{x}$.

(i)   Fixed-Fixed-Fixed Boundary Condition

Upon substituting equations (A-8) into the fixed bottom boundary condition

$$u_1(x_1,x_2,-D,\omega') = 0 \quad u_2(x_1,x_2,-D,\omega') = 0 \quad u_3(x_1,x_2,-D,\omega') = 0 \quad \text{(A-10)}$$

and into top boundary conditions (A-7), and cancelling out $\exp[i(k_1 x_1 + k_2 x_2 - \omega't)]$, simultaneous complex algebraic equations of the form

$$\left[A(k_1,k_2,\omega') \right] \left\{ \begin{array}{c} \phi_o^I \\ \phi_o^R \\ \psi_o^I \\ \psi_o^R \\ \tilde{\chi}_o^I \\ \tilde{\chi}_o^R \end{array} \right\} = \left\{ \begin{array}{c} -\Delta P_o \\ 0 \\ 0 \\ 0 \\ 0 \\ 0 \end{array} \right\} \qquad \text{(A-11)}$$

arise and are solved employing the double precision IMSL package equation

solver on a VAX computer. Upon solving for $\{\phi_o^I, \ldots, \tilde{\chi}_o^R\}^T$, amplitudes for each

desired k_1, k_2, ω' set, the corresponding normal velocity, $\dot{u}_3$ is computed at the surface and substituted into equation (2a) to form the velocity surface impedance

$$Z(\omega') = \frac{\Delta P_o}{\omega'\left[\gamma_d(\phi_o^R - \phi_o^I) + k_1(\psi_o^I + \psi_o^R) - i\gamma_s k_2(\tilde{\chi}_o^I - \tilde{\chi}_o^R)\right]} \qquad \text{(A-12)}$$

The above is related to the X^* needed in the wall pressure spectrum formulas by $X^* = -i\omega Z\big|_{\omega'=-\omega}$.

(ii) Free-Fixed-Fixed Boundary Condition

In this case the bottom side of the layer is free to slide in the x_1 direction while remaining fixed in the vertical and x_2 direction. Upon substituting equations (A-8) into the conditions

$$\sigma_{31}(x_1,x_2,-D,\omega') = 0 \quad \dot{u}_2(x_1,x_2,-D,\omega') = 0 \quad \dot{u}_3(x_1,x_2,-D,\omega') = 0 \quad \text{(A-13)}$$

again lead to a set of equations of the form (A-11) except the $A(k_1,k_2,\omega')$ array is different because of the different boundary conditions. Upon solving the new system of equations, the impedance is again formed with equation (A-12).

(iii) Free-Free-Free Boundary Condition

Here the bottom surface is free of all surface tractions and consequently upon substituting equations (A-8) into the conditions

$$\sigma_{31}(x_1,x_2,-D,\omega') = 0 \quad \sigma_{32}(x_1,x_2,-D,\omega') = 0 \quad \sigma_{33}(x_1,x_2,-D,\omega') = 0 \quad \text{(A-14)}$$

again lead to equations analogous to (A-11) and finally to the impedance via equation (A-12).

COMBINED TOP LAYER-BOTTOM PLATE IMPEDANCE

The impedance relation for the combined isotropic layer-plate of Fig. 1 can be developed by first obtaining the impedance relationship between normal stress and normal velocity and also, the impedance relating surface shear and in-plane motion for a thin elastic plate. These normal and in-plane plate impedances are then used as boundary conditions which are applied to the bottom side of the isotropic layer.

(i)   Normal Motion Plate Impedance

The equations of motion for an orthotropic flat plate are given by (9) in the form

$$\hat{D}_1 \frac{\partial^4 w}{\partial x_1^4} + 2\hat{H} \frac{\partial^4 w}{\partial x_1^2 \partial x_2^2} + \hat{D}_2 \frac{\partial^4 w}{\partial x_2^4} + \rho_p T \frac{\partial^2 w}{\partial t^2} = +q(x_1, x_2, t) \tag{A-15}$$

where q, the normal distributed surface traction, is taken as positive upward (in the $-x_3$ direction); w is the normal displacement to the plate (taken as positive in the $+x_3$ direction), ρ_p is the plate mass density per unit volume, T is the plate thickness and $\hat{D}_1$, $\hat{D}_2$ and $\hat{H}$ are the orthotropic plate rigidities and are given by

$$\hat{D}_1 = \frac{T^3 D_{11}}{12} \qquad \hat{D}_2 = \frac{T^3 E_{22}}{12} \qquad \hat{H} = \frac{T^3 E_{12}}{12} + \frac{2T^3 G}{12} \tag{A-16}$$

where the E_{11}, E_{22}, E_{12}, G moduli are constants appearing in the stress strain law of the form

$$\sigma_{11} = E_{11}\,\epsilon_{11} + E_{12}\,\epsilon_{22} \qquad \sigma_{22} = E_{22}\,\epsilon_{22} + E_{12}\,\epsilon_{11} \qquad \sigma_{12} = G\,\gamma_{12} \tag{A-17}$$

where $\epsilon_{11}, \epsilon_{22}$, are the curvature strains corresponding to the transverse deformation w. The normal traction on the plate is expressed in the form $q = q_0 \exp[i(k_1 x_1 + k_2 x_2 - \omega' t)]$ and the response, w is in the form $w = w_0 \exp[i(k_1 x_1 + k_2 x_2 - \omega' t)]$. Upon substituting these two expressions into equation (A-15) and solving for w in terms of q, we obtain

$$Z_{33}(\omega') = \frac{q}{\dot{w}} = \frac{-i}{\omega} \left[\rho_p T \omega^2 - (\hat{D}_1 k_1^4 + 2\hat{H} k_1^2 k_2^2 + \hat{D}_2 k_2^4) \right] \tag{A-18}$$

(ii)   In-plane Motion Plate Impedance

The in-plane plate dynamic equilibrium equations (9) are given by

$$\frac{\partial N_{11}}{\partial x_1} + \frac{\partial N_{12}}{\partial x_2} + \Delta \tau_1 = \rho_p T \frac{\partial^2 u}{\partial t^2}$$

$$\frac{\partial N_{12}}{\partial x_1} + \frac{\partial N_{22}}{\partial x_2} + \Delta \tau_2 = \rho_p T \frac{\partial^2 v}{\partial t^2} \tag{A-19}$$

where N_{11}, N_{22}, N_{12} are the plate in-plane membrane faces and Δ_1, Δ_2 are the plate surface tractions. The in-plane strain displacement relations are given by

$$\epsilon_{11} = \frac{\partial u}{\partial x_1} \qquad \epsilon_{22} = \frac{\partial v}{\partial x_2} \qquad \gamma_{12} = \frac{\partial u}{\partial x_2} + \frac{\partial v}{\partial x_1} \qquad \text{(A-20)}$$

and the in-plane membrane forces are related to the in-plane stresses by the relations

$$N_{11} = T\sigma_{11} \qquad N_{22} = T\sigma_{22} \qquad N_{12} = T\sigma_{12} \qquad \text{(A-21)}$$

Substituting (A-21) and (A-20) into (A-17) expresses the membrane forces in terms of motion. Then substituting that result into (A-19) yields

$$K_1 \frac{\partial^2 u}{\partial x_1^2} + K_4 \frac{\partial^2 u}{\partial x_2^2} + K_5 \frac{\partial^2 v}{\partial x_1 \partial x_2} = -\Delta\tau_1 + \rho_p T \frac{\partial^2 u}{\partial t^2}$$

$$\text{(A-22)}$$

$$K_2 \frac{\partial^2 v}{\partial x_2^2} + K_4 \frac{\partial^2 v}{\partial x_1^2} + K_5 \frac{\partial^2 u}{\partial x_1 \partial x_2} = -\Delta\tau_2 + \rho_p T \frac{\partial^2 v}{\partial t^2}$$

where the coefficients are related to the orthotropic material constants by the relations

$$K_1 = TE_{11}, \qquad K_2 = TE_{22}, \qquad K_5 = T(E_{12} + G), \qquad K_4 = TG \qquad \text{(A-23)}$$

Next the tractions and motions are expressed in the form

$$\Delta\tau_1 = \Delta\tau_{01} \exp(i[k_1 x_1 + k_2 x_2 - \omega't]), \quad \Delta\tau_2 = \Delta\tau_{02} \exp(i[k_1 x_1 + k_2 x_2 - \omega't]),$$

$$u = u_0 \exp(i[k_1 x_1 + k_2 x_2 - \omega't]), \text{ and } v = v_0 \exp(i[k_1 x_1 + k_2 x_2 - \omega't])$$

and upon substitution into the equations of motion (A-22), the following impedance relations

$$\Delta\tau_1 = Z_{13}^u \, \dot{u} + Z_{13}^v \, \dot{v} \qquad \Delta\tau_2 = Z_{23}^v \, \dot{v} + Z_{23}^u \, \dot{u} \qquad \text{(A-24)}$$

where

$$Z_{13}^u = (K_1 k_1^2 + K_4 k_2^2 - \rho_p T\omega'^2) i/\omega' \qquad Z_{13}^v = (k_1 k_2 K_5) i/\omega'$$

$$Z_{23}^v = (K_2 k_2^2 + K_4 k_1^2 - \rho_p T\omega'^2) i/\omega' \qquad Z_{23}^u = (k_1 k_2 K_5) i/\omega'$$

(iii) Layer-To-Plate Interface Connection

The bottom side of the layer at $x_3 = -D$ is connected to the plate with the boundary conditions

$$\sigma_{31}(x_1, x_2, -D, \omega') = \Delta\tau_1 \qquad \sigma_{32}(x_1, x_2, -D, \omega') = \Delta\tau_2 \qquad \sigma_{33}(x_1, x_2, -D, \omega') = q$$

Employing the plate impedance conditions (A-18) and (A-24) and noting the surface motions of the layer are equal to the plate middle surface motions (i.e., $\dot{u} = \dot{u}_1(x_1, x_2, -D, \omega')$, $\dot{v} = \dot{u}_2(x_1, x_2, -D, \omega')$ and $\dot{w} = \dot{u}_3(x_1, x_2, -D, \omega')$) the interface boundary conditions to the layer can be written as

$$\sigma_{31}(x_1,x_2,-D,\omega') = Z_{13}^{u}\, \dot{u}_1(x_1,x_2,-D,\omega') + Z_{13}^{v}\, \dot{u}_2(x_1,x_2-D,\omega')$$

$$\sigma_{32}(x_1,x_2,-D,\omega') = Z_{23}^{v}\, \dot{u}_2(x_1,x_2,-D,\omega') + Z_{23}^{u}\, \dot{u}_1(x_1,x_2-D,\omega') \qquad (A\text{-}25)$$

$$\sigma_{33}(x_1,x_2,-D,\omega') = Z_{33}^{w}\, \dot{u}_3(x_1,x_2,-D,\omega')$$

At this point, the procedure is essentially the same as the earlier simple boundary condition cases, where the desired fluid-layer interface surface impedance is obtained by substituting equations (A-8) into (A-25) and producing again, a set of equations like (A-11). Solving (A-11) for $\{\phi_0^I, \ldots, \bar{X}_0^R\}^T$, the final desired velocity surface impedance is evaluated with (A-12).

Introduction of Structural Damping

A simple form of steady state harmonic damping can be introduced by simply replacing the real elastic constants in the layer and/or plate, with corresponding complex moduli . Defining η as the ratio of the imaginary to the real component of the appropriate elatic moduli (denoted by i, r superscript respectively). For the layer, we define

$$n_s = \mu^i/\mu^r \quad \text{and} \quad n_d = (\lambda^i + 2\mu^i)/(\lambda^r + 2\mu^r) \qquad (A\text{-}26)$$

and for the plate

$$n_{p1} = E_{11}^i/E_{11}^r \quad n_{P2} = E_{22}^i/E_{22}^r \quad n_{p12} = E_{12}^i/E_{12}^r = G^i/G^r \qquad (A\text{-}27)$$

Surface Impedance Verification

The computer program which generates the compliant surface spectrum is straightforward, but rather lengthy, consequently some check cases are used to verify the accuracy of the calculations.

(i) Plate Theory Comparison

In this case, the upper isotropic layer impedance formulation is checked out against the corresponding thin plate velocity impedance (6) given by the simple expression

$$Z = -i(\rho_p T\omega^2 - D_p k^2)/\omega = -iX/\omega \qquad (A\text{-}28)$$

where the plate modulus is defined in $D_p = ET^3/[12(1 - \nu^2)]$.

A secondary by-product of this checkout is additional information regarding the adequacy of simple plate theory (i.e., without shear and rotary inertia correction effects) while using the dimension and material constants employed in the lower plate attachment model considered in the earlier Figure 3d. Consequently, the dimension and material of the check calculation are exactly the same as the plate model from Figure 3d. The impedance is computed with both the elastic solution discussed in section (iii) of this appendix, and with the simple plate impedance, equation A-28. The comparative impedance results (normalized by the $\rho_0 C_a$ of the fluid) results are plotted in Figure 1-A, and as osbserved, the agreement is very good over the range of interest $0 \le k_1/k_a \le 3.0$ herein. For larger values of k_1/k_a, the rotary inertia and shear correction terms are needed in order to continue to employ plate theory. The breakdown of the simple theory occurs roughly when the freely propagating flexure wavelength is about 1/5 or greater than the plate thickness (10).
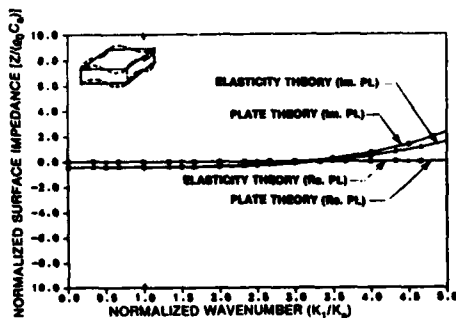
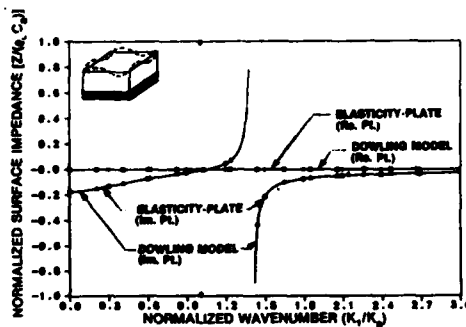FIGURE 1-A. COMPARISON OF ELASTICITY IMPEDANCE TO PLATE THEORY IMPEDANCE

FIGURE 2-A. COMPARISON OF COMBINED ELASTICITY-PLATE IMPEDANCE TO DOWLING NO SHEAR SOLID-PLATE IMPEDANCE

(ii) Isotropic Layer (zero shear) - Isotropic Plate Check

Here, the impedance of the reference (6) surface model consisting of a layer of material (with zero shear modulus) attached to an isotropic plate is used as a check case. The material properties and dimensions of the layer and plate correspond to the ones used in Figure 3d sample problem, with the exception that the base case layer Lame' elastic constants were assigned so the shear modulus was extremely small (i.e., μ = 10.0 psi) and the dilatational wave speed of the layer remains the same as the base case layer dilatational wave speed. The shear modulus is not set exactly zero, to avoid numerous indeterminant forms that would appear in the equation (A-12) impedance formula. The real and imaginary parts of the normalized velocity impedance are shown in Figure 2-A and as shown, the two results overlay each other over the whole domain of interest.

(iii) Omnidirectional Impedance Check

The impedance used to generate the Figure 4d curves employs all three of the potentials used in equation (A-12), consequently the fact that the results are the same for any $k_1^2 + k_2^2 = k^2$ = constant combination of k_1, k_2 is an additional check on the expected omnidirectional impedance relationship.

Acknowledgements

REFERENCES

1. Ffowcs-Williams, J. E., "Sound Radiation from Turbulent Boundary Layers Formed on Compliant Surfaces," Journal of Fluid Mechanics, Vol 22, 1965.

2. Strawderman, W. A., and Brand, R. S., "Turbulent-Flow Excited Vibration of A Simply Supported, Rectangular Flat Plate," Journal of the Acoustical Society of America, Vol 45, 1969.

3. Ffowcs-Williams, J. E., "Surface-Pressure Fluctuations Induced by Boundary-Layer Flow at Finite Mach Number," Vol 22, 1965.

4. Dowling, A. P., "Flow-Acoustic Interaction Near a Flexible Wall," Journal of Fluid Mechanics, Vol 128, 1983.

5. Lighthill, M. J., "On Sound Generated Aerodynamically," I. General theory, Proceedings of the Royal Society, London, Vol A211, 1952.

6. Dowling, A. P., "The Low Wavenumber Wall Pressure Spectrum on a Flexible Surface," Journal of Sound and Vibration, Vol 66, 1983.

7. Rogallo, R. S. and Moin, P., "Numerical Simulation of Turbulent Flows," Ann. Rev. Fluid Mech., Vol 16, 1984.

8. Pao, Y. H. and Mow C. C., Diffraction of Elastic Waves and Dynamic Stress Concentrations, Crane Russak, New York, 1971.

9. Ugural, A.C., Stresses in Plates and Shells, McGraw Hill, New York, 1981.

10. Midlin, R.D., "Influence of Rotary Inertia and Shear on Flexural Motions of Isotropic, Elastic Plates," Journal of Applied Mechanics, March 1951.